박 사 학 위 논 문

Ph.D. Dissertation

탄성 부유체의 정적/동적 통합해석 기법 및 응력 전달함수의 직접계산 방법

Integrated hydro -static and -dynamic analysis and direct calculation of stress RAO for elastic floating structures

2023

박 문 수 (朴 文 秀 Park, Moonsu)

한 국 과 학 기 술 원

Korea Advanced Institute of Science and Technology

박 사 학 위 논 문

탄성 부유체의 정적/동적 통합해석 기법 및 응력 전달함수의 직접계산 방법

2023

박 문 수

한 국 과 학 기 술 원

기계항공공학부/기계공학과

탄성 부유체의 정적/동적 통합해석 기법 및 응력 전달함수의 직접계산 방법

박 문 수

위 논문은 한국과학기술원 박사학위논문으로
학위논문 심사위원회의 심사를 통과하였음

2023년 6월 14일

심사위원장 이 필 승 (인)

심 사 위 원 김 진 환 (인)

심 사 위 원 김 대 겸 (인)

심 사 위 원 김 병 완 (인)

심 사 위 원 김 태 영 (인)

Integrated hydro -static and -dynamic analysis and direct calculation of stress RAO for elastic floating structures

Moonsu Park

Advisor: Phill-Seung Lee

A dissertation submitted to the faculty of
Korea Advanced Institute of Science and Technology in
partial fulfillment of the requirements for the degree of
Doctor of Philosophy in Mechanical Engineering

Daejeon, Korea
June 14, 2023

Approved by

Phill-Seung Lee
Professor of Mechanical Engineering

The study was conducted in accordance with Code of Research Ethics[1].

1) Declaration of Ethical Conduct in Research: I, as a graduate student of Korea Advanced Institute of Science and Technology, hereby declare that I have not committed any act that may damage the credibility of my research. This includes, but is not limited to, falsification, thesis written by someone else, distortion of research findings, and plagiarism. I confirm that my dissertation contains honest conclusions based on my own careful research under the guidance of my advisor.

DME 박문수. 탄성 부유체의 정적/동적 통합해석 기법 및 응력 전달함수의 직접계산 방법. 기계공학과. 2023년. 82+iii 쪽. 지도교수: 이필승. (영문 논문)

Park, Moonsu. Integrated hydro -static and -dynamic analysis and direct calculation of stress RAO for elastic floating structures. 2023. 82+iii pages. Advisor: Lee, Phill-Seung. (Text in English)

<u>초 록</u>

본 학위연구에서는 부유식 구조물의 정적 및 동적해석을 통합하기 위한 효과적인 수치해석 방법을 제안한다. 일반적으로 부유식 구조물의 흘수선은 정적해석을 통해 계산되며 부유식 구조물의 동적 해석을 위한 접수면의 메쉬 모델을 구성하는데 사용된다. 다양한 하중 조건을 경험하는 부유식 구조물의 경우 하중 조건의 개수만큼 메쉬모델을 작성해야 하므로 많은 어려움이 있다. 이 연구는 단월 메쉬모델을 이용하여 다양한 하중조건을 가진 부유식 구조물의 동적해석을 수행하고자 한다. 구조물은 유한요소법을 사용하여 모델링하고 외부유체는 경계요소법을 사용하여 모델링하며, 단일 메쉬는 정수 및 동적 해석 모두에 사용됩니다. 일치하지 않는 메쉬 처리 기술을 채택하여 부유 구조의 젖은 표면 메쉬가 자유 표면과 일치할 필요가 없으며 이에 따라 다양한 하중 조건에서 re-meshing 없이 강체 및 탄성 부유식 구조물에 대한 해석이 가능하다.

또한 주파수 도메인에서 수행되는 유탄성 해석에서 응력의 전달함수를 효율적으로 계산하는 방법에 대하여 소개하고자 한다. 주파수 도메인에서 유탄성 해석을 수행하면 실수부와 허수부로 구성된 조화응답 형태의 성분별 응력값이 도출된다. 구조물의 강도를 평가하기 위하여 응력 성분값을 조합하여 사용한다. 대표적인 응력이 von-Mises 응력과 주응력이다. 이들 응력은 비조화응답이므로 한주기 동안 최대값을 찾기 위해서는 시간의 변화에 대한 값들을 직접 계산하여 구하여야 한다. 본 연구에서는 이러한 어려움을 해결하기 위해, 주파수 도메인에서 강도평가를 위한 응력의 전달함수를 효율적으로 구할 수 있는 방법을 제안한다. 이 방법은 구조물의 최종강도 및 피로강도 등 건전성 분석 및 실시간 모니터링 시스템 등을 구현하기 위한 중요한 도구로 활용될 수 있을 것으로 기대된다.

<u>핵심낱말</u> 유한요소법, 경계요소법, 유탄성, 유체-구조 상호작용, 응력전달함수, 비조화함수

Abstract

This dissertation proposes an effective numerical method to integrate hydro-static and dynamic analysis of floating structures. In general, the waterline of floating structures is calculated through hydrostatic analysis and is used to construct wet-surface meshes for hydrodynamic analysis of floating structures. Those are time consuming and complicated tasks, in particular, when various loading conditions are considered. This study focuses on resolving the difficulties. A floating structure is modeled using the finite element method and the external fluid is modeled using the boundary element method. A single mesh is used for both hydro-static and dynamic analyses. Adopting a non-matching mesh treatment technique, the wet surface mesh of the floating structure does not need to match with free surface. Hydrodynamic analysis considering both rigid and flexible floating structures is possible without remeshing in various loading conditions. The effectiveness of the proposed method is demonstrated through several numerical examples.

In addition, we propose an efficient method for calculating the transfer function of stress in the frequency domain for hydroelastic analysis. After performing hydroelastic analysis in the frequency domain, stress values in the form of harmonic response with real and imaginary components are obtained. These stress values need to be combined to calculate representative stresses such as von-Mises stress and principal stress, which are non-harmonic responses, and require direct calculation of values over time to find the maximum value during one period. To overcome this challenge, this study proposes a method to efficiently obtain the transfer function of stress in the frequency domain for evaluating the strength of structures. This method is expected to be a valuable tool for implementing integrity analysis and real-time monitoring systems for structures, as well as evaluating the ultimate strength and fatigue strength of structures in reliability analysis.

Keywords Structural analysis, Finite element method, Fluid structure interaction, Hydroelasticity, Hydrodynamic Hydrostatic

Contents

List of Tables

List of Figures

Chapter 1. Introduction

Analyzing the motion of ships and offshore structures due to various external loads is a very important task not only in the design stage but also in the operation process. Numerous related studies have been conducted focusing on complex interactions between floating structures and external flow through experimental, analytical, and numerical approaches [2-7]. For a long time, hydrodynamic analysis has been performed under the assumption that the structure is a rigid body [4, 5]. Over the past decade, the enlargement of ships and offshore structures has triggered the development of hydroelastic analysis techniques, and related research is progressing quite successfully [8-18].

In general, the hydrodynamic response is calculated using the hydrostatic equilibrium state as a reference configuration. Therefore, in order to perform hydrodynamic analysis, hydrostatic analysis must be performed in advance [12,16,34-36]. In other words, the waterline of a floating structure is calculated through hydrostatic analysis, a wet-surface mesh matching with the waterline is created, and hydrodynamic analysis is performed. In the design of ships and offshore structures, many loading conditions are considered. Performing hydrostatic analysis and creating a wet-surface mesh corresponding to each loading condition is a very complicated and time-consuming task.

In order to overcome the aforementioned difficulties, it is necessary to integrate hydrostatic analysis and hydrodynamic analysis and use a single mesh model. To do so, we should resolve a problem of non-matching between the waterline and the wet-surface mesh that inevitably occurs. There have been several attempts to deal with such non-matching mesh problems in fluid-structure interaction analysis [16, 31-33].

In the frequency domain, the stress of a structure is calculated using the displacement, velocity, acceleration, and other parameters obtained through hydroelastic analysis. The stress components of a structure are harmonic functions. To evaluate the strength of a structure, the stress components are combined and evaluated[41-50], with representative examples being von-Mises stress and principal stress. These stresses are no longer harmonic functions. In the conventional method, the one period is divided into equal time intervals, and the maximum value obtained through individual calculations is used in the design[42].

The goal of this dissertation is to present novel methods that overcome the drawbacks mentioned above. We propose a method for Integrated hydro-static and dynamic analysis of floating structures through non-matching mesh treatment. Also, we intend to propose an effective method for obtaining the stress transfer function for evaluating the strength of a structure obtained through frequency domain elastic analysis.

In Chapter 2, we propose an effective method for hydrodynamic analysis of floating structures with various load conditions using a single mesh model. To deal with the non-matching mesh problem, we adopt a special numerical integration method, in which remeshing is not necessarily [16]. Through this, hydrostatic analysis and hydrodynamic analysis were completely integrated. We demonstrate the numerical scheme based on the direct coupling method for 3D hydorelastic analysis, where the structure is model using the finite element method, the external fluid is modeled using the boundary element method. The direct coupling method can also be used for hydrodynamic analysis of rigid body motion. Since hydro-static and -dynamic analyses conducted separately in engineering practice are integrated, the time and effort required for hydrodynamic analysis can be significantly reduced, especially when various loading conditions are considered.

In Chapter 3, Direct calculation of stress RAOs in hydroelastic analysis is presented. The response of a ship or floating structure to unit waves is referred to as the Response Amplitude Operator (RAO), and the responses are statistically combined to calculate the structural response in real sea states, which are irregular waves[44,51,52]. While the stress components for regular waves are in harmonic function form, we propose a method for finding the maximum value of combined stress, which is in non-harmonic function form, for evaluating the strength of the structure. Through this approach, we aim to improve computational speed compared to conventional methods.

In Chapter 4, conclusions and future works are provided.

Chapter 2. Integrated hydrostatic and hydrodynamic analysis of flexible floating structures

We present the Integrated hydrostatic and hydrodynamic analysis of flexible floating structures in this chapter. The mathematical formulation in Section 2.1 and the numerical procedure in Section 2.2 are presented. In Section 2.3, the effective numerical integration methods are introduced. In Section 2.4, the feasibility of the proposed numerical procedure is demonstrated through various problems corresponding to rigid and elastic body cases. Finally, the concluding remarks are given.

2.1. Integrated hydrostatic and hydrodynamic formulation

This section provides the integrated hydrostatic and hydrodynamic formulation based on the hydrostatic formulation in Ref. [15] and hydrodynamic formulation in Refs. [11,13,18]. All possible external forces that floating structures may be subjected to are taken into account. We adopt mathematical notations in Ref. [26]

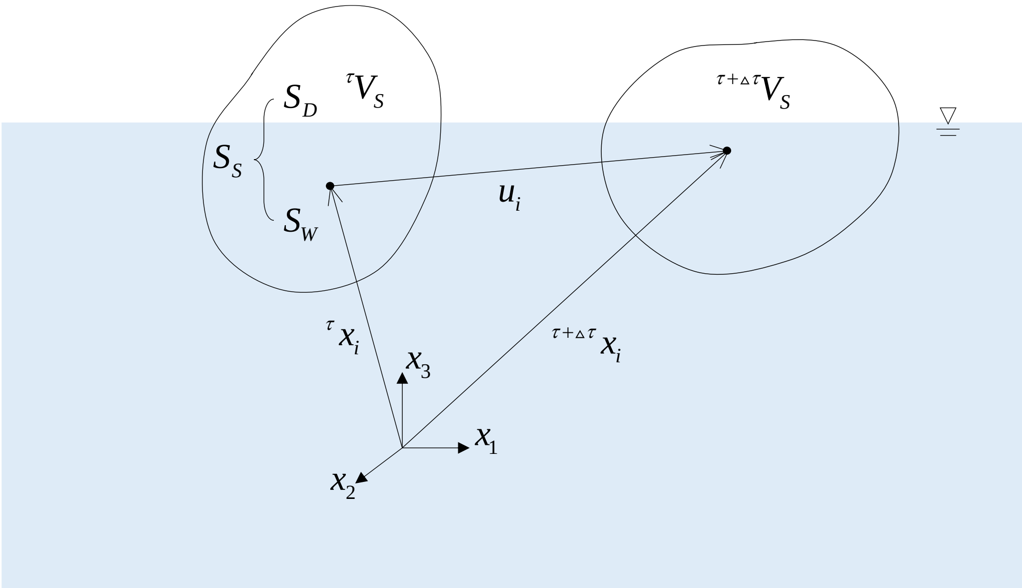

Fig. 2-1. Floating body at times τ and $\tau+\Delta\tau$

2.1.1. Incremental equilibrium equation

As shown in Fig. 2-1, a structure floating in the water is positioned in a fixed Cartesian coordinate system with coordinates x_i, the origin of which is located on the water plane. The volume of the structure is denoted as V_S and its surface is represented by $S_S = S_D \cup S_W$, where S_D and S_W denote dry and wet surfaces, respectively. The material for the floating structure is assumed to be homogeneous, isotropic, and linear elastic.

The Lagrangian description is employed to obtain the integrated hydrostatic and hydrodynamic formulation [26]. Two different configurations at times τ and $\tau + \Delta\tau$ are considered as a known (reference) and unknown configurations, respectively.

The structure is subjected to a water pressure field at time $\tau + \Delta\tau$

$$ {}^{\tau+\Delta\tau}P = -\rho_W g \, {}^{\tau+\Delta\tau}x_3 + {}^{\tau+\Delta\tau}P_D \tag{2-1} $$

where $-\rho_W g \, {}^{\tau+\Delta\tau}x_3$ and ${}^{\tau+\Delta\tau}P_D$ denote the hydrostatic and hydrodynamic pressures, respectively, ρ_W is the fluid density, and g is the gravitational acceleration.

The equilibrium equations of the floating structure at time $\tau + \Delta\tau$ are given by

$$ \frac{\partial \, {}^{\tau+\Delta\tau}\sigma_{ij}}{\partial \, {}^{\tau+\Delta\tau}x_j} - \rho_S \, {}^{\tau+\Delta\tau}\ddot{x}_i - \rho_S g \delta_{i3} + {}^{\tau+\Delta\tau}f_i^B = 0 \quad \text{in} \quad {}^{\tau+\Delta\tau}V_S , $$

$$ {}^{\tau+\Delta\tau}\sigma_{ij} \, {}^{\tau+\Delta\tau}n_j = {}^{\tau+\Delta\tau}f_i^S \quad \text{on} \quad {}^{\tau+\Delta\tau}S_S , $$

$$ {}^{\tau+\Delta\tau}\sigma_{ij} \, {}^{\tau+\Delta\tau}n_j = -{}^{\tau+\Delta\tau}P \, {}^{\tau+\Delta\tau}n_i \quad \text{on} \quad {}^{\tau+\Delta\tau}S_W , \tag{2-2} $$

where ${}^{\tau+\Delta\tau}\sigma_{ij}$ is the Cauchy stress tensor at time $\tau + \Delta\tau$, ρ_S is the density of the floating structure, δ_{ij} is the Kronecker delta ($\delta_{ij} = 1$ if $i = j$ and $\delta_{ij} = 0$ otherwise), $\ddot{(\;)} = d^2(\;)/dt^2$ with time variable t, ${}^{\tau+\Delta\tau}n_i$ is the unit normal vector outward from the structure to the fluid at time $\tau + \Delta\tau$, ${}^{\tau+\Delta\tau}f_i^B$ denotes the body force at time $\tau + \Delta\tau$ except for inertia and gravity forces and, and ${}^{\tau+\Delta\tau}f_i^S$ denotes the surface force at time $\tau + \Delta\tau$ except for the water pressure.

The principle of virtual work at time $\tau + \Delta\tau$ can be stated as

$$ \int_{{}^{\tau+\Delta\tau}V_S} {}^{\tau+\Delta\tau}\sigma_{ij} \delta \, {}_{\tau+\Delta\tau}e_{ij} \, d \, {}^{\tau+\Delta\tau}V_S = \tag{2-3a} $$

$$ -\int_{{}^{\tau+\Delta\tau}V_S} \rho_S \, {}^{\tau+\Delta\tau}\ddot{x}_i \delta u_i \, d \, {}^{\tau+\Delta\tau}V_S - \int_{{}^{\tau+\Delta\tau}V_S} \rho_S g \delta u_3 \, d \, {}^{\tau+\Delta\tau}V_S \tag{2-3b} $$

$$+\int_{^{\tau+\Delta\tau}S_W} \rho_W g\, {}^{\tau+\Delta\tau}x_3\, {}^{\tau+\Delta\tau}n_i \delta u_i d\, {}^{\tau+\Delta\tau}S_W - \int_{^{\tau+\Delta\tau}S_W} {}^{\tau+\Delta\tau}P_D\, {}^{\tau+\Delta\tau}n_i \delta u_i d\, {}^{\tau+\Delta\tau}S_W \tag{2-3c}$$

$$+\int_{^{\tau+\Delta\tau}V_S} {}^{\tau+\Delta\tau}f_i^B \delta u_i d\, {}^{\tau+\Delta\tau}V_S + \int_{^{\tau+\Delta\tau}S_S} {}^{\tau+\Delta\tau}f_i^S \delta u_i d\, {}^{\tau+\Delta\tau}S_S \, , \tag{2-3d}$$

where δu_i denotes the virtual displacement vector, and $\delta\, {}_{\tau+\Delta\tau}e_{ij}$ is the corresponding virtual strain tensor

$$\delta\, {}_{\tau+\Delta\tau}e_{ij} = \frac{1}{2}\left(\frac{\partial \delta u_i}{\partial\, {}^{\tau+\Delta\tau}x_j} + \frac{\partial \delta u_j}{\partial\, {}^{\tau+\Delta\tau}x_i}\right). \tag{2-4}$$

Eq. (2-3a) denotes the internal virtual work and Eqs. (2-3b)-(2-3d) denote the external virtual works corresponding to inertia, gravity, water pressure and other external body and surface forces. Note that the variational operator δ denotes virtual variables.

The internal virtual work in Eq. (2-3a) can be rewritten for the reference configuration at time τ

$$\int_{^{\tau+\Delta\tau}V_S} {}^{\tau+\Delta\tau}\sigma_{ij} \delta\, {}_{\tau+\Delta\tau}e_{ij} d\, {}^{\tau+\Delta\tau}V_S = \int_{^{\tau}V_S} {}^{\tau+\Delta\tau}_{\tau}S_{ij} \delta\, {}^{\tau+\Delta\tau}_{\tau}\varepsilon_{ij} d\, {}^{\tau}V_S \tag{2-5}$$

with

$${}^{\tau+\Delta\tau}_{\tau}S_{ij} = \det({}^{\tau+\Delta\tau}_{\tau}x_{ij})\, {}^{\tau}_{\tau+\Delta\tau}x_{im}\, {}^{\tau}_{\tau+\Delta\tau}x_{jn}\, {}^{\tau+\Delta\tau}\sigma_{mn} \, ,$$

$${}^{\tau+\Delta\tau}_{\tau}\varepsilon_{ij} = \frac{1}{2}\left(\frac{\partial u_i}{\partial\, {}^{\tau}x_j} + \frac{\partial u_j}{\partial\, {}^{\tau}x_i} + \frac{\partial u_k}{\partial\, {}^{\tau}x_i}\frac{\partial u_k}{\partial\, {}^{\tau}x_j}\right),$$

in which ${}^{\tau+\Delta\tau}_{\tau}S_{ij}$ and ${}^{\tau+\Delta\tau}_{\tau}\varepsilon_{ij}$ denote the second Piola-Kirchhoff stress tensor and the Green-Lagrange strain tensor, respectively, at time $\tau+\Delta\tau$ with respect to the reference configuration at time τ, ${}^{\tau+\Delta\tau}_{\tau}x_{ij} = \dfrac{\partial\, {}^{\tau+\Delta\tau}x_i}{\partial\, {}^{\tau}x_j}$ is the deformation tensor, and u_i denotes the displacement at time $\tau+\Delta\tau$ measured from the reference configuration at time τ. That is, $u_i = {}^{\tau+\Delta\tau}x_i - {}^{\tau}x_i$.

The second Piola-Kirchhoff stress tensor is decomposed as

$${}^{\tau+\Delta\tau}_{\tau}S_{ij} = {}^{\tau}_{\tau}S_{ij} + {}_{\tau}S_{ij} = {}^{\tau}\sigma_{ij} + {}_{\tau}S_{ij} \, , \tag{2-6}$$

in which ${}^{\tau}_{\tau}S_{ij} = {}^{\tau}\sigma_{ij}$ and ${}_{\tau}S_{ij}$ is the incremental second Piola-Kirchhoff stress tensor.

The Green-Lagrange strain tensor is also decomposed as

$${}^{\tau+\Delta\tau}_{\tau}\varepsilon_{ij} = {}^{\tau}_{\tau}\varepsilon_{ij} + {}_{\tau}\varepsilon_{ij} = {}_{\tau}\varepsilon_{ij} \, , \tag{2-7}$$

where ${}^{\tau}_{\tau}\varepsilon_{ij} = 0$ and ${}_{\tau}\varepsilon_{ij}$ is the incremental Green-Lagrange strain tensor.

The incremental Green-Lagrange strain tensor consists of the linear (${}_{\tau}e_{ij}$) and nonlinear (${}_{\tau}\eta_{ij}$) parts

$$ {}_{\tau}\varepsilon_{ij} = {}_{\tau}e_{ij} + {}_{\tau}\eta_{ij} \tag{2-8} $$

with ${}_{\tau}e_{ij} = \frac{1}{2}(\frac{\partial u_i}{\partial {}^{\tau}x_j} + \frac{\partial u_j}{\partial {}^{\tau}x_i})$, ${}_{\tau}\eta_{ij} = \frac{1}{2}\frac{\partial u_k}{\partial {}^{\tau}x_i}\frac{\partial u_k}{\partial {}^{\tau}x_j}$.

Substituting Eqs. (2-6)-(2-8) into Eq. (2-5) and assuming ${}_{\tau}S_{ij} \approx C_{ijrs}\,{}_{\tau}e_{rs}$, the resulting equation is linearized with respect to u_i . The linearized internal virtual work is obtained as

$$ \int_{{}^{\tau}V_S} {}^{\tau+\Delta\tau}_{\tau}S_{ij}\delta\,{}^{\tau+\Delta\tau}_{\tau}\varepsilon_{ij}d\,{}^{\tau}V_S \approx \int_{{}^{\tau}V_S} C_{ijkl}\,{}_{\tau}e_{kl}\delta\,{}_{\tau}e_{ij}d\,{}^{\tau}V_S + \int_{{}^{\tau}V_S} {}^{\tau}\sigma_{ij}\delta\,{}_{\tau}\eta_{ij}d\,{}^{\tau}V_S + \int_{{}^{\tau}V_S} {}^{\tau}\sigma_{ij}\delta\,{}_{\tau}e_{ij}d\,{}^{\tau}V_S\ . \tag{2-9} $$

It is important to carefully linearize the first term in Eq. (2-3c). Substituting the following relations into Eq. (2-3c)

$$ {}^{\tau+\Delta\tau}x_3 = {}^{\tau}x_3 + u_3\,, \tag{2-10} $$

$$ {}^{\tau+\Delta\tau}n_i d\,{}^{\tau+\Delta\tau}S_W = \det({}^{\tau+\Delta\tau}_{\tau}x_{ij})\,{}^{\tau}_{\tau+\Delta\tau}x_{ji}\,{}^{\tau}n_j d\,{}^{\tau}S_W\,, \tag{2-11} $$

the first term in Eq. (2-3c) becomes

$$ \int_{{}^{\tau+\Delta\tau}S_W} \rho_W g\,{}^{\tau+\Delta\tau}x_3\,{}^{\tau+\Delta\tau}n_i\delta u_i d\,{}^{\tau+\Delta\tau}S_W = \int_{{}^{\tau}S_W} \rho_W g({}^{\tau}x_3 + u_3)\det({}^{\tau+\Delta\tau}_{\tau}x_{ij})\,{}^{\tau}_{\tau+\Delta\tau}x_{ji}\,{}^{\tau}n_j\delta u_i d\,{}^{\tau}S_W\ . \tag{2-12} $$

In Eq. (2-12), the term $\det({}^{\tau+\Delta\tau}_{\tau}x_{ij})\,{}^{\tau}_{\tau+\Delta\tau}x_{ji}$ can be approximated as

$$ \det({}^{\tau+\Delta\tau}_{\tau}x_{ij})\,{}^{\tau}_{\tau+\Delta\tau}x_{ji} \approx \delta_{ij} + {}_{\tau}Q_{ij} \quad \text{with} \quad {}_{\tau}Q_{ij} = \delta_{ij}\frac{\partial u_k}{\partial {}^{\tau}x_k} - \frac{\partial u_j}{\partial {}^{\tau}x_i} \tag{2-13} $$

by utilizing the following relations

$$ \det({}^{\tau+\Delta\tau}_{\tau}x_{ij}) \approx 1 + \frac{\partial u_k}{\partial {}^{\tau}x_k} + \ldots\ldots \quad \text{and} \quad {}^{\tau}_{\tau+\Delta\tau}x_{ij} \approx \delta_{ij} - \frac{\partial u_i}{\partial {}^{\tau}x_j} + \ldots\ldots . $$

Substituting Eq. (2-13) into Eq. (2-12) and linearizing the resulting equation with respect to u_i , the first term in Eq. (2-3c) becomes

$$ \begin{aligned} &\int_{{}^{\tau+\Delta\tau}S_W} \rho_W g\,{}^{\tau+\Delta\tau}x_3\,{}^{\tau+\Delta\tau}n_i\delta u_i d\,{}^{\tau+\Delta\tau}S_W \approx \\ &\qquad \int_{{}^{\tau}S_W} \rho_W g\,{}^{\tau}x_3\,{}^{\tau}n_i\delta u_i d\,{}^{\tau}S_W + \int_{{}^{\tau}S_W} \rho_W g\,{}^{\tau}x_3\,{}_{\tau}Q_{ij}\,{}^{\tau}n_j\delta u_i d\,{}^{\tau}S_W \\ &\qquad + \int_{{}^{\tau}S_W} \rho_W g u_3\,{}^{\tau}n_i\delta u_i d\,{}^{\tau}S_W\ . \end{aligned} \tag{2-14} $$

Similarly, the second term in Eq. (2-3c) is linearized with respect to u_i and ${}^{\tau+\Delta\tau}P_D$ as

$$-\int_{{}^{\tau+\Delta\tau}S_W} {}^{\tau+\Delta\tau}P_D \, {}^{\tau+\Delta\tau}n_i \delta u_i d\, {}^{\tau+\Delta\tau}S_W =$$

$$-\int_{{}^{\tau}S_W} {}^{\tau+\Delta\tau}P_D \det({}^{\tau+\Delta\tau}_{\tau}x_{ij})\, {}_{\tau+\Delta\tau}^{\tau}x_{ji} \, {}^{\tau}n_j \delta u_i d\, {}^{\tau}S_W \approx$$

$$-\int_{{}^{\tau}S_W} {}^{\tau+\Delta\tau}P_D (\delta_{ij} + {}_{\tau}Q_{ij}) \, {}^{\tau}n_j \delta u_i d\, {}^{\tau}S_W \approx$$

$$-\int_{{}^{\tau}S_W} {}^{\tau+\Delta\tau}P_D \, {}^{\tau}n_i \delta u_i d\, {}^{\tau}S_W \,. \qquad (2\text{-}15)$$

Other terms in Eqs. (2-3b) and (2-3d) are simply linearized by setting ${}^{\tau+\Delta\tau}V_S \to {}^{\tau}V_S$, ${}^{\tau+\Delta\tau}S_S \to {}^{\tau}S_S$, and ${}^{\tau+\Delta\tau}S_W \to {}^{\tau}S_W$. Using ${}^{\tau+\Delta\tau}\ddot{x}_i = \ddot{u}_i$ in Eq. (2-3b) and substituting Eqs. (2-14) and (2-15) into Eq. (2-3), the following incremental equilibrium equation is finally obtained

$$\int_{{}^{\tau}V_S} \rho_S \ddot{u}_i \delta u_i d\, {}^{\tau}V_S + \int_{{}^{\tau}V_S} C_{ijkl} \, {}_{\tau}e_{kl} \delta \, {}_{\tau}e_{ij} d\, {}^{\tau}V_S + \int_{{}^{\tau}V_S} {}^{\tau}\sigma_{ij} \delta \, {}_{\tau}\eta_{ij} d\, {}^{\tau}V_S$$

$$-\int_{{}^{\tau}S_W} \rho_W g \, {}^{\tau}x_3 \, {}_{\tau}Q_{ij} \, {}^{\tau}n_j \delta u_i d\, {}^{\tau}S_W - \int_{{}^{\tau}S_W} \rho_W g u_3 \, {}^{\tau}n_i \delta u_i d\, {}^{\tau}S_W + \int_{{}^{\tau}S_W} {}^{\tau+\Delta\tau}P_D \, {}^{\tau}n_i \delta u_i d\, {}^{\tau}S_W =$$

$$-\int_{{}^{\tau}V_S} \rho_S g \delta u_3 d\, {}^{\tau}V_S + \int_{{}^{\tau}S_W} \rho_W g \, {}^{\tau}x_3 \, {}^{\tau}n_i \delta u_i d\, {}^{\tau}S_W + \int_{{}^{\tau}V_S} {}^{\tau+\Delta\tau}f_i^B \delta u_i d\, {}^{\tau}V_S$$

$$+\int_{{}^{\tau}S_S} {}^{\tau+\Delta\tau}f_i^S \delta u_i d\, {}^{\tau}S_S - \int_{{}^{\tau}V_S} {}^{\tau}\sigma_{ij} \delta \, {}_{\tau}e_{ij} d\, {}^{\tau}V_S \qquad (2\text{-}16)$$

The hydrostatic and hydrodynamic equilibrium equations are subsequently derived from Eq. (2-16) in an integrated manner. Eq. (2-16) considers all the external forces which can be applied to floating structures.

2.1.2. Hydrostatic equilibrium equation

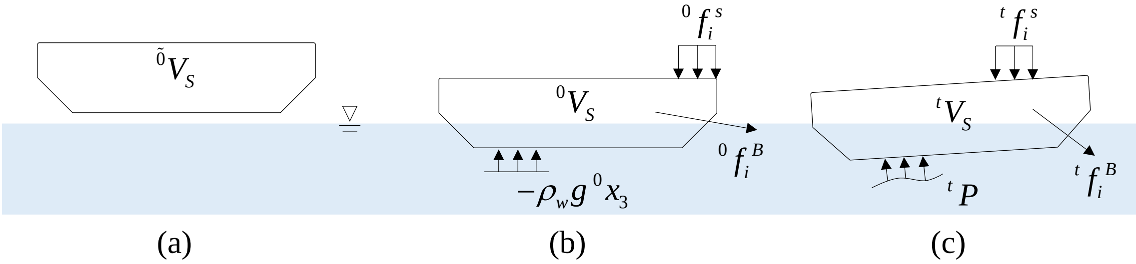

Fig. 2-2. Three equilibrium states: initial state, hydrostatic equilibrium state, and hydrodynamic equilibrium state.

Let us define three states, namely, the initial state, hydrostatic equilibrium state, and hydrodynamic equilibrium state, as shown in Fig. 2-2. The initial state is an arbitrary configuration in which the structure does not contact the external fluid. In the hydrostatic equilibrium state, the structure is floating in the external fluid without motion. The structure is moving due to incident waves in the hydrodynamic equilibrium state.

From a given initial state at time $\tilde{0}$, we can find the hydrostatic equilibrium state at time 0 through incremental nonlinear analysis, allowing large displacements and large rotations. The hydrostatic equilibrium equation can be derived with the condition of zero acceleration ($\ddot{u}_i = 0$) and zero hydrodynamic pressure (${}^{\tau+\Delta\tau}P_D = 0$). The following incremental equilibrium equation for the nonlinear hydrostatic static analysis can be obtained from Eq. (2-16),

$$
\begin{aligned}
&\int_{{}^{\tau}V_S} C_{ijkl}\, {}_{\tau}e_{kl}\, \delta\, {}_{\tau}e_{ij}\, d\, {}^{\tau}V_S + \int_{{}^{\tau}V_S} {}^{\tau}\sigma_{ij}\, \delta\, {}_{\tau}\eta_{ij}\, d\, {}^{\tau}V_S \\
&-\int_{{}^{\tau}S_W} \rho_W g\, {}^{\tau}x_3\, {}_{\tau}Q_{ij}\, {}^{\tau}n_j\, \delta u_i\, d\, {}^{\tau}S_W - \int_{{}^{\tau}S_W} \rho_W g u_3\, {}^{\tau}n_i\, \delta u_i\, d\, {}^{\tau}S_W = \\
&\qquad -\int_{{}^{\tau}V_S} \rho_S g\, \delta u_3\, d\, {}^{\tau}V_S + \int_{{}^{\tau}S_W} \rho_W g\, {}^{\tau}x_3\, {}^{\tau}n_i\, \delta u_i\, d\, {}^{\tau}S_W \\
&\qquad +\int_{{}^{\tau}V_S} {}^{\tau+\Delta\tau}f_i^{B}\, \delta u_i\, d\, {}^{\tau}V_S + \int_{{}^{\tau}S_S} {}^{\tau+\Delta\tau}f_i^{S}\, \delta u_i\, d\, {}^{\tau}S_S - \int_{{}^{\tau}V_S} {}^{\tau}\sigma_{ij}\, \delta\, {}_{\tau}e_{ij}\, d\, {}^{\tau}V_S\,. \qquad (2\text{-}17)
\end{aligned}
$$

The hydrostatic equilibrium equation involves nonlinear effects mainly due to the wet surface change. Therefore, an iterative solution procedure should be employed. After the hydrostatic analysis, we obtain the hydrostatic equilibrium configuration from the initial state configuration.

In the hydrostatic equilibrium state, the following equation is satisfied

$$-\int_{{}^0V_S} \rho_S g \delta u_3 d\,{}^0V_S + \int_{{}^0S_W} \rho_W g\,{}^0x_3\,{}^0n_i \delta u_i d\,{}^0S_W$$

$$+\int_{{}^0V_S} {}^0f_i^B \delta u_i d\,{}^0V_S + \int_{{}^0S_S} {}^0f_i^S \delta u_i d\,{}^0S_S - \int_{{}^0V_S} {}^0\sigma_{ij} \delta\,{}_0e_{ij} d\,{}^0V_S = 0\,. \tag{2-18}$$

That is, the right hand side of Eq. (2-18) becomes zero in the hydrostatic equilibrium configuration at time 0.

2.1.3. Hydrodynamic equilibrium equation

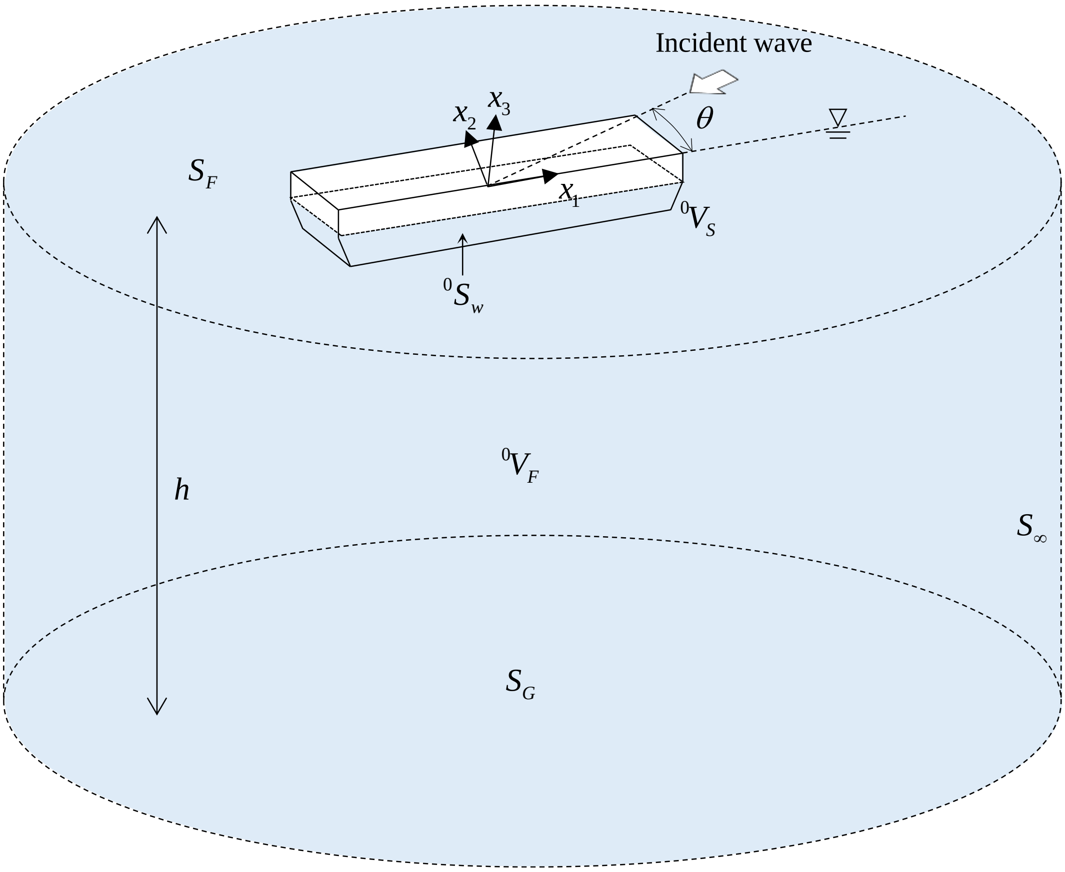

Fig. 2-3. Floating structure under incident wave.

As shown Fig. 2-3, there is a floating structure on the water of depth h. Fluid flow is assumed to be irrotational, inviscid, and incompressible, allowing the use of potential flow theory. The incident regular wave comes continuously from the positive x_1-axis with an angle θ and its amplitude is small enough to adopt the linear wave theory. Only gravity waves are considered, neglecting the surface tension effect. The atmospheric pressure is assumed to be zero.

The volumes occupied by the structure and fluid are denoted as V_S and V_F, respectively. The fluid volume V_F is surrounded by the wet surface S_W, free surface S_F, seabed S_G, and infinite boundary S_∞.

Hydrodynamic analysis is performed in the frequency domain. It is assumed that the motion of the floating structure is small and wet surface change is negligible [11, 18].

Setting $\tau \to 0$ and $\tau + \Delta\tau \to t$ in Eq. (2-16), substituting Eq. (2-18) into the resulting equation, and using ${}^{t}f_i^B = {}^{0}f_i^B + {}^{t}\tilde{f}_i^B$ and ${}^{t}f_i^S = {}^{0}f_i^S + {}^{t}\tilde{f}_i^S$, the following hydrodynamic equilibrium equation is obtained

$$\int_{{}^0V_S} \rho_S \ddot{u}_i \delta u_i d\,{}^0V_S + \int_{{}^0V_S} C_{ijkl}\,{}_0e_{kl}\delta\,{}_0e_{ij} d\,{}^0V_S + \int_{{}^0V_S} {}^0\sigma_{ij}\delta\,{}_0\eta_{ij} d\,{}^0V_S$$
$$-\int_{{}^0S_W} \rho_W g\,{}^0x_3\,{}_0Q_{ij}\,{}^0n_j \delta u_i d\,{}^0S_W - \int_{{}^0S_W} \rho_W g u_3\,{}^0n_i \delta u_i d\,{}^0S_W + \int_{{}^0S_W} {}^tP_D\,{}^0n_i \delta u_i d\,{}^0S_W =$$
$$\int_{{}^0V_S} {}^t\tilde{f}_i^B \delta u_i d\,{}^0V_S + \int_{{}^0S_S} {}^t\tilde{f}_i^S \delta u_i d\,{}^0S_S\,, \tag{2-19}$$

in which ${}^0f_i^B$ and ${}^t\tilde{f}_i^B$ are static and dynamic parts of the body force, respectively, and ${}^0f_i^S$ and ${}^t\tilde{f}_i^S$ are static and dynamic parts of the surface force, respectively.

It is important to note that the reference configuration for the hydrodynamic analysis is the hydrostatic equilibrium configuration. That is, in the hydrodynamic analysis, u_i is the displacement from the configuration at time 0 to the configuration at time t ($u_i = {}^tx_i - {}^0x_i$).

Invoking a harmonic response for angular frequency ω ($u_i = \mathrm{Re}\{\hat{u}_i({}^0x_i)e^{\hat{j}\omega t}\}$; $\hat{j} = \sqrt{-1}$), we obtain the following steady state hydrodynamic equilibrium equation

$$-\omega^2 \int_{{}^0V_S} \rho_S \hat{u}_i \delta u_i d\,{}^0V_S + \int_{{}^0V_S} C_{ijkl}\,{}_0\hat{e}_{kl}\delta\,{}_0e_{ij} d\,{}^0V_S + \int_{{}^0V_S} {}^0\sigma_{ij}\delta\,{}_0\hat{\eta}_{ij} d\,{}^0V_S$$
$$-\int_{{}^0S_W} \rho_W\,{}^0x_3\,{}_0\hat{Q}_{ij}\,{}^0n_j \delta u_i d\,{}^0S_W - \int_{{}^0S_W} \rho_W g \hat{u}_3\,{}^0n_i \delta u_i d\,{}^0S_W + \int_{{}^0S_W} \hat{P}_D\,{}^0n_i \delta u_i d\,{}^0S_W =$$
$$\int_{{}^0V_S} {}^t\hat{f}_i^B \delta u_i d\,{}^0V_S + \int_{{}^0S_S} {}^t\hat{f}_i^S \delta u_i d\,{}^0S_S \tag{2-20}$$

with

$${}_0e_{ij} = \mathrm{Re}\{{}_0\hat{e}_{ij}({}^0x_i)e^{\hat{j}\omega t}\},\ {}_0Q_{ij} = \mathrm{Re}\{{}_0\hat{Q}_{ij}({}^0x_i)e^{\hat{j}\omega t}\},\ {}^tP_D = \mathrm{Re}\{\hat{P}_D({}^0x_i)e^{\hat{j}\omega t}\},$$
$${}_0\eta_{ij} = \mathrm{Re}\{{}_0\hat{\eta}_{ij}({}^0x_i)e^{\hat{j}\omega t}\},\ {}^t\tilde{f}_i^B = \mathrm{Re}\{\hat{f}_i^B({}^0x_i)e^{\hat{j}\omega t}\},\ {}^t\tilde{f}_i^S = \mathrm{Re}\{\hat{f}_i^S({}^0x_i)e^{\hat{j}\omega t}\}.$$

It is important to note that ${}^0\sigma_{ij}$ in Eq (2-20) is obtained from solutions of the hydrostatic analysis. Doing so, a complete hydrostatic stiffness can be constructed for hydrodynamic analysis.

In the steady state, the velocity potential $\phi(t) = \mathrm{Re}\{\hat{\phi}({}^0x_i)e^{\hat{j}\omega t}\}$ is governed by

$$\nabla^2\hat{\phi} = 0 \qquad \text{in } {}^0V_F\,, \tag{2-21a}$$

$$\frac{\partial\hat{\phi}}{\partial x_3} = \frac{\omega^2}{g}\hat{\phi} \qquad \text{on } S_F\ (x_3 = 0), \tag{2-21b}$$

$$\frac{\partial \hat{\phi}}{\partial x_3} = 0 \qquad \text{on } S_G \ \ (x_3 = -h), \tag{2-21c}$$

$$\sqrt{R}\left(\frac{\partial}{\partial R} + \hat{j}\hat{k}\right)(\hat{\phi} - \hat{\phi}^I) = 0 \qquad \text{on } S_\infty \ \ (R \to \infty), \tag{2-21d}$$

$$\frac{\partial \hat{\phi}}{\partial\, {}^0 n} = \hat{j}\omega \hat{u}_i\, {}^0 n_i \qquad \text{on } {}^0 S_W , \tag{2-21e}$$

where $\hat{k}$ is the wave number and $\phi^I(t) = \mathrm{Re}\{\hat{\phi}^I({}^0 x_i)e^{\hat{j}\omega t}\}$ is the velocity potential for an incident wave. Eq. (2-21b) is the combined free surface boundary condition linearized at $x_3 = 0$, Eq. (2-21d) is derived from the Sommerfeld radiation condition, and Eq. (2-21e) describes the condition in which the normal velocities of the structure and the external fluid must be the same on the wet surface.

The incident velocity potential $\hat{\phi}^I$ is defined by (see, e.g., Refs. [27, 28])

$$\hat{\phi}^I = \hat{j}\frac{ga}{\omega}\frac{\cosh \hat{k}(x_3 + h)}{\cosh \hat{k}h} e^{\hat{j}\hat{k}(x_1 \cos\theta + x_2 \sin\theta)} \quad \text{for the finite depth case,} \tag{2-22}$$

and

$$\hat{\phi}^I = \hat{j}\frac{ga}{\omega} e^{\hat{k}x_3} e^{\hat{j}\hat{k}(x_1 \cos\theta + x_2 \sin\theta)} \quad \text{for the infinite depth case,} \tag{2-23}$$

where a is the amplitude of the incident wave.

The corresponding boundary integral equation is given by

$$\alpha\hat{\phi}(x_i) - P.V.\int_{{}^0 S_W} \frac{\partial G(x_i;\xi_i)}{\partial\, {}^0 n(\xi_i)}\hat{\phi}(\xi_i)\, d\, {}^0 S_\xi = -P.V.\int_{{}^0 S_W} G(x_i;\xi_i)\frac{\partial \hat{\phi}(\xi_i)}{\partial\, {}^0 n(\xi_i)}\, d\, {}^0 S_\xi + 4\pi\hat{\phi}^I(x_i)$$

$$\text{for } x_i \text{ on } {}^0 S_W , \tag{2-24}$$

in which α is the solid angle, $P.V.$ refers to the Cauchy principal value, and $G(x_i;\xi_i)$ is Green's function, which is located at position ξ_i and generated by a source potential with strength -4π and angular frequency ω. The subscript ξ shows that the integration is performed with respect to variable ξ_i on the wet surface ${}^0 S_W$. Detailed procedure to obtain the Green's function in finite and infinite depth cases is described well in Ref. [28].

Multiplying a test function $\delta\hat{\phi}(x_i)$ to Eq. (2-24) and integrating over the wet surface ${}^0 S_W$, the following equations are obtained:

$$\int_{{}^0 S_W} \alpha\hat{\phi}(x_i)\delta\hat{\phi}(x_i)\, d\, {}^0 S_x - \int_{{}^0 S_W} P.V.\int_{{}^0 S_W} \left(\frac{\partial G(x_i;\xi_i)}{\partial\, {}^0 n(\xi_i)}\hat{\phi}(\xi_i) - G(x_i;\xi_i)\frac{\partial \hat{\phi}(\xi_i)}{\partial\, {}^0 n(\xi_i)} \right) dS_\xi\, \delta\hat{\phi}(x_i)\, d\, {}^0 S_x =$$

$$4\pi\int_{{}^0S_W}\hat{\phi}^I(x_i)\delta\hat{\phi}(x_i)d\,{}^0S_x \quad \text{for } x_i \text{ on } {}^0S_W\,, \tag{2-25}$$

where the subscript x denotes that the integration is performed with respect to variable x_i on the wet surface ${}^0S_W$.

Using the linearized Bernoulli equation, the hydrodynamic pressure $\hat{P}_D$ can be expressed as

$$\hat{P}_D = -\hat{j}\omega\rho_W\hat{\phi}\,. \tag{2-26}$$

Substituting Eq. (2-26) into Eq. (2-20) and Eq. (2-21e) into Eq. (2-25), the following direct-coupled equations are finally obtained

$$\begin{aligned}
&-\omega^2\int_{{}^0V_S}\rho_S\hat{u}_i\delta u_i d\,{}^0V_S + \int_{{}^0V_S}C_{ijkl}\,{}_0\hat{e}_{kl}\delta\,{}_0e_{ij}d\,{}^0V_S + \int_{{}^0V_S}{}^0\sigma_{ij}\delta\,{}_0\hat{\eta}_{ij}d\,{}^0V_S \\
&-\int_{{}^0S_W}\rho_W\,{}^0x_3\,{}_0\hat{Q}_{ij}\,{}^0n_j\delta u_i d\,{}^0S_W - \int_{{}^0S_W}\rho_W g\hat{u}_3\,{}^0n_i\delta u_i d\,{}^0S_W - \hat{j}\omega\int_{{}^0S_W}\rho_W\hat{\phi}\,{}^0n_i\delta u_i d\,{}^0S_W = \\
&\qquad \int_{{}^0V_S}{}^t\hat{f}_i^B\delta u_i d\,{}^0V_S + \int_{{}^0S_S}{}^t\hat{f}_i^S\delta u_i d\,{}^0S_S\,,
\end{aligned} \tag{2-27}$$

$$\begin{aligned}
&\int_{{}^0S_W}\alpha\hat{\phi}(x_i)\delta\hat{\phi}(x_i)d\,{}^0S_x \\
&-\int_{{}^0S_W}P.V.\int_{{}^0S_W}\left(\frac{\partial G(x_i;\xi_i)}{\partial\,{}^0n(\xi_i)}\hat{\phi}(\xi_i) - \hat{j}\omega G(x_i;\xi_i)\hat{u}_i(\xi_i)\,{}^0n_i(\xi_i)\right)dS_\xi\delta\hat{\phi}(x_i)d\,{}^0S_x = \\
&\qquad 4\pi\int_{{}^0S_W}\hat{\phi}^I(x_i)\delta\hat{\phi}(x_i)d\,{}^0S_x \quad \text{for } x_i \text{ on } {}^0S_W\,.
\end{aligned} \tag{2-28}$$

2.2. Discretization

In this section, the hydrostatic equilibrium equation in Eq. (2-17) is discretized using the finite element method for hydrostatic analysis. The direct-coupled equations in Eqs. (2-27)-(2-28) are discretized using the finite and boundary element methods for hydrodynamic analysis.

2.2.4. Finite element discretization for hydrostatic analysis

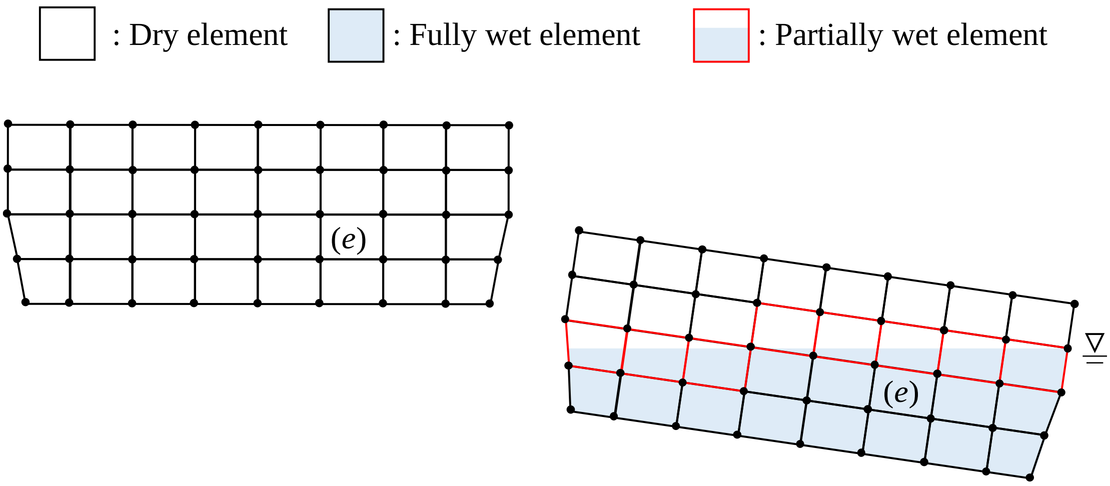

Fig. 2-4. Finite element discretization for hydrostatic analysis : (a) initial state; (b) hydrostatic equilibrium state.

The floating structure is discretized using N finite elements including M wet elements facing the wet surface (including partially or fully wet elements), as shown in Fig. 2-4. For a finite element (e), the increments of the structural displacements and strains are interpolated as

$$u_i^{(e)} = \mathbf{H}_i^{(e)} \mathbf{u}^{(e)}, \quad \delta u_i^{(e)} = \mathbf{H}_i^{(e)} \delta \mathbf{u}^{(e)},$$

$${}_{\tau}e_{ij}^{(e)} = {}^{\tau}\mathbf{B}_{ij}^{(e)} \mathbf{u}^{(e)}, \quad \delta\, {}_{\tau}\eta_{ij}^{(e)} = \delta \mathbf{u}^{(e)\mathrm{T}}\, {}^{\tau}\mathbf{N}_{ij}^{(e)} \mathbf{u}^{(e)}, \tag{2-29}$$

where $\mathbf{u}^{(e)}$ is the incremental nodal displacement vector for element (e), $\mathbf{H}_i^{(e)}$ is the displacement interpolation matrix, and ${}^{\tau}\mathbf{B}_{ij}^{(e)}$ and ${}^{\tau}\mathbf{N}_{ij}^{(e)}$ are the linear and nonlinear strain-displacement relation matrices, respectively.

Substituting Eq. (2-29) into Eq. (2-17) and applying the standard finite element procedure, the following incremental equilibrium equation is obtained

$${}^{\tau}\mathbf{K}\mathbf{U} = {}^{\tau+\Delta\tau}\mathbf{R} - {}^{\tau}\mathbf{F} \tag{2-30}$$

with

$${}^{\tau}\mathbf{K} = {}^{\tau}\mathbf{S}_K + {}^{\tau}\mathbf{S}_{KN} - {}^{\tau}\mathbf{S}_{HN} - {}^{\tau}\mathbf{S}_{HD},$$

$${}^{\tau+\Delta\tau}\mathbf{R} = -{}^{\tau+\Delta\tau}\mathbf{R}_G + {}^{\tau+\Delta\tau}\mathbf{R}_{HS} + {}^{\tau+\Delta\tau}\mathbf{R}_B + {}^{\tau+\Delta\tau}\mathbf{R}_S,$$

in which ${}^{\tau}\mathbf{K}$ is the tangential stiffness matrix including the linear stiffness (${}^{\tau}\mathbf{S}_K$), the nonlinear geometric stiffness (${}^{\tau}\mathbf{S}_{KN}$), and the hydrostatic stiffness terms: ${}^{\tau}\mathbf{S}_{HN}$ and ${}^{\tau}\mathbf{S}_{HD}$ resulting from the wet surface change and buoyancy change, respectively, and $\mathbf{U}$ is the incremental nodal displacement vector for the whole model. In addition, the external force vector ${}^{\tau+\Delta\tau}\mathbf{R}$ includes the gravity (${}^{\tau+\Delta\tau}\mathbf{R}_G$), buoyancy force (${}^{\tau+\Delta\tau}\mathbf{R}_{HS}$), body force (${}^{\tau+\Delta\tau}\mathbf{R}_B$), and surface force (${}^{\tau+\Delta\tau}\mathbf{R}_S$) vectors, and ${}^{\tau}\mathbf{F}$ is the internal force vector. Note that ${}^{\tau}\mathrm{S}_{CH} = {}^{\tau}\mathrm{S}_{KN} - {}^{\tau}\mathrm{S}_{HN} - {}^{\tau}\mathrm{S}_{HD}$ is the complete hydrostatic stiffness for the floating structure.

Assume that the wet elements are numbered 1 to M, and the remaining elements are assigned numbers $M+1$ through N. The matrices and vectors in Eq. (2-30) are evaluated by

$${}^{\tau}\mathbf{S}_K = \mathop{\mathrm{A}}_{e=1}^{N} \int_{{}^{\tau}V_S^{(e)}} {}^{\tau}\mathbf{B}_{ij}^{(e)\mathrm{T}} C_{ijkl}^{(e)}\, {}^{\tau}\mathbf{B}_{kl}^{(e)} d\, {}^{\tau}V_S \,, \tag{2-31a}$$

$${}^{\tau}\mathbf{S}_{KN} = \mathop{\mathrm{A}}_{e=1}^{N} \int_{{}^{\tau}V_S^{(e)}} {}^{\tau}\mathbf{N}_{ij}^{(e)}\, {}^{\tau}\sigma_{ij}^{(e)} d\, {}^{\tau}V_S \,, \tag{2-31b}$$

$${}^{\tau}\mathbf{S}_{HN} = \mathop{\mathrm{A}}_{e=1}^{M} \int_{{}^{\tau}S_W^{(e)}} \rho_W\, g\, {}^{\tau}x_3 \mathbf{H}_i^{(e)\mathrm{T}}\, {}_{\tau}\mathbf{D}_i^{(e)} d\, {}^{\tau}S_W \,, \tag{2-31c}$$

$${}^{\tau}\mathbf{S}_{HD} = \mathop{\mathrm{A}}_{e=1}^{M} \int_{{}^{\tau}S_W^{(e)}} \rho_W\, g \mathbf{H}_i^{(e)\mathrm{T}}\, {}^{\tau}n_i^{(e)} \mathbf{H}_3^{(e)} d\, {}^{\tau}S_W \,, \tag{2-31d}$$

$${}^{\tau+\Delta\tau}\mathbf{R}_G = \mathop{\mathrm{A}}_{e=1}^{N} \int_{{}^{\tau}V_S^{(e)}} {}^{\tau}\rho_S^{(e)} g \mathbf{H}_3^{(e)\mathrm{T}} d\, {}^{\tau}V_S \,, \tag{2-31e}$$

$${}^{\tau+\Delta\tau}\mathbf{R}_{HS} = \mathop{\mathrm{A}}_{e=1}^{M} \int_{{}^{\tau}S_W^{(e)}} \rho_W\, g\, {}^{\tau}x_3\, {}^{\tau}n_i^{(e)} \mathbf{H}_i^{(e)\mathrm{T}} d\, {}^{\tau}S_W \,, \tag{2-31f}$$

$${}^{\tau+\Delta\tau}\mathbf{R}_B = \mathop{\mathrm{A}}_{e=1}^{N} \int_{{}^{\tau}V_S^{(e)}} \mathbf{H}_i^{(e)\mathrm{T}}\, {}^{\tau+\Delta\tau}\mathbf{f}_i^{B(e)} d\, {}^{\tau}V_S \,, \tag{2-31g}$$

$${}^{\tau+\Delta\tau}\mathbf{R}_S = \mathop{\mathrm{A}}_{e=1}^{N} \int_{{}^{\tau}S_S^{(e)}} \mathbf{H}_i^{(e)\mathrm{T}}\, {}^{\tau+\Delta\tau}\mathbf{f}_i^{S(e)} d\, {}^{\tau}S_S \,, \tag{2-31h}$$

$${}^{\tau}\mathbf{F} = \mathop{\mathrm{A}}_{e=1}^{N} \int_{{}^{\tau}V_S^{(e)}} {}^{\tau}\mathbf{B}_{ij}^{(e)\mathrm{T}}\, {}^{\tau}\sigma_{ij}^{(e)} d\, {}^{\tau}V_S \,, \tag{2-31i}$$

where A is the finite element (FE) assembly operator, ${}^{\tau}S_W^{(e)}$ denotes the wet surface part of the element, $C_{ijkl}^{(e)}$ is the material law tensor, $\mathbf{H}_3^{(e)}$ is the interpolation matrix for the displacement component u_3, and ${}^{\tau}\sigma_{ij}^{(e)}$ is the Cauchy stress tensor. Note that ${}^{\tau}n_j\, {}_{\tau}Q_{ij} = n_i \dfrac{\partial u_k}{\partial^{\tau} x_k} - n_j \dfrac{\partial u_j}{\partial^{\tau} x_i} = {}_{\tau}\mathbf{D}_i^{(e)} \mathbf{u}^{(e)}$ is used to derive Eq. (2-31c).

From Eq. (2-30), the incremental equilibrium equation is obtained for the rigid body hydrostatic analysis

[15]

$$ {}^{\tau}\bar{\mathbf{K}}\bar{\mathbf{U}} = {}^{\tau+\Delta\tau}\bar{\mathbf{R}} \tag{2-32} $$

with ${}^{\tau}\bar{\mathbf{K}} = \bar{\boldsymbol{\psi}}^{\mathrm{T}}\, {}^{\tau}\mathbf{S}_{CH}\, \bar{\boldsymbol{\psi}}$, $\mathbf{U} = \bar{\boldsymbol{\psi}}\bar{\mathbf{U}} = q_1^R \bar{\boldsymbol{\psi}}_1 + \cdots + q_6^R \bar{\boldsymbol{\psi}}_6$, ${}^{\tau+\Delta\tau}\bar{\mathbf{R}} = \bar{\boldsymbol{\psi}}^{\mathrm{T}}\, {}^{\tau+\Delta\tau}\mathbf{R}$,

in which $\bar{\boldsymbol{\psi}}_i$ $(i = 1, 2, ..., 6)$ is the basis vector for the i-th rigid body mode, $\bar{\boldsymbol{\psi}}$ is the matrix containing $\bar{\boldsymbol{\psi}}_1$ to $\bar{\boldsymbol{\psi}}_6$, and $\bar{\mathbf{U}} = \begin{bmatrix} q_1^R & q_2^R & q_3^R & q_4^R & q_5^R & q_6^R \end{bmatrix}^{\mathrm{T}}$ is the generalized coordinate vector for six rigid body motions (heave, sway, surge, roll, pitch, and yaw).

The incremental equilibrium equations in Eqs. (2-30) and (2-32) are solved using the standard Newton-Raphson method until an energy criterion is satisfied [15, 26].

2.2.5. Finite and boundary element discretization for hydrodynamic analysis

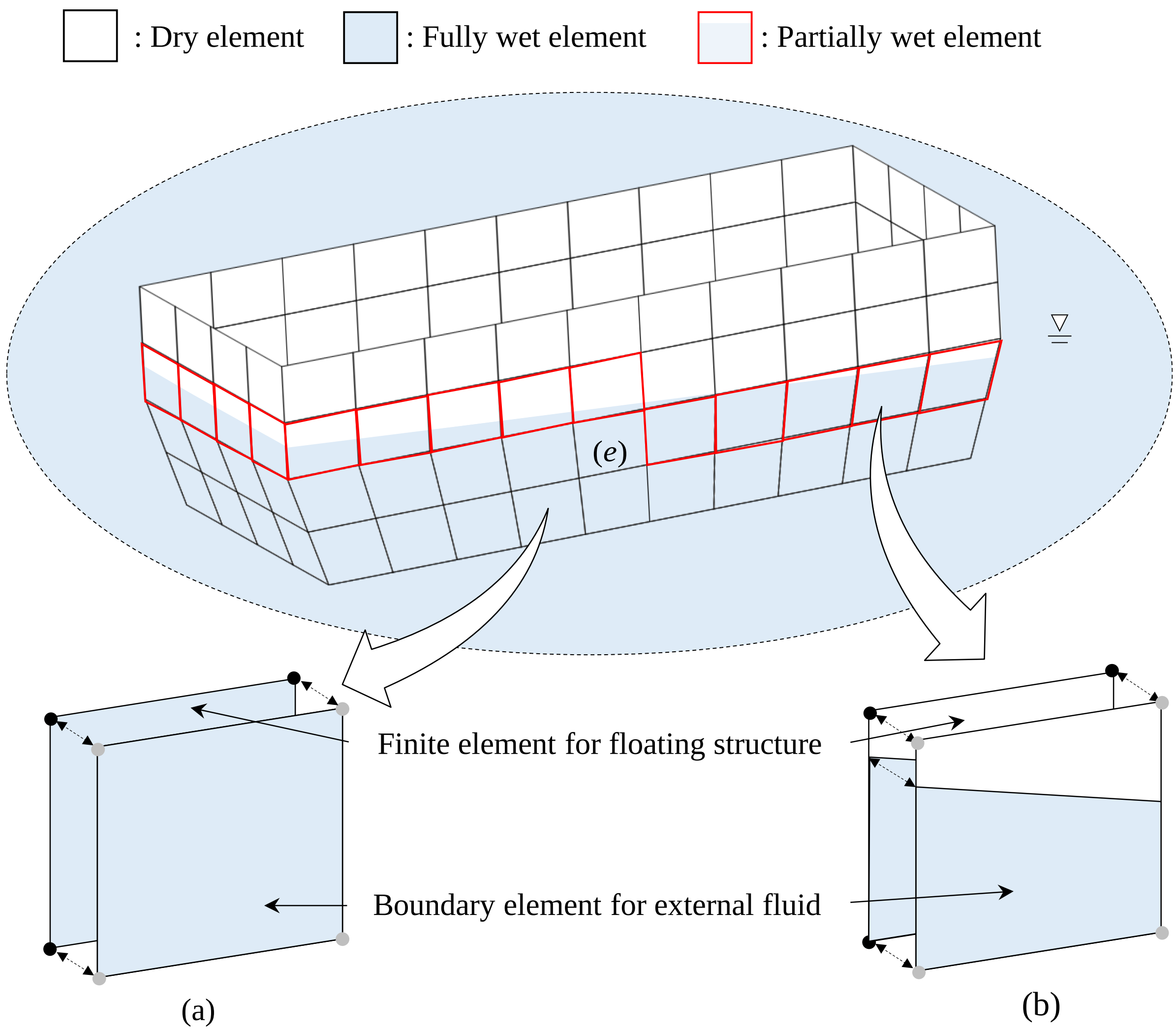

Fig. 2.5. Finite element and boundary element discretizations, and mesh connection : (a) fully wet element; (b) partially wet element

The floating structure is modeled using N finite elements and the external fluid is modeled using M boundary elements (corresponding to the wet elements). The finite and boundary element meshes are connected through the wet surface, as depicted in Fig. 2-5. The fields of structural displacements and fluid velocity potential are interpolated using the nodal displacement vector ($\hat{\mathbf{u}}$) and the nodal velocity potential vector ($\hat{\boldsymbol{\varphi}}$), respectively.

For an element (e), the structural displacement $\hat{u}_i^{(e)}$ and the velocity potential $\hat{\phi}^{(e)}$ are interpolated as

$$\hat{u}_i^{(e)} = \mathbf{H}_i^{(e)}\hat{\mathbf{u}}^{(e)}, \tag{2-33}$$

$$\hat{\phi}^{(e)} = \mathrm{P}^{(e)}\hat{\boldsymbol{\varphi}}^{(e)}, \tag{2-34}$$

where $\mathbf{P}^{(e)}$ is the velocity potential interpolation matrix used for the boundary element, and $\hat{\mathbf{u}}^{(e)}$ and $\hat{\boldsymbol{\varphi}}^{(e)}$ are the nodal displacement and velocity potential vectors for element (e), respectively.

Substituting Eqs. (2-33) and (2-34) into Eqs. (2-27) and (2-28), respectively, the following discrete coupled equation for the steady state problem can be obtained

$$\begin{bmatrix} -\omega^2\,{}^0\mathrm{S}_M + {}^0\mathrm{S}_K + {}^0\mathrm{S}_{CH} & \hat{j}\omega\,{}^0\mathrm{S}_D \\ \hat{j}\omega\,{}^0\mathrm{F}_G & {}^0\mathrm{F}_M - {}^0\mathrm{F}_{Gn} \end{bmatrix}\begin{bmatrix} \hat{\mathbf{U}} \\ \hat{\boldsymbol{\Phi}} \end{bmatrix} = \begin{bmatrix} {}^t\mathbf{R}_B + {}^t\mathbf{R}_S \\ 4\pi\,{}^t\mathrm{R}_I \end{bmatrix} \tag{2-35}$$

with ${}^0\mathrm{S}_{CH} = {}^0\mathrm{S}_{KN} - {}^0\mathrm{S}_{HN} - {}^0\mathrm{S}_{HD}$,
where $\hat{\mathbf{U}}$ and $\hat{\boldsymbol{\Phi}}$ denote nodal displacement and velocity potential vectors, respectively, for the whole model, ${}^0\mathbf{S}_M$ is the mass matrix, and ${}^0\mathrm{S}_{CH}$ is the complete hydrostatic stiffness matrix including the hydrostatic stiffness terms (${}^0\mathrm{S}_{HN}$ and ${}^0\mathrm{S}_{HD}$) and the geometric stiffness (${}^0\mathrm{S}_{KN}$). Note that the superscript 0 denotes the configuration of the hydrostatic equilibrium state. $\mathbf{U}$ is the incremental nodal displacement vector for the whole model.

Submatrices and vectors in Eq. (2-35) are obtained using the following equations

$${}^0\mathbf{S}_M = \mathop{\mathrm{A}}_{e=1}^{N}\int_{{}^0V_S^{(e)}} {}^0\rho_S \mathbf{H}_i^{(e)\mathrm{T}}\mathbf{H}_i^{(e)} d\,{}^0V_S\,, \tag{2-36a}$$

$${}^0\mathbf{S}_K = \mathop{\mathrm{A}}_{e=1}^{N}\int_{{}^0V_S^{(e)}} {}^0\mathbf{B}_{ij}^{(e)\mathrm{T}} C_{ijkl}^{(e)}\,{}^0\mathbf{B}_{kl}^{(e)} d\,{}^0V_S\,, \tag{2-36b}$$

$${}^0\mathbf{S}_{KN} = \mathop{\mathrm{A}}_{e=1}^{N}\int_{{}^0V_S^{(e)}} {}^0\mathbf{N}_{ij}^{(e)}\,{}^0\sigma_{ij}^{(e)} d\,{}^0V_S\,. \tag{2-36c}$$

$${}^0\mathbf{S}_{HN} = \mathop{\mathrm{A}}_{e=1}^{M}\int_{{}^0S_W^{(e)}} \rho_W g\,{}^0x_3 \mathbf{H}_i^{(e)\mathrm{T}}\,{}_0\mathbf{D}_i d\,{}^0S_W\,, \tag{2-36d}$$

$${}^0\mathbf{S}_{HD} = \mathop{\mathrm{A}}_{e=1}^{M}\int_{{}^0S_W^{(e)}} \rho_W g \mathbf{H}_i^{(e)\mathrm{T}}\,{}^0n_i^{(e)}\mathbf{H}_3^{(e)} d\,{}^0S_W\,, \tag{2-36e}$$

$${}^0\mathbf{S}_D = \mathop{\mathrm{A}}_{e=1}^{M}\int_{{}^0S_W^{(e)}} \rho_W \mathbf{H}_i^{(e)\mathrm{T}}\,{}^0n_i^{(e)}\mathbf{P}^{(e)} d\,{}^0S_W\,, \tag{2-36f}$$

$${}^0\mathbf{F}_G = \mathop{\mathrm{A}}_{e=1}^{M}\int_{{}^0S_W^{(e)}} \mathbf{P}^{(e)\mathrm{T}}\left\{\mathop{\mathrm{A}}_{\bar{e}=1}^{M}\int_{S_W^{(\bar{e})}} G(x_i;\xi_i)\,{}^0n_i\mathbf{H}_i^{(\bar{e})} d\,{}^0S_\xi\right\} d\,{}^0S_x\,, \tag{2-36g}$$

$${}^0\mathbf{F}_M = \mathop{\mathrm{A}}_{e=1}^{M}\int_{{}^0S_W^{(e)}} \alpha^{(e)}\mathbf{P}^{(e)\mathrm{T}}\mathbf{P}^{(e)} d\,{}^0S_W\,, \tag{2-36h}$$

$${}^0\mathbf{F}_{Gn} = \mathop{\mathrm{A}}_{e=1}^{M}\int_{{}^0S_W^{(e)}} \mathbf{P}^{(e)\mathrm{T}}\left\{\mathop{\mathrm{A}}_{\bar{e}=1}^{M}\int_{{}^0S_W^{(\bar{e})}} \nabla_\xi G(x_i;\xi_i)\mathbf{P}^{(\bar{e})} d\,{}^0S_\xi\right\} d\,{}^0S_x\,, \tag{2-36i}$$

$${}^t\mathbf{R}_B = \mathop{\mathrm{A}}_{e=1}^{N}\int_{{}^0V_S^{(e)}} \mathbf{H}_i^{(e)\mathrm{T}}\,{}^t\hat{\mathbf{f}}_i^{B(e)} d\,{}^0V_S\,, \tag{2-36j}$$

$$ {}^{t}\mathbf{R}_S = \mathop{\mathrm{A}}_{e=1}^{N} \int_{{}^{\tau}S_S^{(e)}} \mathbf{H}_i^{(e)\mathrm{T}}\, {}^{t}\hat{\mathbf{f}}_i^{S(e)} d\, {}^{0}S_S \,, \tag{2-36k} $$

$$ {}^{t}\mathbf{R}_I = \mathop{\mathrm{A}}_{e=1}^{M} \int_{{}^{0}S_W^{(e)}} \mathbf{P}^{(e)\mathrm{T}} \hat{\phi}^{I} d\, {}^{0}S_W \,, \tag{2-36l} $$

where $G(x_i;\xi_i)$ is Green's function, $\bar{e}$ is the element in which ξ_i is defined, and $\hat{\phi}^I$ is the velocity potential for an incident wave. Note that the hydrostatic analysis should be performed in advance to properly construct the geometric stiffness ${}^{0}\mathrm{S}_{KN}$, which includes the stress solution obtained from the hydrostatic analysis. In Eq. (2-36h), the solid angle $\alpha^{(e)}$ is interpolated in element (e) from its nodal values using the finite element shape functions.

It is computationally efficient to use the mode superposition method [11, 18, 26]. Let us consider the generalized eigenvalue problem

$$ {}^{0}\mathbf{S}_K \boldsymbol{\psi}_i = \lambda_i\, {}^{0}\mathbf{S}_M \boldsymbol{\psi}_i \,, \quad i = 1,2,..., N_a \quad \text{for the floating structure,} \tag{2-37} $$

where $\boldsymbol{\psi}_i$ is the eigenvectors, λ_i is the corresponding eigenvalues (dry modes), and N_a is the number of degrees of freedom (DOFs) for the floating structure model.

The nodal displacement vector of the floating structure is approximated as

$$ \hat{\mathbf{U}} \approx \hat{q}_1 \boldsymbol{\psi}_1 + \hat{q}_2 \boldsymbol{\psi}_2 + \cdots + \hat{q}_{\hat{N}_a} \boldsymbol{\psi}_{\hat{N}_a} = \boldsymbol{\psi}\hat{\mathbf{q}} \,, \quad \hat{N}_a < N_a \,, \tag{2-38} $$

in which $\boldsymbol{\psi}$ is the eigenvector matrix, $\hat{\mathbf{q}}$ is the corresponding generalized coordinate vectors, and $\hat{N}_a$ is the number of eigenvectors for approximation.

Substituting Eq. (2-38) into Eq. (2-35) and pre-multiplying $\boldsymbol{\psi}^{\mathrm{T}}$ to the structural part (first row) of Eq. (2-35), the following reduced equation is obtained:

$$ \begin{bmatrix} -\omega^2 \mathrm{I} + \Lambda + {}^{0}\hat{\mathbf{S}}_{CH} & \hat{j}\omega \boldsymbol{\psi}^{\mathrm{T}}\, {}^{0}\mathrm{S}_D \\ \hat{j}\omega\, {}^{0}\mathrm{F}_G \boldsymbol{\psi} & {}^{0}\mathrm{F}_M - {}^{0}\mathrm{F}_{Gn} \end{bmatrix} \begin{bmatrix} \hat{\mathrm{q}} \\ \hat{\boldsymbol{\Phi}} \end{bmatrix} = \begin{bmatrix} \boldsymbol{\psi}^{\mathrm{T}} ({}^{t}\mathbf{R}_B + {}^{t}\mathbf{R}_S) \\ 4\pi\, {}^{t}\mathrm{R}_I \end{bmatrix}, \tag{2-39} $$

where $I_{ij} = \delta_{ij}$ and $\Lambda_{ij} = \lambda_i \delta_{ij}$ with $i, j = 1,2,..., \hat{N}_a$. Note that ${}^{0}\hat{\mathbf{S}}_{CH}$ in Eq. (2-39) is the complete hydrostatic stiffness in the generalized coordinates (${}^{0}\hat{\mathbf{S}}_{CH} = \boldsymbol{\psi}^{\mathrm{T}}\, {}^{0}\mathbf{S}_{CH} \boldsymbol{\psi}$). Rigid body hydrodynamic analysis can be conducted only when the 6 rigid body modes of the floating structure are contained in Eq. (2-39).

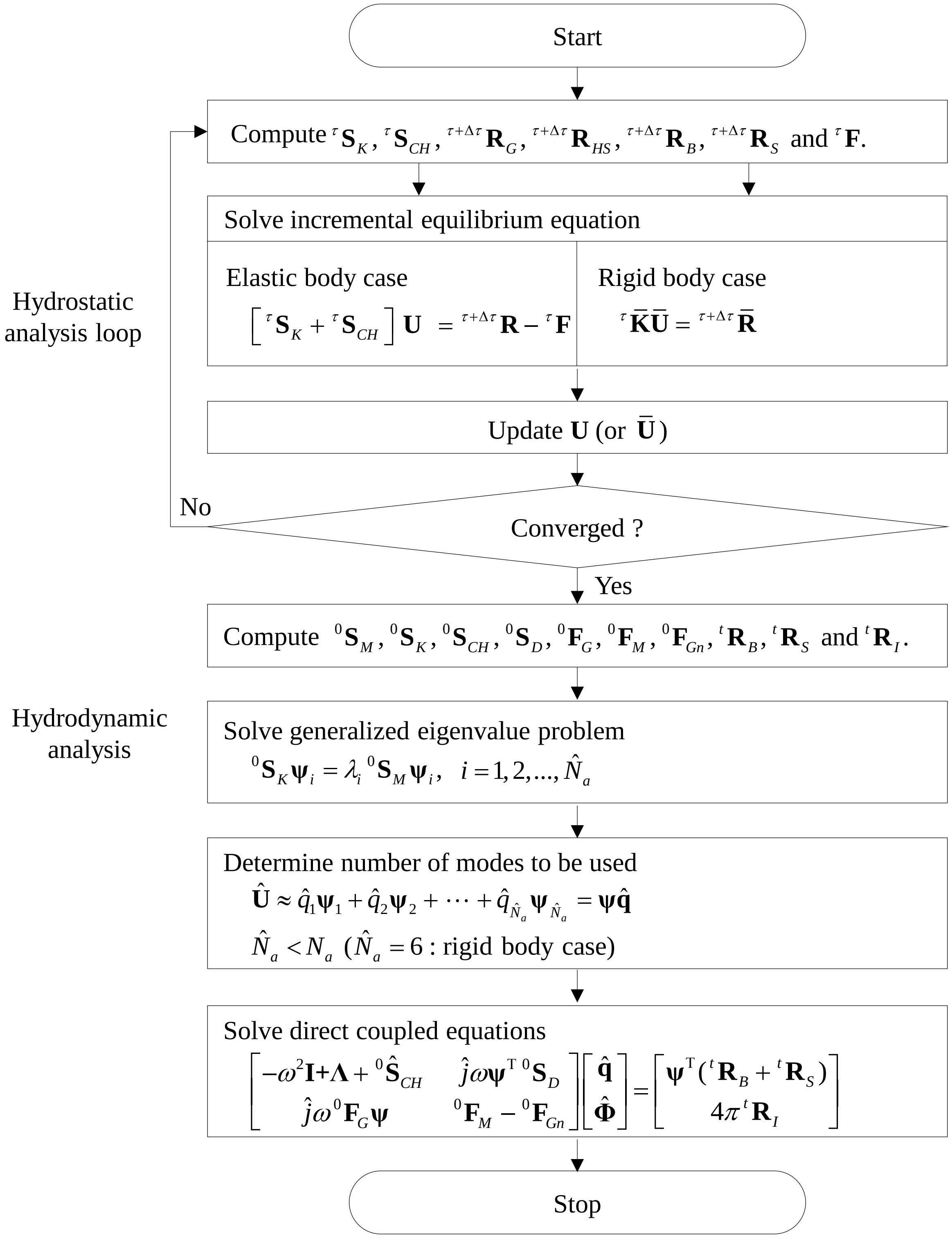

Fig. 2-6. Integrated hydrostatic and hydrodynamic analysis procedure.

Fig. 2-6 shows the procedure for the integrated hydrostatic and hydrodynamic analysis of floating structures, see Ref. [11]. The integrated analysis consists of two steps: hydrostatic analysis to find the static equilibrium state and hydrodynamic analysis to find the dynamic equilibrium state. Of course, the hydrostatic equilibrium state is the reference configuration for the hydrodynamic analysis.

2.3. Non-matching mesh treatment

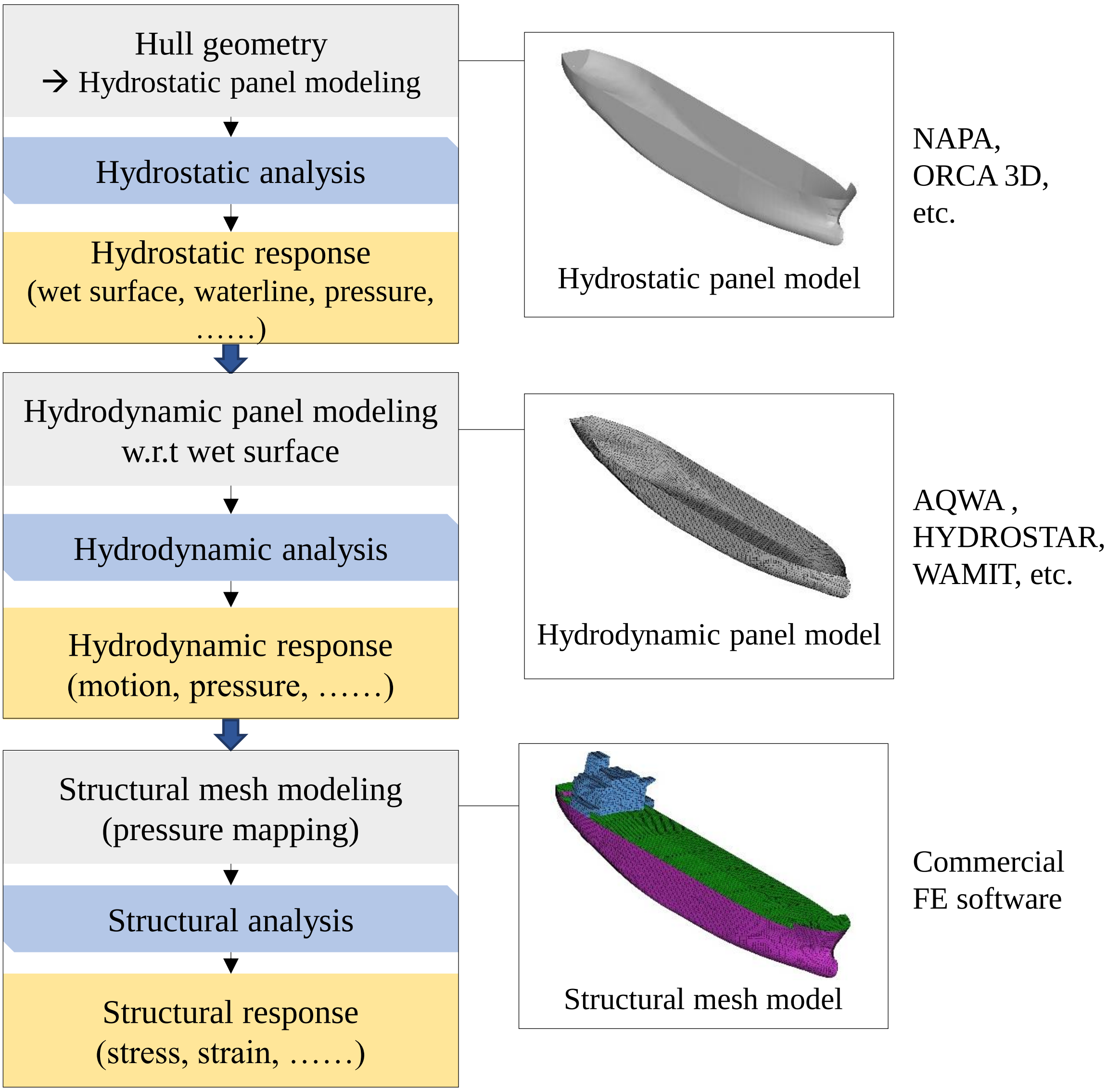

Fig. 2-7. Hydrostatic and hydrodynamic analysis procedure and models required for conventional rigid body hydrodynamic analysis.

The procedure of the conventional rigid body hydrodynamic analysis is shown in Fig. 2-7. Through hydrostatic analysis, waterline and wet surface in the hydrostatic equilibrium state are found. Commercial software such as NAPA and ORCA 3D has been widely used for rigid body hydrostatic analysis [29,30]. The rigid body hydrodynamic analysis is performed using a panel model, modeling only the wet surface. AQWA, HYDROSTAR and WAMIT are popular commercial software for rigid body hydrodynamic analysis [31-33]. For this conventional procedure, two different panel models (hydrostatic and hydrodynamic panel models) are required for both analyses. When a subsequent structural analysis is necessary, a structural FE mesh model is additionally required with hydrostatic and hydrodynamic pressure mapped into the model.

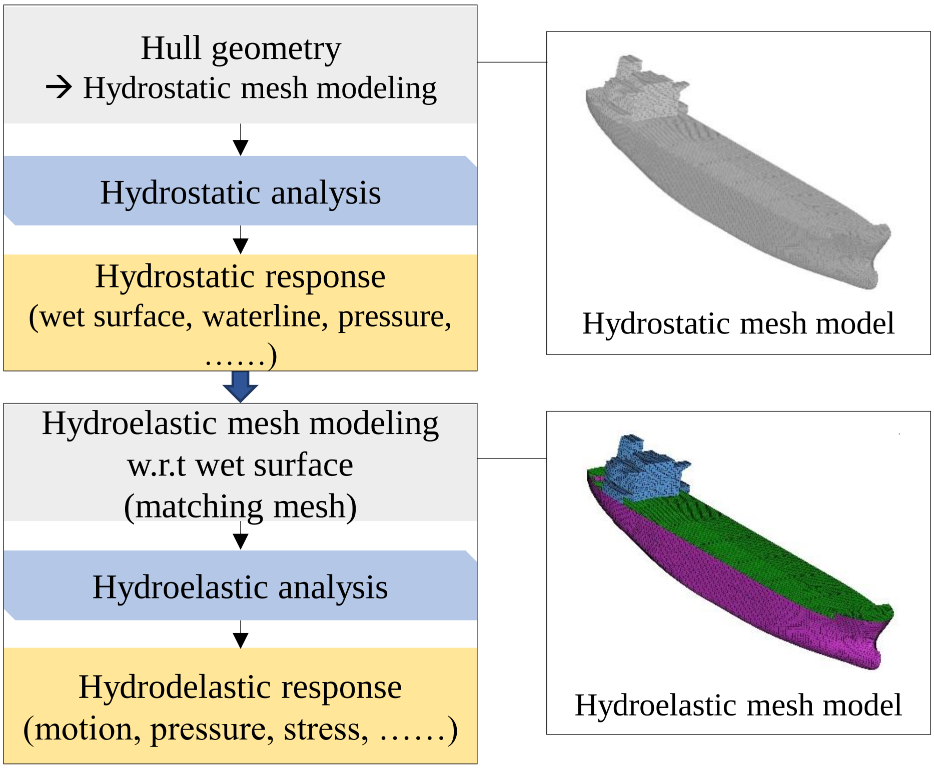

(a)

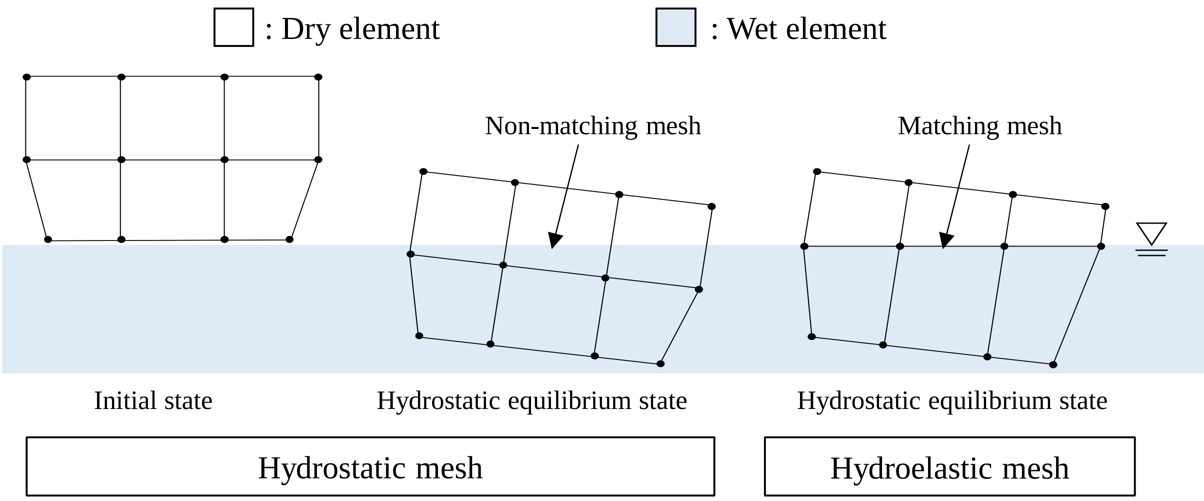

(b)

Fig. 2-8. Hydrostatic and hydrodynamic analysis procedure and mesh models required for hydroelastic analysis: (a) analysis procedure and (b) mesh models.

In the hydroelastic analysis procedure shown in Fig. 2-8(a), a hydrostatic mesh model is necessary for hydrostatic analysis and a hydroelastic mesh model is necessary for hydroelastic analysis. In hydrostatic analysis, the structural flexibility needs to be considered as in Ref. [15]. Both hydrostatic and hydroelastic mesh models are obtained from the structural FE mesh model, with some modification and remeshing. Fig. 2-8(b) shows the remeshing required to prepare the hydroelastic mesh model, in which remeshing is performed along the waterline so that the mesh matches the waterline. In general, FE mesh models also have meshes for inner structures, and thus the inner meshes need to be modified according to the outer hull mesh fitted to the wet surface. It is not an easy task.

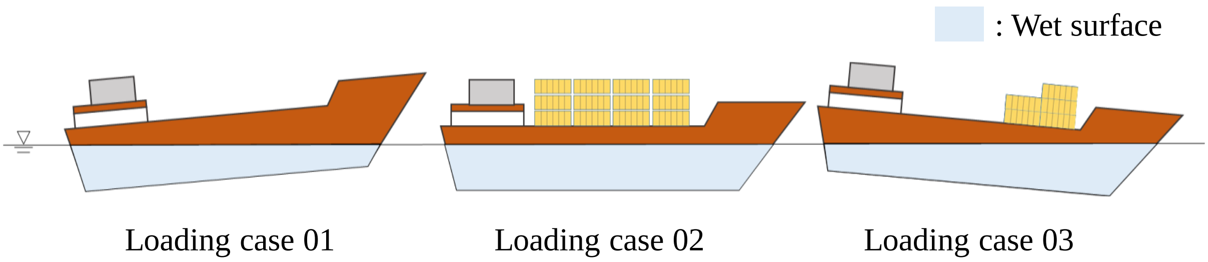

Fig. 2-9. Wet surface change according to static loading cases.

Mesh modeling and remeshing are time-consuming and labor-intensive tasks, depending on engineer's skill level, know-how, and individual abilities. In addition, when hydrodynamic analysis needs to be performed for multiple static loading cases, mesh modeling and remeshing should be performed as many times as the number of static loading cases; see Fig. 2-9.

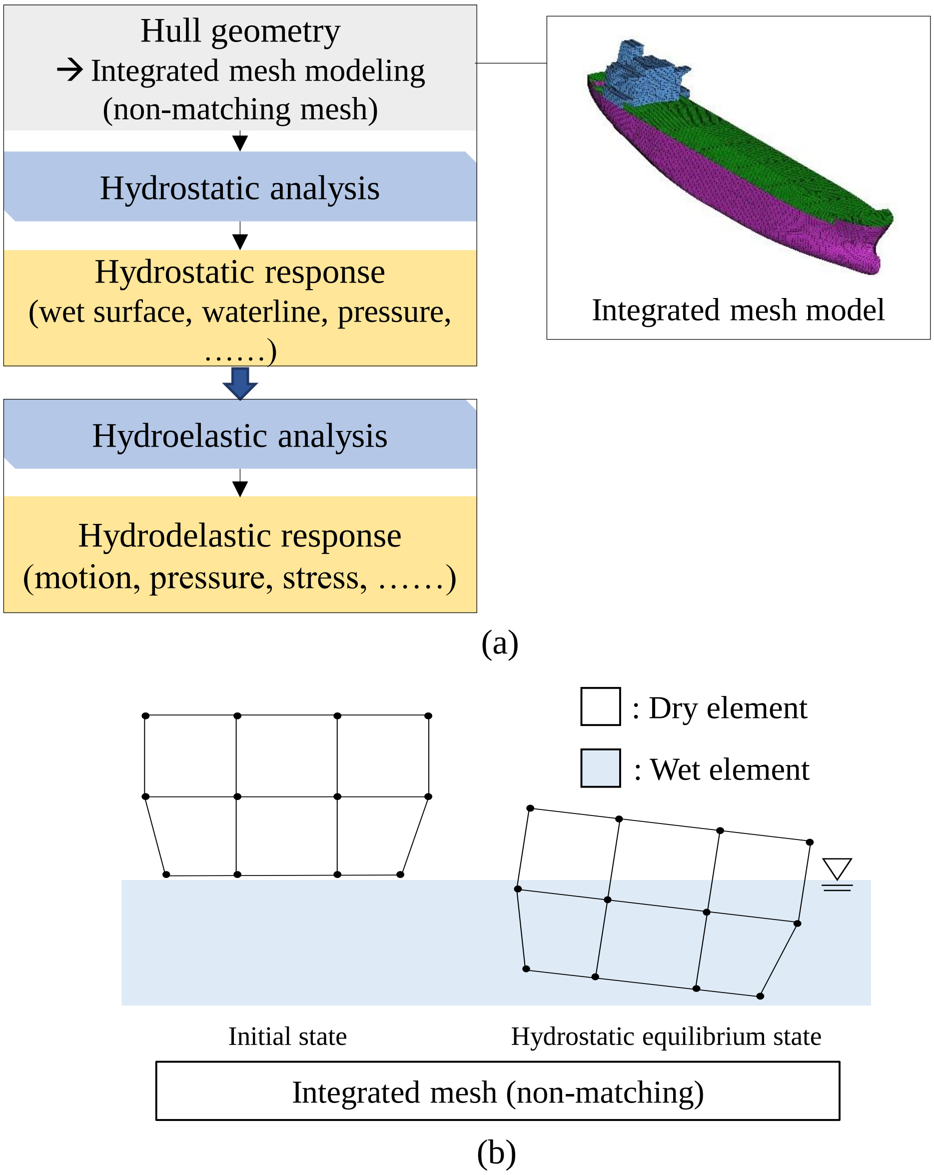

Fig. 2-10. Integrated hydrostatic and hydrodynamic analysis procedure for a flexible structure using a single integrated mesh model: (a) analysis procedure and (b) integrated mesh model.

Fig. 2-10 shows the integrated hydrostatic and hydrodynamic analysis procedure proposed in this study. In the analysis procedure, a single integrated mesh model is used for both analyses without remeshing. Doing so, non-matching mesh treatment is necessary. Since the mesh is not matched with the free-surface, as shown in Fig. 2-10(b), the numerical integration should be carefully performed in calculations of ${}^{\tau}\mathrm{S}_{HN}$, ${}^{\tau}\mathrm{S}_{HD}$ and ${}^{\tau+\Delta\tau}\mathrm{R}_{HS}$ in Eq.(2-30), and ${}^{0}\mathrm{S}_{HN}$, ${}^{0}\mathrm{S}_{HD}$, ${}^{0}\mathrm{S}_{D}$, ${}^{0}\mathrm{F}_{G}$, ${}^{0}\mathrm{F}_{M}$, ${}^{0}\mathrm{F}_{Gn}$, and ${}^{t}\mathbf{R}_{I}$ in Eq. (2-35) over the wet surface parts of the partially wet elements.

We present a special numerical integration technique adopted to effectively resolve the non-matching mesh problem in the integrated hydrostatic and hydrodynamic analysis of flexible floating structures [15]. In particular, the integration technique is applied to the surface integration of the partially submerged finite elements and boundary elements as shown in Fig. 2-11. We here consider 3-node and 4-node elements.

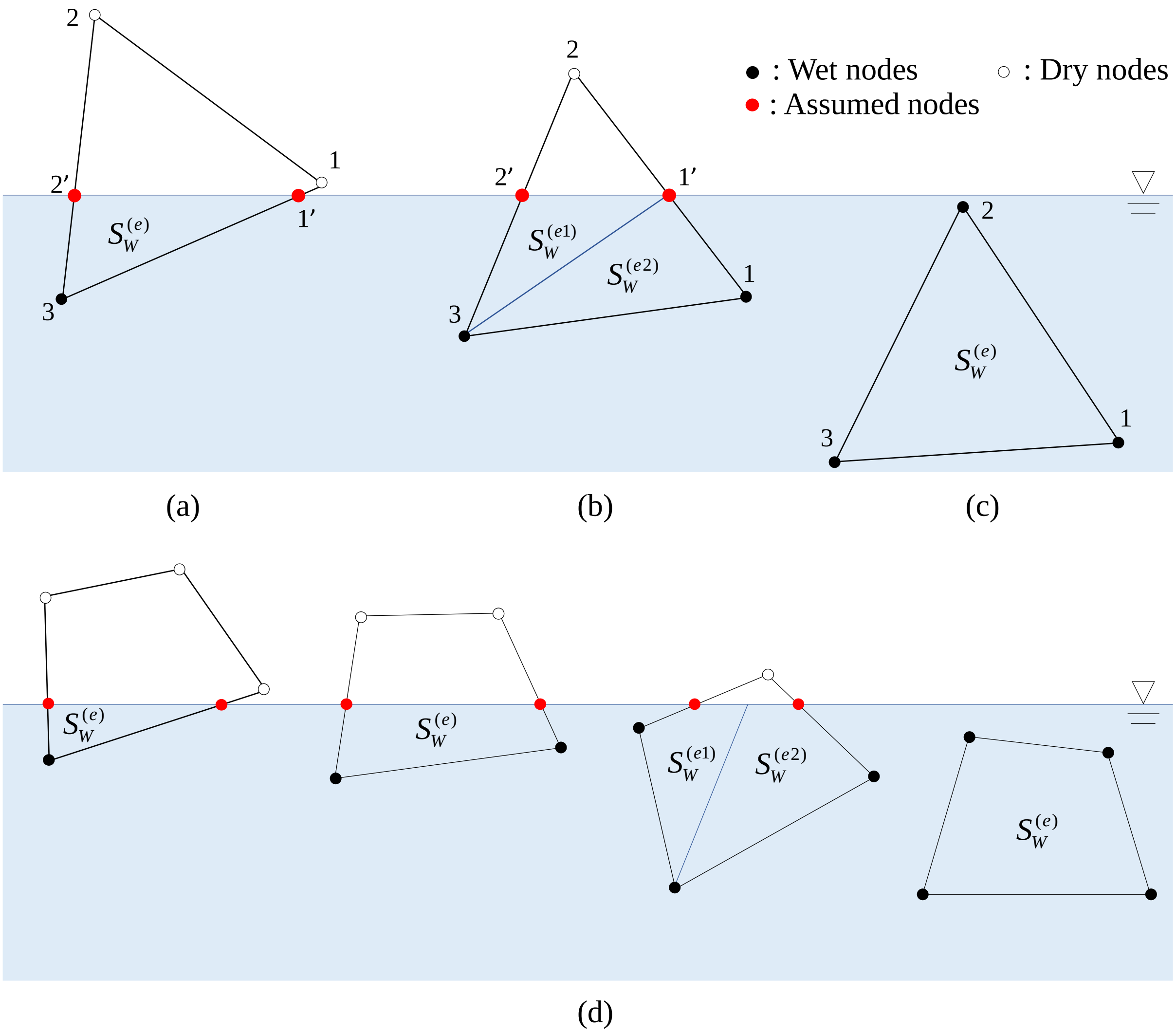

Fig. 2-11. 3-node and 4-node wet element classification for numerical integration.

Fig. 2-11 shows all cases in which 3-node and 4-node elements are in contact with water: 3 cases for the 3-node element and 4 cases for the 4-node element. A node located below the free surface is called a wet node and at least one of the element nodes is wet. For the 3-node element, the following procedure is employed for numerical integrations in the wet surface part of the element.

- Fig. 2-11(a) shows the case in which the element is partially wet and one node is wet. The connectivity of the wet surface part is defined as 1'-2'-3 by introducing the assumed nodes 1' and 2' at the free surface. The assumed nodes 1' and 2' are not real nodes but used only for numerical integration and thus there is no increase in DOFs in the integrated hydrostatic and hydrodynamic analysis. Using the element connectivity, the numerical integration is performed over the wet surface $S_W^{(e)}$ through the conventional three-point Gaussian quadrature.
- Fig. 2-11(b) shows a partially wet element with 2 wet nodes. The wet surface part of the element is divided into two subtriangles ($S_W^{(e)} = S_W^{(e1)} \cup S_W^{(e2)}$). $S_W^{(e1)}$ and $S_W^{(e2)}$ are defined as 1'-2'-3 and 1'-3-1 with assumed nodes 1' and 2'. Three-point Gaussian quadrature is performed in each subtriangular areas.
- Fig. 2-11(c) presents a fully wet element in which all nodes are wet. The three-point Gaussian quadrature is performed over the wet surface part defined by nodes 1-2-3 ($S_W^{(e)}$).

In the case of 4-node quadrilateral elements, numerical integration is performed considering four different cases according to the number of wet nodes; see Fig. 2-11(d). When only one node is wet, the integration over the triangular area is performed as shown in Fig. 2-11(d). The wet surface parts can be divided into triangular and/or quadrilateral shapes for convenience of the numerical integration; see Ref. [15] for details.

Using the special numerical integration technique explained in this section, the numerical integrations in Eqs. (2-30) and (2-35) are effectively performed without modification of the initial element mesh prepared for the hydrostatic analysis. That is, a remeshing process is not required regardless of waterline change due to static loadings.

2.4. Numerical examples

In this section, the validity and effectiveness of the integrated hydrostatic and hydrodynamic analysis is demonstrated through various problems. In the proposed numerical procedure, the structures are modeled by the well-known MITC3 and MITC4 shell finite elements [26,34-39]. To interpolate fluid velocity potential, 3- and 4-node boundary elements are used.

Two hydrodynamic problems are solved: a floating hull [11] and a whole ship. The rigid body hydrodynamic analysis is performed using AQWA, a 3D panel frequency domain code in ANSYS [31], and the results are compared with those of the proposed method.

The density of the fluid (water) ρ_w is 1,000 kg/m^3 and the water depth h is assumed to be infinite. The gravitational acceleration g is 9.8 m/s^2.

2.4.1. Floating hull problem

We here perform both rigid body hydrodynamic and hydroelastic analyses of a floating hull subjected to an incident wave [11]. Hull length is 100 m at the top and 90 m at the bottom; the breadth is 10 m, and height is 4 m, as shown in Fig. 2-12(a). The thickness is 0.03 m, and the density is 6.3585×10^4 kg/m^3 at the bottom area and 5.0×10^3 kg/m^3 at the other areas, which results in a draft of 2 m in the hydrostatic equilibrium state for the rigid body case. Young's modulus $E = 200$ GPa and Poisson's ratio ν =0.3 are used for hydroelastic analysis. We consider two incident wave directions (θ) of 0 and 45 degrees and with periods of 3 s to 12 s.

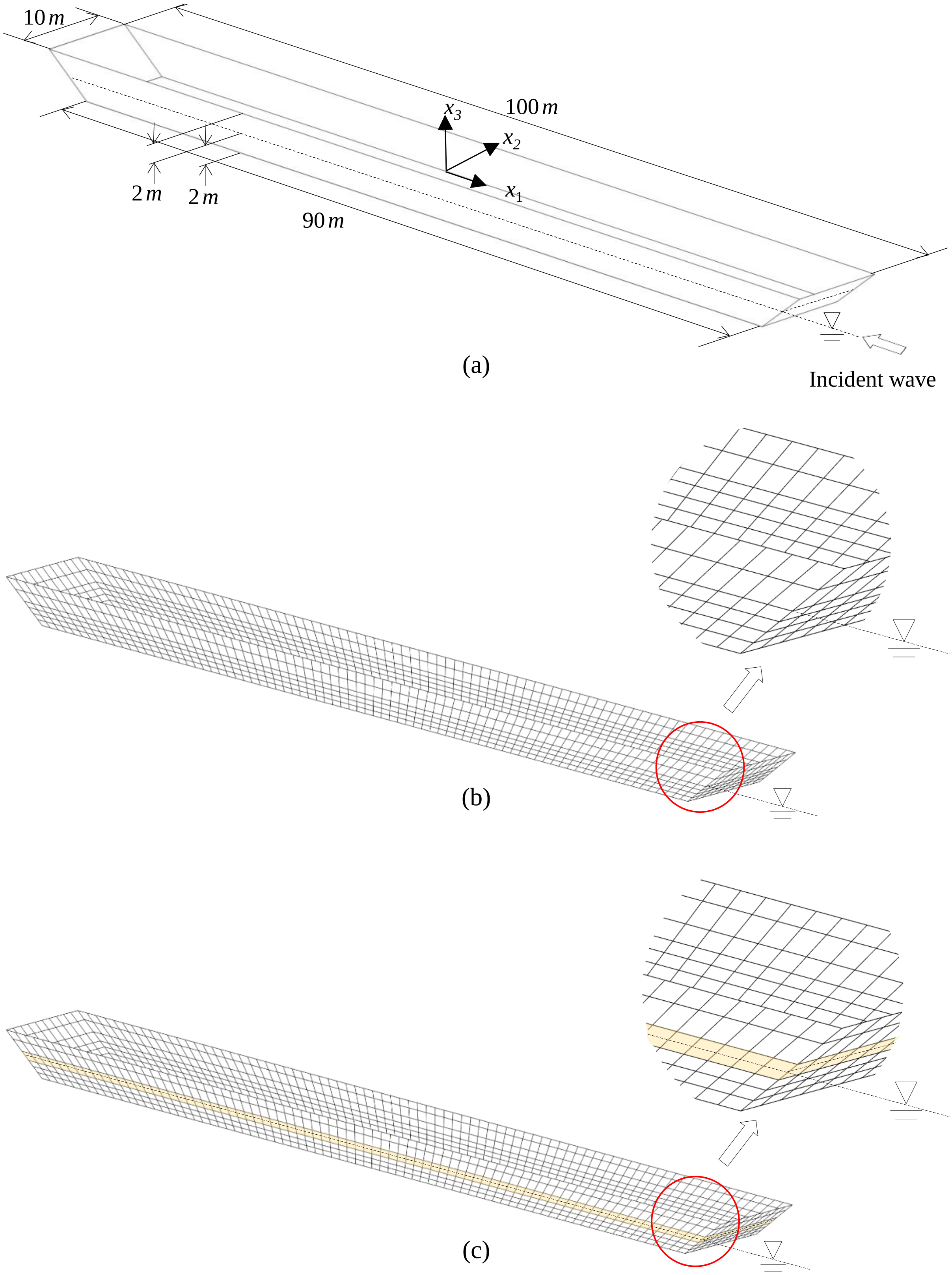

Fig. 2-12. Floating hull problem: (a) problem description, (b) hydroelastic mesh model (matching mesh), and (c) integrated mesh model (non-matching mesh).

The numbers of shell finite elements used are 80, 10 and 6 in the length, breadth, and height directions, respectively. Initially, the integrated mesh model is positioned to have a draft of 2 m for the hydrostatic analysis. After 5 iterations, the buoyancy is balanced with the self-weight within the energy criterion of 1.0×10^{-6}. For hydrodynamic analysis, two meshes are considered: the hydroelastic mesh model used in Fig. 2-12(b) as in Ref. [11] and the integrated mesh model in Fig. 2-12(c). Note that the integrated mesh model has a non-matching mesh, while the hydroelastic mesh model has a matching mesh.

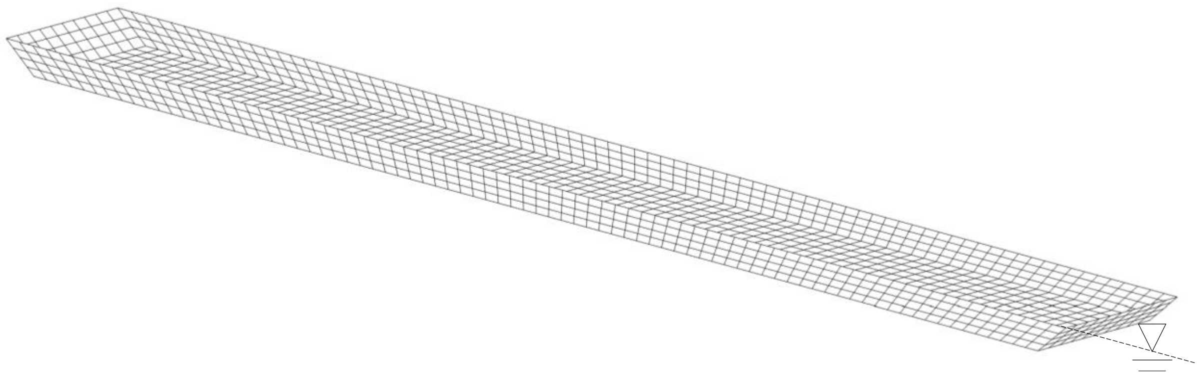

Fig. 2-13. Hydrodynamic panel model of floating hull for AQWA

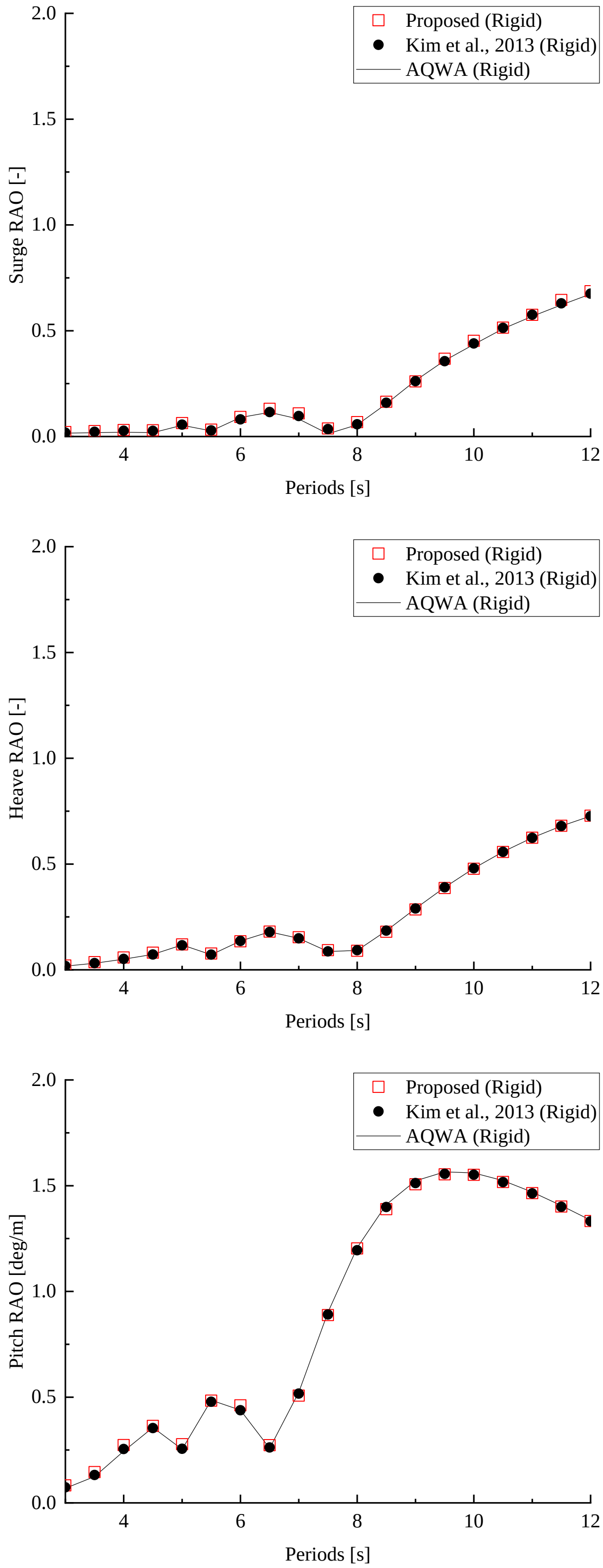

Fig. 2-14. Response amplitude operators (RAOs) for surge, heave, and pitch motions of floating hull when $\theta = 0°$. Rigid body hydrodynamic analysis is performed.

We perform integrated hydrostatic and rigid body hydrodynamic analysis using the integrated mesh model. The results are compared with thos1e obtained using AQWA and reported in Ref. [11]. For the rigid body hydrodynamic analysis of AQWA, the numbers of panels used for modeling only the wet surface of the floating hull are 80, 10, and 4 in the length, breadth, and height directions, respectively, as shown in Fig. 2-13. The analysis in Ref. [11] employed the matching mesh in Fig. 2-12(b). Fig. 2-14 shows the calculated response amplitude operators (RAOs). All the results are in good agreement.

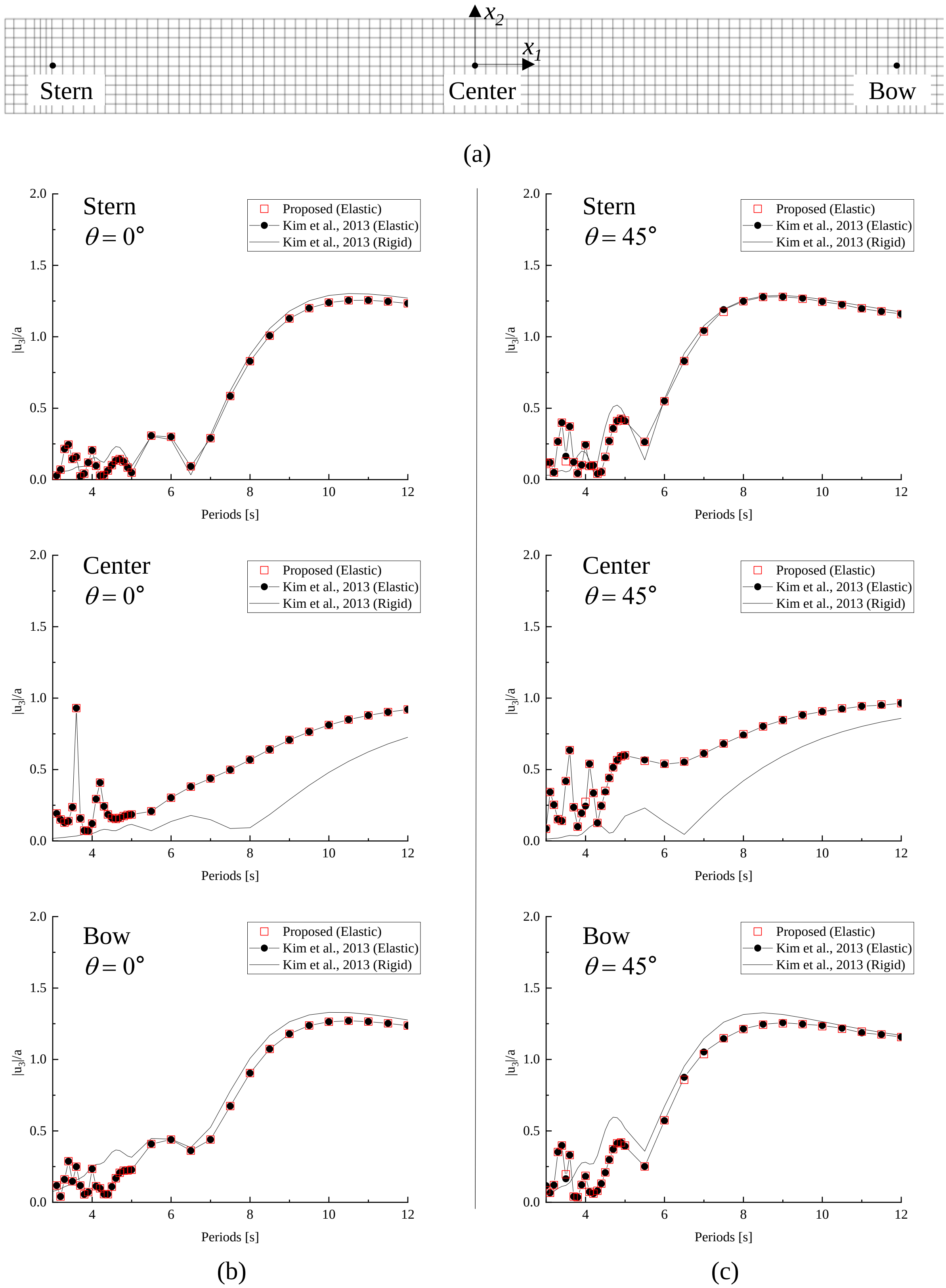

Fig. 2-15. Vertical displacements at stern, center, and bow of floating hull bottom: (a) measuring points, (b) when $\theta = 0°$, and (c) when $\theta = 45°$.

In the hydroelastic analysis, we consider the dry modes of floating structures that correspond to the natural frequencies below $\sqrt{1000}$ rad/s. Fig. 2-15 represents the calculated vertical displacements at stern, center, and bow; the results match well with those in Ref. [11]. Also, the displacements obtained using the rigid body hydrodynamic analysis are compared.

We here confirm that the proposed method using the integrated mesh model with non-matching mesh provides almost the same accuracy as the hydrodynamic panel model and the hydroelastic mesh model with matching mesh.

2.4.2. Whole ship problem

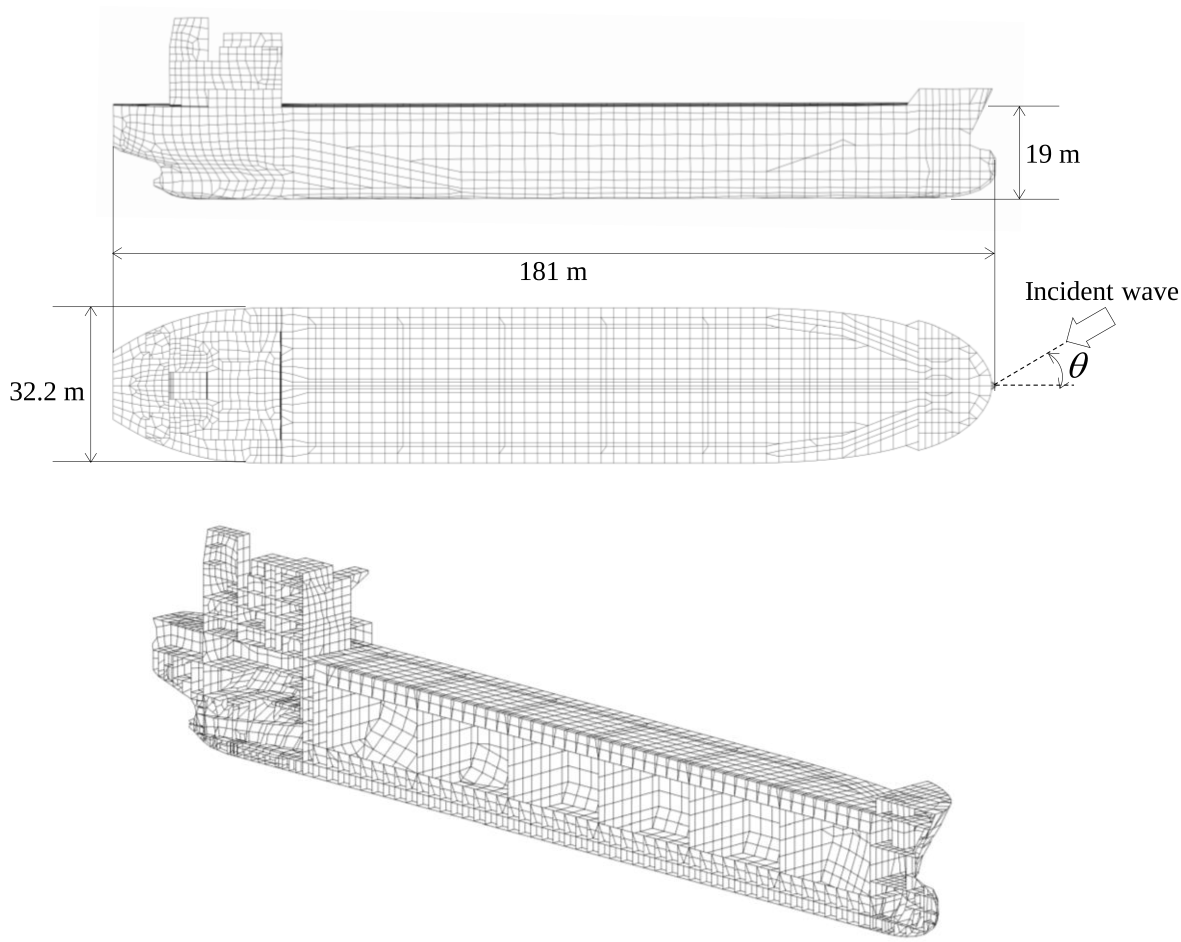

Fig. 2-16. Whole ship FE model.

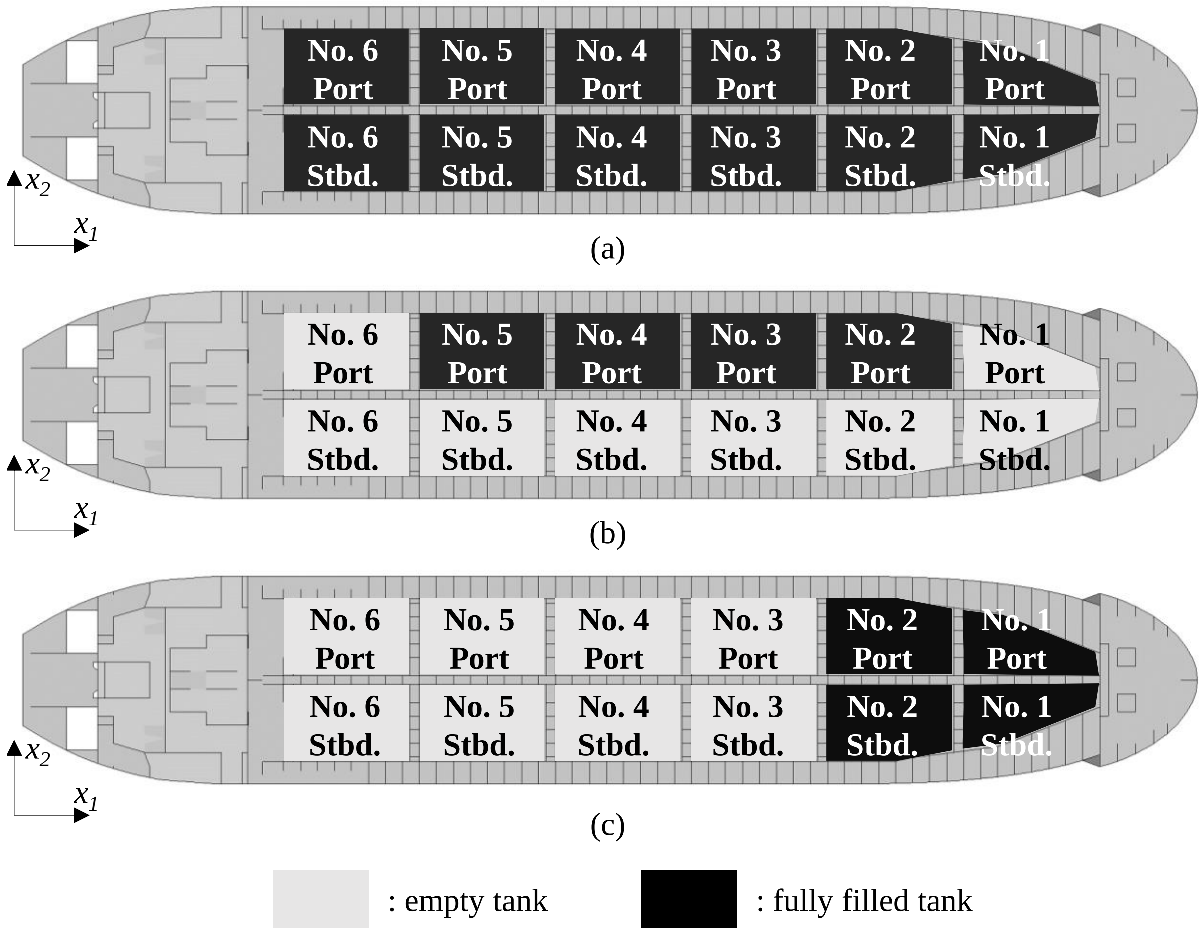

Fig. 2-17. Tank filling conditions: (a) LC01, (b) LC02, and (c) LC03.

We consider a ship with 12 tanks, shown in Fig. 2-16. Length, breadth, and height (bottom to deck) are 181 m, 32.2 m, and 19 m, respectively. The density of the structure is 7,870 kg/m^3, Young's modulus E = 210 GPa, and Poisson's ratio ν = 0.3. The tanker ship is subjected to 3 different static loadings (LC01, LC02, and LC03) depending on whether or not the internal tanks are filled with fluid; see the tank filling conditions in Fig. 2-17. The internal fluid density is 850 kg/m^3. Incident wave angle is 45 degrees and its period ranges from 8.0 to 26.0 s, with a constant increment (ΔT = 1 s).

The whole ship structure is modeled using 17,029 shell finite elements as shown in Fig. 2-16. The internal fluid is modeled by simply increasing the density of the surrounding tank structure. The whole ship model has finite element meshes for inner structures and outer hull, and the meshes are intricately connected. It is a very difficult task to construct a waterline matching mesh model considering such mesh connections. However, the proposed procedure does not require a waterline matching mesh model.

Initially, the integrated mesh model is positioned to have a draft of 13.3 m for the hydrostatic analysis. The buoyancy is balanced with the self-weight within the energy criterion of 1.0×10^{-6}. Table 2-1 shows the hydrostatic equilibrium states calculated for the three static loading cases.

Table 2-1. Hydrostatic analysis results of whole ship model according to three loading cases.

Loading cases		LC01	LC02	LC03
Number of iterations		10	9	9
Displacement [m^3]		52,525	27,025	25,750
Radius of gyration [m]	Roll	12.3	12.2	12.6
	Pitch	40.7	40.9	46.6
	Yaw	41.2	41.0	46.9
COG [m]	x	94.35	91.489	112.03
	y	0.000	2.573	-0.002
	z	-1.400	0.588	2.1915
COB [m]	x	94.35	91.489	112.03
	y	0.000	2.573	-0.002
	z	-5.385	-3.543	-3.518
Trim angle [◦]		0.0	0.0	3.6
Heel angle [◦]		0.0	29.9	0.0

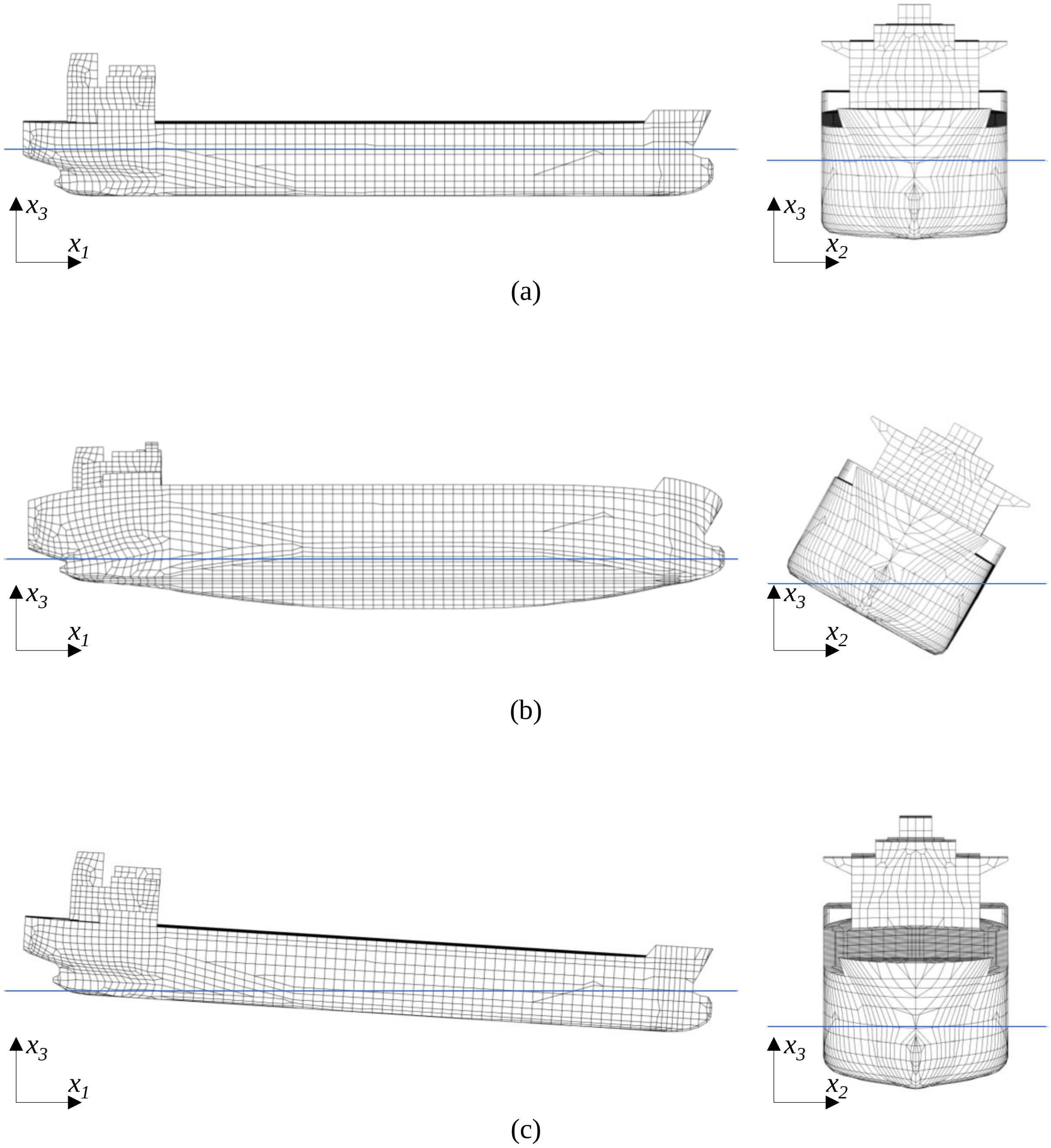

Fig. 2-18. Integrated mesh model in hydrostatic equilibrium states according to loading cases: (a) LC01, (b) LC02, and (c) LC03.

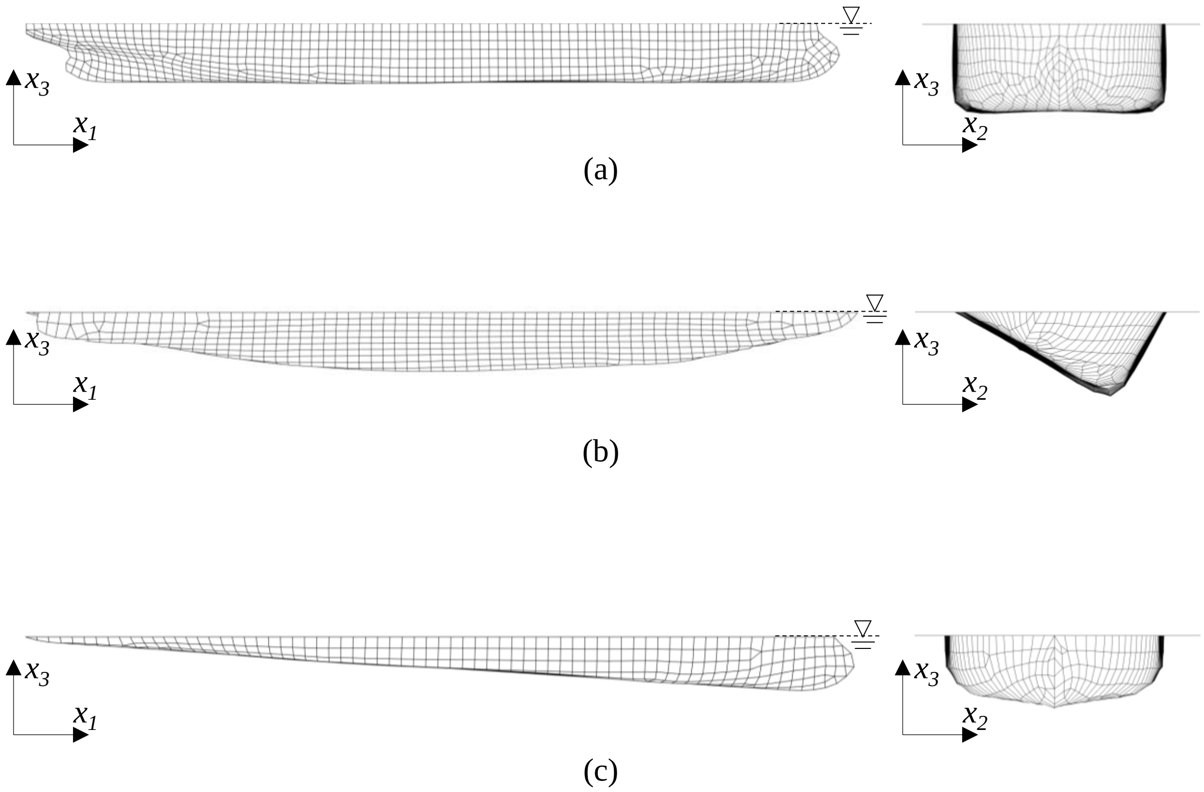

Fig. 2-19. Three different hydrodynamic panel models for AQWA according to loading cases : (a) LC01, (b) LC02, and (c) LC03.

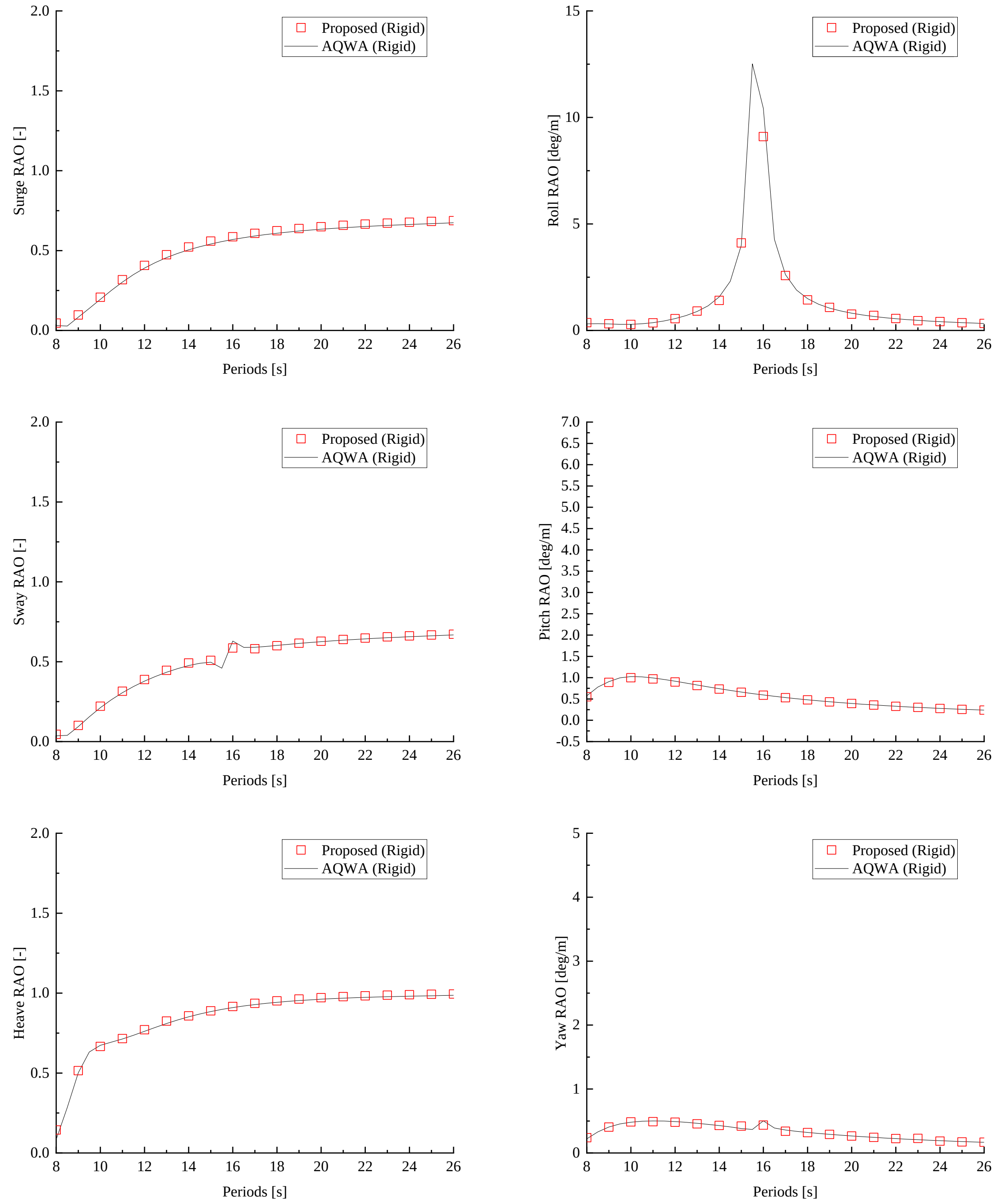

Fig. 2-20. Response amplitude operators (RAOs) for surge, sway, heave, roll, pitch and yaw motions of hull ship for LC01 when $\theta = 45°$. Rigid body hydrodynamic analysis is performed.

Integrated hydrostatic and rigid body hydrodynamic analysis is performed using the integrated mesh model, as shown in Fig. 2-16. Fig. 2-18 and Table 2-1 show the hydrostatic equilibrium states calculated for the three static loading cases. Unlike the proposed method, AQWA requires three different hydrodynamic panel models corresponding to the three static loading cases, as shown in Fig. 2-19. Fig. 2-20 presents the calculated response amplitude operators (RAOs) for the static loading case LC01 when incident wave angle is 45 degrees. The analysis results obtained using the proposed method are in good agreement with those of AQWA.

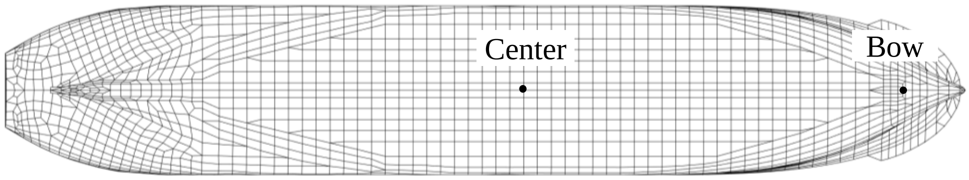

(a)

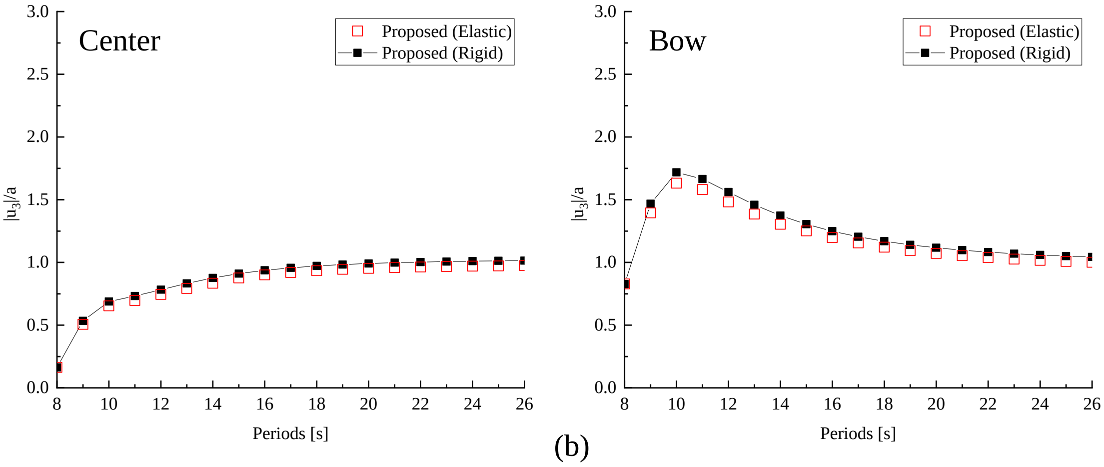

(b)

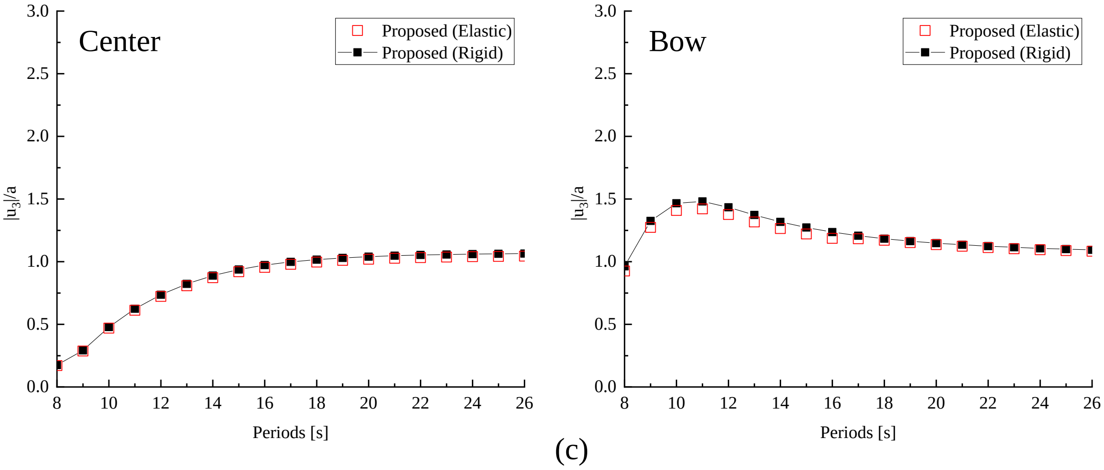

(c)

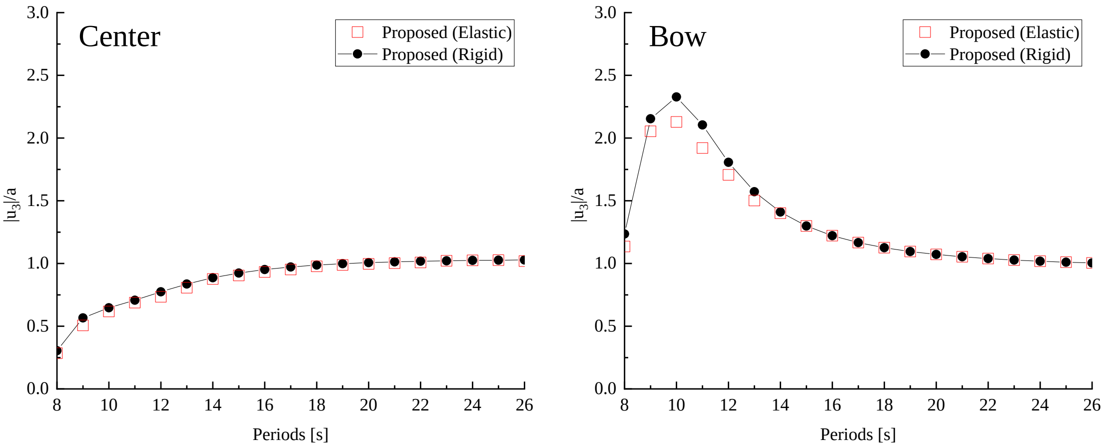

(d)

Fig. 2-21. Vertical displacements of whole ship when $\theta = 45°$: (a) measuring points, (b) LC01, (c) LC02, and (d) LC03.

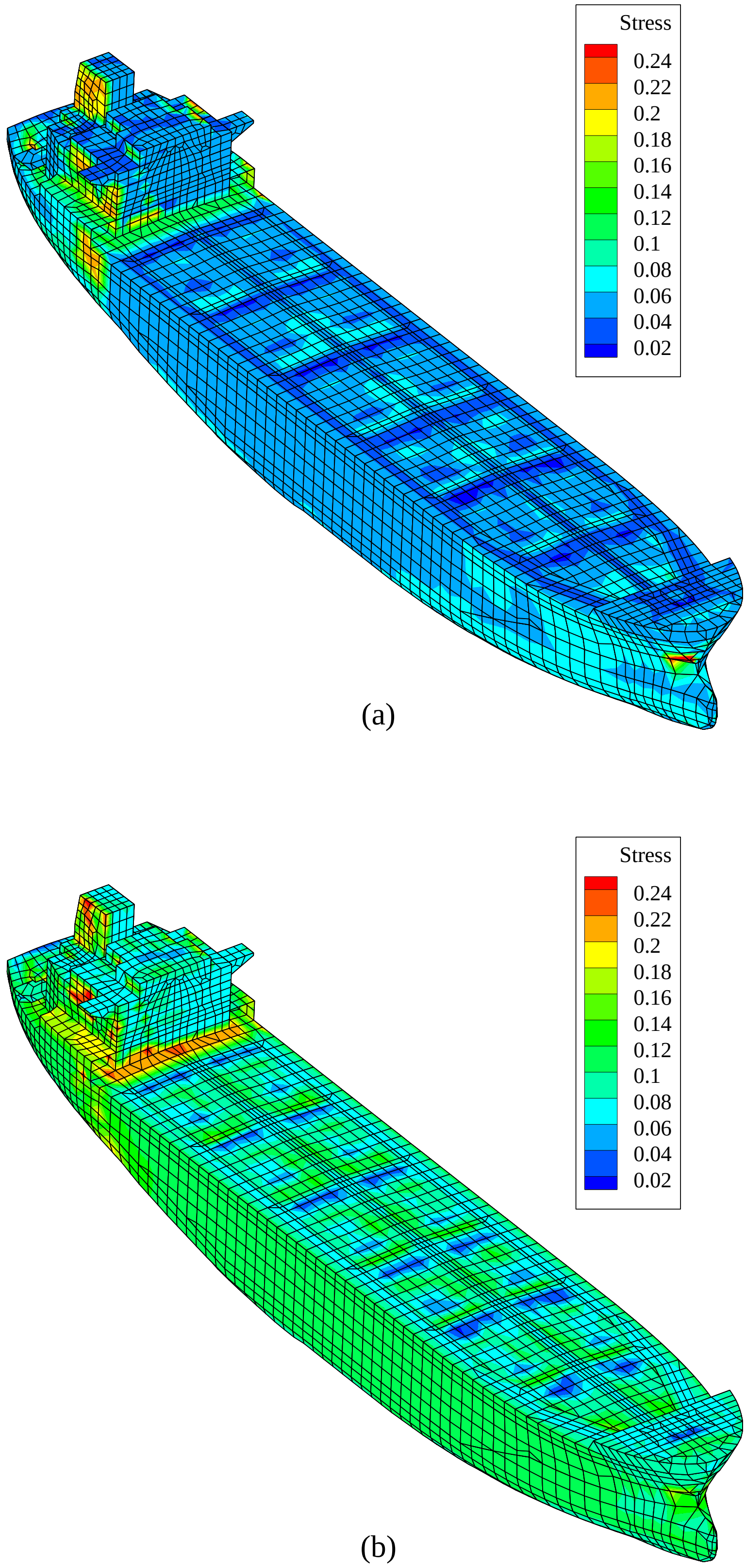

Fig. 2-22. Normalized von-Mises stress distribution for whole ship at LC01 when $T = 11s$: (a) $t = mT$, (b) $t = mT + \frac{T}{4}$ with an integer m.

Integrated hydrostatic and hydroelastic analysis is then carried out. We consider the dry modes of the ship structure that correspond to the natural frequencies below $\sqrt{1000}$ rad/s. Fig. 2-21 presents the calculated vertical displacements at bow and center for three static loading cases (LC01, LC02 and LC03) when incident wave angle is 45 degrees. The results are compared with those of the integrated hydrostatic and rigid body hydrodynamic analysis. In addition, Fig. 2-22 shows the von-Mises stress distribution normalized by the yield stress (355 MPa) for the static loading case LC01 when an incident wave comes with angle 45 degrees, amplitude 1 m, and period 11 seconds.

Table 2-2. Modeling and computation times estimated for hydrostatic and hydrodynamic (hydroelastic) analyses of whole ship model.

ORCA3D/AQWA/ANSYS (Procedure in Fig. 2-7)	Kim et. al., 2013 (Procedure in Fig. 2-8)	Proposed method (Procedure in Fig. 2-10)
Hydrostatic panel modeling: 30 min *	Hydrostatic mesh modeling: 20 min *	Integrated mesh modeling: 20 min *
Hydrostatic analysis 3×3 min	Hydrostatic analysis: 3×15 min	Hydrostatic analysis: 3×15 min
Hydrodynamic panel modeling: 3×30 min *	Hydroelastic mesh modeling: 3×60 min *	
Hydrodynamic analysis: 3×4 min	Hydroelastic analysis: 3×12 min	Hydroelastic analysis: 3×12 min
Structural mesh modeling: 3×60 min*		
Structural FE analysis: 3×2 min		
Total time: 327 min (100 %)	Total time: 281 min (85.9 %)	Total time: 101 min (30.9 %)

* Manual operations are involved.

Finally, we have measured the total modeling and computation times required for hydrostatic and hydrodynamic (hydroelastic) analyses, taking into account three static loading cases. These values are found in Table 2-2. We considered three approaches, as shown in Figs. 7, 8, and 10, and assumed that the CAD and FE models were already available. The time and effort required for manual operations, such as mesh modeling and remeshing, vary depending on the engineer's individual abilities. To estimate the time required for manual operations, we consulted with experienced ship design engineers.

The first approach is a traditional method that sequentially utilizes three commercial codes: ORCA3D for rigid body hydrostatic analysis, AQWA for rigid body hydrodynamic analysis, and ANSYS for structural FE analysis. The second approach follows the procedure used by Kim et. al. for conventional hydroelastic analysis, while the third approach employs the proposed method. Manual operations are inevitable for transferring information between the different models.

The required times consist of modeling and calculation times. Modeling time includes time to create hydrostatic panel/mesh model, hydrodynamic panel/mesh model, and structural mesh model. Remeshing is performed using Altair Hypermesh [40]. Mesh modelings and calculations are performed on a personal computer (PC) with Intel Core i7-8700, 3.20 GHz CPU, and 64 GB RAM. Modeling time to create the hydrodynamic mesh model is not necessary for the proposed method. The proposed method significantly reduces total time required, although the amount of reduction varies depending on engineer's skill level and know-how.

2.5. Concluding remarks

we proposed a method for the hydro-elastic analysis considering various loading conditions, in which the direct-coupling method was employed to couple structural motions and water waves. When the cargo loading conditions of the floating structures change, the wet surface changes according to changing the hydrostatic equilibrium state. The remeshing is inevitable process to perform hydrodynamic analysis for each loading condition. The special numerical integration method was adopted to resolve the non-matching mesh problem without remeshing process. The proposed method was verified through numerical examples. As numerical examples, we solved the problems of simple barge and whole ship model with an incident wave and the radiation problem of floating hull. The numerical results are verified the high fidelity of the present formulation when compared with the experimental results and the numerical results of existing commercial codes based on the conventional formulation.

Chapter 3. Direct calculation of the stress transfer function in frequency domain

We present the Direct calculation of the stress transfer function in frequency domain in this chapter. The stress response for hydroelastic analysis in frequency domain in Section 3.1. In Section 3.2, an effective stress RAOs calculation methods are introduced. In Section 2.3, the feasibility of the proposed numerical procedure is demonstrated through various problems. Finally, the concluding remarks are given.

3.1. Stress response for hydroelastic analysis in frequency domain

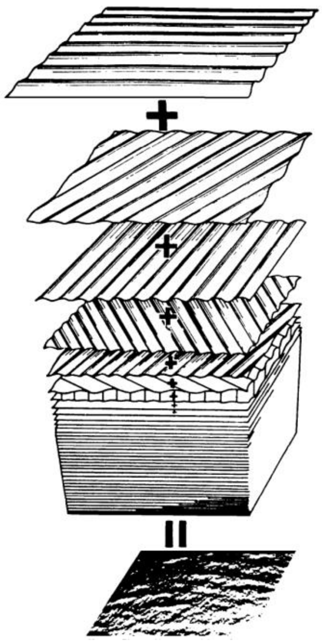

Fig. 3-1. A sum of many simple sine waves makes an irregular Sea

Irregular waves can be represented as a linear superposition of regular waves, as shown in Fig.3-1. A method for analyzing the response by introducing sinusoidal waves with unit amplitude into a motion analysis model is used. This allows for the mathematical estimation of the response and loads in irregular sea states[41].

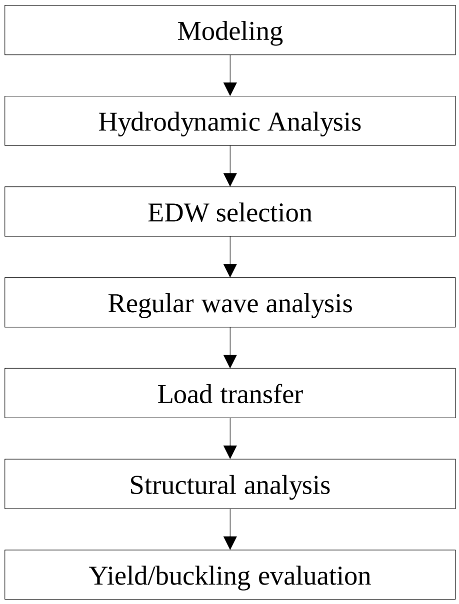

(a)

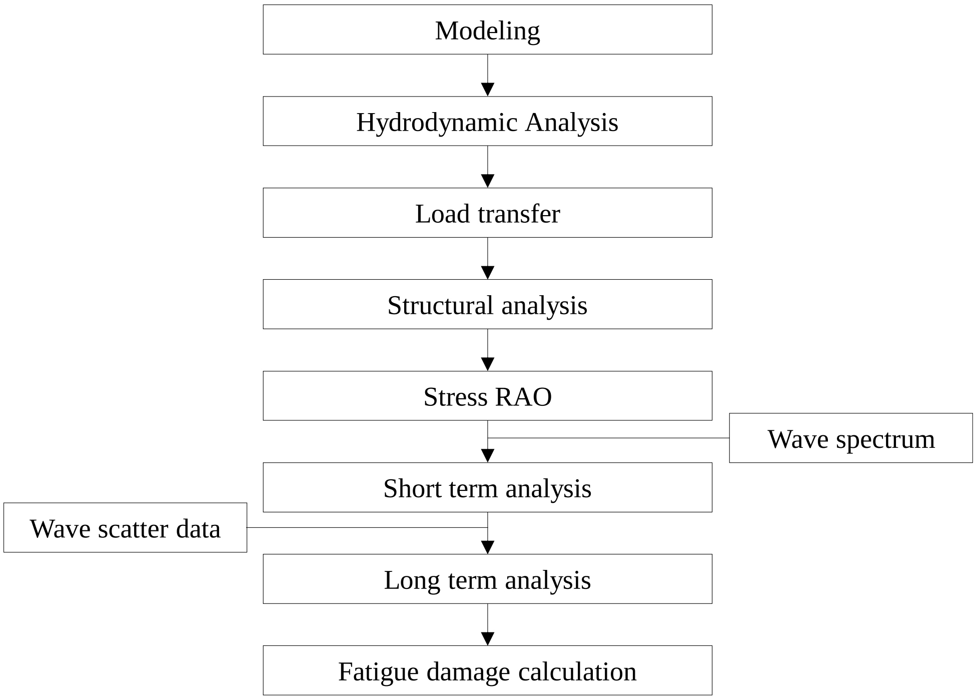

(b)

Fig. 3-2 The evaluation procedures for ship structural strength[44]:
(a) yield/buckling strength, (b) fatigue Strength.

By inputting sinusoidal waves with unit amplitude into the motion analysis model, the response amplitude operator (RAO) is obtained. Mathematical extension of the response to short-term and long-term responses using statistical data for irregular sea states allows for the calculation of response and loads in irregular sea[55-58]. In other words, RAO for unit amplitude response is fundamental data for the design of ships/offshore structures. The evaluation procedure for yield strength and fatigue strength of ships is illustrated in Fig. 3-2.

3.1.1. Hydroelastic(hydrodynamic) equation

In the steady state, the direct-coupled equations are used for this study. The following direct-coupled equations are finally obtained, the detailed procedures in Ref. [11-14,18]

Invoking a harmonic response for angular frequency ω ($u_i = \mathrm{Re}\{\hat{u}_i({}^0x_i)e^{\hat{j}\omega t}\}$; $\hat{j}=\sqrt{-1}$), we then obtain the following steady state equation:

$$
\begin{aligned}
&-\omega^2\int_{{}^0V_S}\rho_S\hat{u}_i\delta u_i d\,{}^0V_S+\int_{{}^0V_S}C_{ijkl}\,{}_0\hat{e}_{kl}\delta\,{}_0e_{ij}d\,{}^0V_S+\int_{{}^0V_S}{}^0\sigma_{ij}\delta\,{}_0\hat{\eta}_{ij}d\,{}^0V_S\\
&-\int_{{}^0S_W}\rho_W\,{}^0x_3\,{}_0\hat{Q}_{ij}\,{}^0n_j\delta u_i d\,{}^0S_W-\int_{{}^0S_W}\rho_W g\hat{u}_3\,{}^0n_i\delta u_i d\,{}^0S_W-\hat{j}\omega\int_{{}^0S_W}\rho_W\hat{\phi}\,{}^0n_i\delta u_i d\,{}^0S_W=\\
&\qquad\int_{{}^0V_S}{}^t\hat{f}_i^B\delta u_i d\,{}^0V_S+\int_{{}^0S_S}{}^t\hat{f}_i^S\delta u_i d\,{}^0S_S\,,
\end{aligned}
\tag{3-1}
$$

with

$$
{}_0e_{ij}=\mathrm{Re}\{{}_0\hat{e}_{ij}({}^0x_i)e^{\hat{j}\omega t}\},\ {}_0Q_{ij}=\mathrm{Re}\{{}_0\hat{Q}_{ij}({}^0x_i)e^{\hat{j}\omega t}\},\ {}^tP_D=\mathrm{Re}\{\hat{P}_D({}^0x_i)e^{\hat{j}\omega t}\},
$$

$$
{}_0\eta_{ij}=\mathrm{Re}\{{}_0\hat{\eta}_{ij}({}^0x_i)e^{\hat{j}\omega t}\},\ {}^t\tilde{f}_i^B=\mathrm{Re}\{\hat{f}_i^B({}^0x_i)e^{\hat{j}\omega t}\},\ {}^t\tilde{f}_i^S=\mathrm{Re}\{\hat{f}_i^S({}^0x_i)e^{\hat{j}\omega t}\}.
$$

$$
\begin{aligned}
&\int_{{}^0S_W}\alpha\hat{\phi}(x_i)\delta\hat{\phi}(x_i)d\,{}^0S_x\\
&-\int_{{}^0S_W}P.V.\int_{{}^0S_W}\left(\frac{\partial G(x_i;\xi_i)}{\partial\,{}^0n(\xi_i)}\hat{\phi}(\xi_i)-\hat{j}\omega G(x_i;\xi_i)\hat{u}_i(\xi_i)\,{}^0n_i(\xi_i)\right)dS_\xi\delta\hat{\phi}(x_i)d\,{}^0S_x=\\
&\qquad 4\pi\int_{{}^0S_W}\hat{\phi}^I(x_i)\delta\hat{\phi}(x_i)d\,{}^0S_x\quad\text{for }x_i\text{ on }{}^0S_W\,.
\end{aligned}
\tag{3-2}
$$

The following discrete coupled equation for the steady state problem can be obtained, detail procedure is well described in [11-14]

$$
\begin{bmatrix}-\omega^2\,{}^0\mathrm{S}_M+{}^0\mathrm{S}_K+{}^0\mathrm{S}_{CH} & \hat{j}\omega\,{}^0\mathrm{S}_D\\ \hat{j}\omega\,{}^0\mathrm{F}_G & {}^0\mathrm{F}_M-{}^0\mathrm{F}_{Gn}\end{bmatrix}\begin{bmatrix}\hat{\mathbf{U}}\\ \hat{\mathbf{\Phi}}\end{bmatrix}=\begin{bmatrix}{}^t\mathbf{R}_B+{}^t\mathbf{R}_S\\ 4\pi\,{}^t\mathrm{R}_I\end{bmatrix}
\tag{3-3}
$$

with ${}^{0}\mathrm{S}_{CH} = {}^{0}\mathrm{S}_{KN} - {}^{0}\mathrm{S}_{HN} - {}^{0}\mathrm{S}_{HD}$,

where $\hat{\mathbf{U}}$ and $\hat{\boldsymbol{\Phi}}$ denote nodal displacement and velocity potential vectors, respectively, for the whole model, ${}^{0}\mathbf{S}_{M}$ is the mass matrix, and ${}^{0}\mathrm{S}_{CH}$ is the complete hydrostatic stiffness matrix including the hydrostatic stiffness terms (${}^{0}\mathrm{S}_{HN}$ and ${}^{0}\mathrm{S}_{HD}$) and the geometric stiffness (${}^{0}\mathrm{S}_{KN}$). Note that the superscript 0 denotes the configuration of the hydrostatic equilibrium state. $\mathbf{U}$ is the incremental nodal displacement vector for the whole model.

The condensed structural equation for the steady state 3D hydroelastic problems:

$$\left[-\omega^{2}\left({}^{0}\mathrm{S}_{M} + {}^{0}\mathrm{S}_{MA}\right) + j\omega {}^{0}\mathrm{S}_{CH} + {}^{0}\mathrm{S}_{K} + {}^{0}\mathrm{S}_{CH}\right]\hat{\mathbf{U}} = \mathbf{R}_{W}, \tag{3-4}$$

where

${}^{0}\mathrm{S}_{MA} = \mathrm{Re}\left\{ {}^{0}\mathrm{S}_{D}\left({}^{0}\mathrm{F}_{M} - {}^{0}\mathrm{F}_{Gn}\right)^{-1} {}^{0}\mathrm{F}_{G} \right\}$: added mass matrix,

${}^{0}\mathrm{S}_{CW} = -\omega \times \mathrm{Im}\left\{ {}^{0}\mathrm{S}_{D}\left({}^{0}\mathrm{F}_{M} - {}^{0}\mathrm{F}_{Gn}\right)^{-1} {}^{0}\mathrm{F}_{G} \right\}$: radiated wave damping matrix,

${}^{0}\mathrm{S}_{W} = j\omega {}^{0}\mathrm{S}_{D}\left({}^{0}\mathrm{F}_{M} - {}^{0}\mathrm{F}_{Gn}\right)^{-1} 4\pi {}^{t}\mathrm{R}_{I}$: wave excitation force matrix.

3.1.2. Stress response

The responses obtained from the motion equation derived from the frequency domain Eq. (3-4) can be expressed in the form of complex numbers or trigonometric functions. When represented in complex number form, it can be expressed as real and imaginary components, or in general trigonometric function form as the following equation, assuming the specific frequency ω .

$$\hat{u}_{i} = \hat{u}_{i}^{\mathrm{Re}} + \hat{j}\hat{u}_{i}^{\mathrm{Im}} \tag{3-5}$$

$$\begin{aligned} u_{i}(t) &= \mathrm{Re}\{\hat{u}_{i}\, e^{\hat{j}\omega t}\} \\ &= \hat{u}_{i}^{\mathrm{Re}}\cos\omega t - \hat{u}_{i}^{\mathrm{Im}}\sin\omega t, \end{aligned} \tag{3-6}$$

in which

$$\hat{u}_{i}\, e^{\hat{j}\omega t} = \hat{u}_{i}\cos\omega t - \hat{j}\hat{u}_{i}\sin\omega t.$$

For the stress analysis,

$$\hat{\sigma}_{ij} = C_{ijrs}\hat{\varepsilon}_{rs}$$

$$= \hat{\sigma}_{ij}^{\mathrm{Re}} + \hat{j}\hat{\sigma}_{ij}^{\mathrm{Im}}, \tag{3-7}$$

where,

$\hat{\sigma}_{ij}^{\mathrm{Re}} = C_{ijrs}\hat{\varepsilon}_{rs}^{\mathrm{Re}}, \hat{\sigma}_{ij}^{\mathrm{Im}} = C_{ijrs}\hat{\varepsilon}_{rs}^{\mathrm{Im}}$.

In the frequency domain, the components of stress, similar to displacement, are also expressed in the form of harmonic response.

$$\sigma_{ij}(t) = \hat{\sigma}_{ij}^{\mathrm{Re}} \cos \omega t - \hat{\sigma}_{ij}^{\mathrm{Im}} \sin \omega t \tag{3-8}$$

In order to evaluate the yield and fatigue strength of a structure, a combined stress is used. Representative combined stresses include von-Mises stress and principal stress. The von-Mises stress is a representative stress for evaluating the yield stress, and is a stress using the second-order deviation stress invariant. The equation for obtaining the von-Mises stress in the time domain is as follows, and the coefficient terms are organized by the following equations

$$\sigma_{vM}(t) = \sqrt{\frac{3}{2}\left(\sigma_{ij}(t) - \frac{1}{3}\delta_{ij}\sigma_{kk}(t)\right)^2}\,. \tag{3-9}$$

The concept of principal stress is commonly used in engineering and mechanics to analyze the failure or deformation behavior of materials and structures, such as in structural engineering, geotechnical engineering, and solid mechanics. Understanding the principal stresses and their directions is crucial in predicting how materials and structures will behave under different loading conditions and designing safe and efficient engineering systems. Because crack growth is closely related to the angle of principal stress, principal stress is often used for fatigue analysis. Stress consists of normal stress and shear stress, and both stresses change according to the angle of the slope. At this time, there is an inclined plane where the shear stress is zero and the normal stress is maximum, and this is called the principal stress plane, and the maximum normal stress is called the principal stress. The principal stress in a three-dimensional stress state can be defined by the stress invariants (I_1, I_2, I_3) as follows.

$$P_1 = \frac{I_1(t)}{3} + \frac{2}{3}\left(\sqrt{I_1^2(t) - 3I_2(t)}\right)\cos\phi,$$

$$P_2 = \frac{I_1(t)}{3} + \frac{2}{3}\left(\sqrt{I_1^2(t) - 3I_2}(t)\right)\cos\left(\phi(t) - \frac{2\pi}{3}\right),$$

$$P_3(t) = \frac{I_1(t)}{3} + \frac{2}{3}\left(\sqrt{I_1^2(t) - 3I_2}(t)\right)\cos\left(\phi(t) - \frac{4\pi}{3}\right), \tag{3-10}$$

where,

$$I_1(t) = \sigma_{ii}(t),$$

$$I_2(t) = \frac{1}{2}\left\{\sigma_{ii}(t)\sigma_{jj}(t) - \sigma_{ij}(t)\sigma_{ji}(t)\right\},$$

$$I_3(t) = \varepsilon_{ijk}\sigma_{1i}(t)\sigma_{2j}(t)\sigma_{3k}(t),$$

$$\phi = \frac{1}{3}\cos^{-1}\left(\frac{2I_1^3 - 9I_1I_2 + 27I_3}{2(I_1^2 - 3I_2)^{3/2}}\right).$$

3.2. The proposed method for stress RAO

In this study, we propose the method to calculate the transfer function using the corresponding period and maximum value in order to directly compute the stress RAO. We describe the methods for evaluating the strength of ships and offshore structures using two types of stress that are commonly used in the field of structural analysis of ships and offshore structures. Since most ships and floating structures are thin shell structures with thin thickness compared to their length, we assume a plane stress state for the analysis.

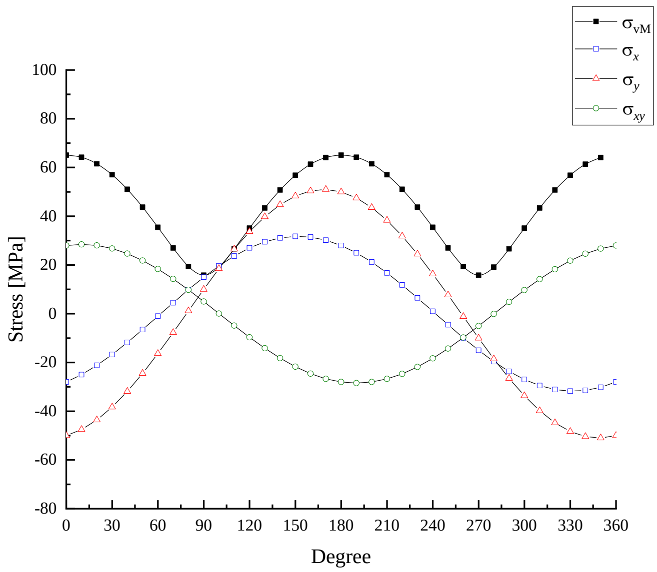

Fig. 3-3. The von-Mises stress results obtained from conventional method.

Fig. 3-3 shows the conventional method shows a conventional method for obtaining the stress RAO. The following is the method commonly used in practical design to determine the maximum value of stress [42]. For the derived non-harmonic von Mises and principal stresses the following values are relevant for presentation:

• The stress at a given value of the phase (t) of the incoming wave.

• The maximum stress found by stepping through the whole cycle ($0 \le t \le T$).

• The value of the phase of the incoming wave giving the maximum stress.

3.2.1. von-Mises stress

The stress components expressed as Eq. (3-8) can be substituted into the von-Mises stress Eq. (3-9), and rearranged using trigonometric identities for plane triangles, yielding the following expression:

$$\sigma_{vM}(t) = \sqrt{\frac{\sqrt{(A-B)^2 + C^2}}{2}\sin(2\omega t + \phi_1) + \frac{A+B}{2}}\,, \tag{3-11}$$

where

$$A = \frac{3}{2}\left(\hat{\sigma}_{ij}^{\mathrm{Re}} - \frac{1}{3}\delta_{ij}\hat{\sigma}_{kk}^{\mathrm{Re}}\right)\left(\hat{\sigma}_{ij}^{\mathrm{Re}} - \frac{1}{3}\delta_{ij}\hat{\sigma}_{kk}^{\mathrm{Re}}\right),$$

$$B = \frac{3}{2}\left(\hat{\sigma}_{ij}^{\mathrm{Im}} - \frac{1}{3}\delta_{ij}\hat{\sigma}_{kk}^{\mathrm{Im}}\right)\left(\hat{\sigma}_{ij}^{\mathrm{Im}} - \frac{1}{3}\delta_{ij}\hat{\sigma}_{kk}^{\mathrm{Im}}\right),$$

$$C = 3\left(\hat{\sigma}_{ij}^{\mathrm{Re}} - \frac{1}{3}\delta_{ij}\hat{\sigma}_{kk}^{\mathrm{Re}}\right)\left(\hat{\sigma}_{ij}^{\mathrm{Im}} - \frac{1}{3}\delta_{ij}\hat{\sigma}_{kk}^{\mathrm{Im}}\right),$$

$$\sin\phi_1 = \frac{(A-B)}{\sqrt{(A-B)^2 + C^2}},\ \cos\phi_1 = \frac{-C}{\sqrt{(A-B)^2 + C^2}}\,.$$

The maximum value and corresponding time can be obtained using the coefficients obtained from Eq. (3-11), as follows:

$$\max(\sigma_{vM}(t)) = \sqrt{\frac{\sqrt{(A-B)^2 + C^2}}{2} + \frac{A+B}{2}} \quad \text{when } 0 \le \omega t = n\pi + \frac{\pi}{4} - \frac{\phi}{2} \le 2\pi\,. \tag{3-12}$$

3.2.2. Principal stress

By substituting each stress component expressed in Eq. (3-8) into the equation for calculating the principal stress Eq. (3-10) and rearranging using trigonometric expressions, the following equation for calculating the principal stress in the time domain can be obtained.

$$P_1 = \frac{I_1(t)}{3} + \frac{2}{3}\left(\sqrt{I_1^2(t) - 3I_2(t)}\right)\cos\phi ,$$

$$P_2 = \frac{I_1(t)}{3} + \frac{2}{3}\left(\sqrt{I_1^2(t) - 3I_2}(t)\right)\cos\left(\phi(t) - \frac{2\pi}{3}\right),$$

$$P_3(t) = \frac{I_1(t)}{3} + \frac{2}{3}\left(\sqrt{I_1^2(t) - 3I_2}(t)\right)\cos\left(\phi(t) - \frac{4\pi}{3}\right), \tag{3-13}$$

where

$$I_1(t) = \sigma_{ii}(t) = \hat{\sigma}_{ii}^{\mathrm{Re}} \cos\omega t - \hat{\sigma}_{ii}^{\mathrm{Im}} \sin\omega t ,$$

$$I_2(t) = \frac{1}{2}\left\{\left(\hat{\sigma}_{ii}^{\mathrm{Re}}\hat{\sigma}_{jj}^{\mathrm{Re}} - \hat{\sigma}_{ij}^{\mathrm{Re}}\hat{\sigma}_{ij}^{\mathrm{Re}}\right)\cos^2\omega t + \left(\hat{\sigma}_{ii}^{\mathrm{Im}}\hat{\sigma}_{jj}^{\mathrm{Im}} - \hat{\sigma}_{ij}^{\mathrm{Im}}\hat{\sigma}_{ij}^{\mathrm{Im}}\right)\sin^2\omega t\right\}$$

$$-\frac{1}{2}\left\{\left(\hat{\sigma}_{ii}^{\mathrm{Re}}\hat{\sigma}_{jj}^{\mathrm{Im}} + \hat{\sigma}_{jj}^{\mathrm{Re}}\hat{\sigma}_{ii}^{\mathrm{Im}} - \hat{\sigma}_{ij}^{\mathrm{Im}}\hat{\sigma}_{ij}^{\mathrm{Re}} - \hat{\sigma}_{ij}^{\mathrm{Re}}\hat{\sigma}_{ij}^{\mathrm{Im}}\right)\sin\omega t\cos\omega t\right\},$$

$$I_3(t) = \varepsilon_{ijk}\left\{\hat{\sigma}_{1i}^{\mathrm{Re}}\hat{\sigma}_{2j}^{\mathrm{Re}}\hat{\sigma}_{3k}^{\mathrm{Re}}\cos^3\omega t - \left(\hat{\sigma}_{1i}^{\mathrm{Re}}\hat{\sigma}_{2j}^{\mathrm{Im}}\hat{\sigma}_{3k}^{\mathrm{Re}} + \hat{\sigma}_{1i}^{\mathrm{Re}}\hat{\sigma}_{2j}^{\mathrm{Re}}\hat{\sigma}_{3k}^{\mathrm{Im}} + \hat{\sigma}_{1i}^{\mathrm{Im}}\hat{\sigma}_{2j}^{\mathrm{Re}}\hat{\sigma}_{3k}^{\mathrm{Re}}\right)\sin\omega t\cos^2\omega t\right\}$$

$$+\varepsilon_{ijk}\left\{\left(\hat{\sigma}_{1i}^{\mathrm{Im}}\hat{\sigma}_{2j}^{\mathrm{Im}}\hat{\sigma}_{3k}^{\mathrm{Re}} + \hat{\sigma}_{1i}^{\mathrm{Im}}\hat{\sigma}_{2j}^{\mathrm{Re}}\hat{\sigma}_{3k}^{\mathrm{Im}} + \hat{\sigma}_{1i}^{\mathrm{Re}}\hat{\sigma}_{2j}^{\mathrm{Im}}\hat{\sigma}_{3k}^{\mathrm{Im}}\right)\sin^2\omega t\cos\omega t - \hat{\sigma}_{1i}^{\mathrm{Im}}\hat{\sigma}_{2j}^{\mathrm{Im}}\hat{\sigma}_{3k}^{\mathrm{Im}}\sin^3\omega t\right\},$$

$$\phi(t) = \frac{1}{3}\cos^{-1}\left(\frac{2I_1^3(t) - 9I_1(t)I_2(t) + 27I_3(t)}{2(I_1^2(t) - 3I_2(t))^{3/2}}\right).$$

Since Eq. (3-13) consists of the sum of harmonic and non-harmonic functions, it is not easy to analytically obtain the maximum value. Newton-Raphson method is employed for the maximum value.

In the case of plane stress, the principal stress (P_1) at a specific time can be defined as follows.

$$P_1 = \sqrt{D^2 + E^2}\cos(\omega t + \phi_1) + \sqrt{\sqrt{\left(\left(\frac{F-G}{2}\right)^2 + \left(\frac{H}{2}\right)^2\right)}\cos(2\omega t + \phi_2) + \frac{F+G}{2}} \tag{3-14}$$

where

$$D = \frac{1}{2}\delta_{ij}\hat{\sigma}_{kk}^{\mathrm{Re}}, \quad E = \frac{1}{2}\delta_{ij}\hat{\sigma}_{kk}^{\mathrm{Im}},$$

$$F = \frac{1}{4}\left(\hat{\sigma}_{ij}^{\mathrm{Re}} - \frac{1}{2}\delta_{ij}\hat{\sigma}_{kk}^{\mathrm{Re}}\right)\left(\hat{\sigma}_{ij}^{\mathrm{Re}} - \frac{1}{2}\delta_{ij}\hat{\sigma}_{kk}^{\mathrm{Re}}\right),$$

$$G = \frac{1}{4}\left(\hat{\sigma}_{ij}^{\mathrm{Im}} - \frac{1}{2}\delta_{ij}\hat{\sigma}_{kk}^{\mathrm{Im}}\right)\left(\hat{\sigma}_{ij}^{\mathrm{Im}} - \frac{1}{2}\delta_{ij}\hat{\sigma}_{kk}^{\mathrm{Im}}\right),$$

$$H = \frac{1}{2}\left(\hat{\sigma}_{ij}^{\mathrm{Re}} - \frac{1}{2}\delta_{ij}\hat{\sigma}_{kk}^{\mathrm{Re}}\right)\left(\hat{\sigma}_{ij}^{\mathrm{Im}} - \frac{1}{2}\delta_{ij}\hat{\sigma}_{kk}^{\mathrm{Im}}\right),$$

$$\cos\phi_1 = \frac{D}{\sqrt{D^2 + E^2}}, \quad \sin\phi_1 = \frac{E}{\sqrt{D^2 + E^2}},$$

$$\cos\phi_2 = \frac{F-G}{\sqrt{(F-G)^2+(H)^2}}, \quad \sin\phi_2 = \frac{H}{\sqrt{(F-G)^2+(H)^2}}.$$

As the Eq. (3-13) represents a non-harmonic function, finding the maximum value analytically is challenging. Therefore, we attempted to use the Newton-Raphson method [53, 54] to obtain a solution. In numerical analysis, Newton's method, also known as the Newton–Raphson method, named after Isaac Newton and Joseph Raphson, is a root-finding algorithm which produces successively better approximations to the roots (or zeroes) of a real-valued function. We searched for the value where the first derivative becomes zero, aiming to locate the maximum value at that position. The first derivative of the function can be expressed as follows,

$$\frac{dP_1}{d\theta} = -D\sin\theta - E\cos\theta + \frac{-F\cos\theta\sin\theta + G\sin\theta\cos\theta - \frac{1}{2}H(\cos^2\theta - \sin^2\theta)}{\sqrt{F\cos^2\theta + G\sin^2\theta - H\sin\theta\cos\theta}} = 0. \tag{3-16}$$

By utilizing the relationship that the maximum value of the function composed of two periodic functions occurs between the maximum value positions of the two functions, we can predict the interval where the maximum value will occur in advance. For this purpose, we use the ωt that maximizes the first term on the right is used as the initial and search for the maximum value accordingly.

3.3. Numerical examples

In this section, the validity and effectiveness of the direct calculation of stress RAO in hydroelastic analysis demonstrated through various problems. In the proposed numerical procedure, the structures are modeled by the well-known MITC4 shell finite elements [34-39].

Two problems for showing the procedure are solved: the von-Mises stress calculation method and the principal stress calculation method, and the results are compared with those of the previous method.

3.3.1. von-Mises stress

In order to validate the effectiveness of the proposed method, the results obtained from the conventional method and the proposed method are compared. The stress components obtained from elastoplastic analysis will be used for calculations.

The stress components are given below,

$$\begin{bmatrix} \hat{\sigma}_{11}^{\mathrm{Re}} \\ \hat{\sigma}_{22}^{\mathrm{Re}} \\ \hat{\sigma}_{33}^{\mathrm{Re}} \\ \hat{\sigma}_{12}^{\mathrm{Re}} \\ \hat{\sigma}_{23}^{\mathrm{Re}} \\ \hat{\sigma}_{31}^{\mathrm{Re}} \end{bmatrix} = \begin{bmatrix} -28 \\ -50 \\ 0 \\ 28 \\ 0 \\ 0 \end{bmatrix} [\mathrm{MPa}], \quad \begin{bmatrix} \hat{\sigma}_{11}^{\mathrm{Im}} \\ \hat{\sigma}_{22}^{\mathrm{Im}} \\ \hat{\sigma}_{33}^{\mathrm{Im}} \\ \hat{\sigma}_{12}^{\mathrm{Im}} \\ \hat{\sigma}_{23}^{\mathrm{Im}} \\ \hat{\sigma}_{31}^{\mathrm{Im}} \end{bmatrix} = \begin{bmatrix} -15 \\ -10 \\ 0 \\ -5 \\ 0 \\ 0 \end{bmatrix} [\mathrm{MPa}].$$

In order to utilize the conventional method, the period was divided into 36 equal increments from 0 to T. The stress components and the corresponding von-Mises stress for each time step were calculated.

The maximum value during one cycle, calculated using the Eq. (3-12), is as follows.

$A = 4236$, $B = 250$, $C = -30$.

$$\sin\phi = \frac{(A-B)}{\sqrt{(A-B)^2 + C^2}} = 0.99997, \quad \cos\phi = \frac{-C}{\sqrt{(A-B)^2 + C^2}} = 0.00752$$

$$\max(\sigma_{vM}(t)) = \sqrt{\frac{\sqrt{(A-B)^2 + C^2}}{2} + \frac{A+B}{2}} = 65.0850, \text{ when } t = 0.4974T$$

Within one cycle ($0 \le t \le T$), the value of von-Mises stress and its corresponding time are obtained as shown above. It can be observed that the maximum value may vary depending on the spacing of time steps in the conventional method.

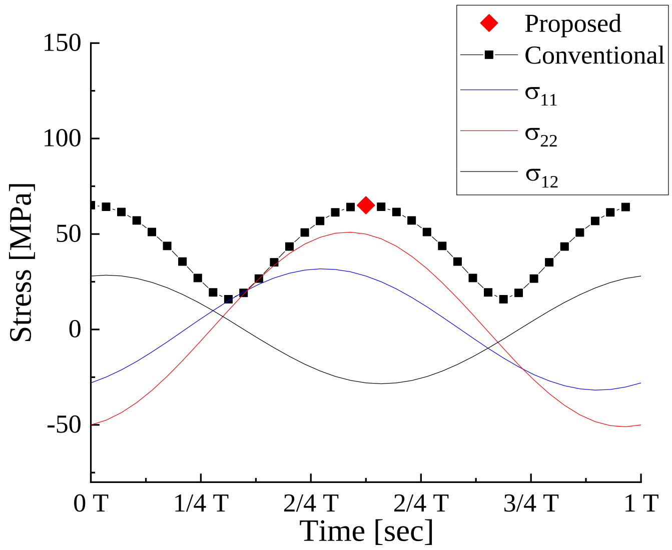

Fig. 3-4. The von-Mises stress results obtained from conventional method and proposed method.

The Fig. 3-4 shows the von-Mises stress results obtained from conventional method and proposed method. It is confirmed that the proposed method allows us to find the maximum value in just one calculation, compared to the previous method which required 36 calculations. This indicates that this method is more efficient and faster in finding the maximum value.

3.3.2. Principal stress

The validity of the proposed method is demonstrated for the principal stress case. The stress components obtained from elastoplastic analysis will be used for calculations. The results are compared by using both the conventional method and the proposed method in this study.

The stress components are given below,

$$\begin{bmatrix} \hat{\sigma}_{11}^{\mathrm{Re}} \\ \hat{\sigma}_{22}^{\mathrm{Re}} \\ \hat{\sigma}_{33}^{\mathrm{Re}} \\ \hat{\sigma}_{12}^{\mathrm{Re}} \\ \hat{\sigma}_{23}^{\mathrm{Re}} \\ \hat{\sigma}_{31}^{\mathrm{Re}} \end{bmatrix} = \begin{bmatrix} -28 \\ -50 \\ 0 \\ 28 \\ 0 \\ 0 \end{bmatrix} [\mathrm{MPa}], \quad \begin{bmatrix} \hat{\sigma}_{11}^{\mathrm{Im}} \\ \hat{\sigma}_{22}^{\mathrm{Im}} \\ \hat{\sigma}_{33}^{\mathrm{Im}} \\ \hat{\sigma}_{12}^{\mathrm{Im}} \\ \hat{\sigma}_{23}^{\mathrm{Im}} \\ \hat{\sigma}_{31}^{\mathrm{Im}} \end{bmatrix} = \begin{bmatrix} -15 \\ -10 \\ 0 \\ -5 \\ 0 \\ 0 \end{bmatrix} [\mathrm{MPa}].$$

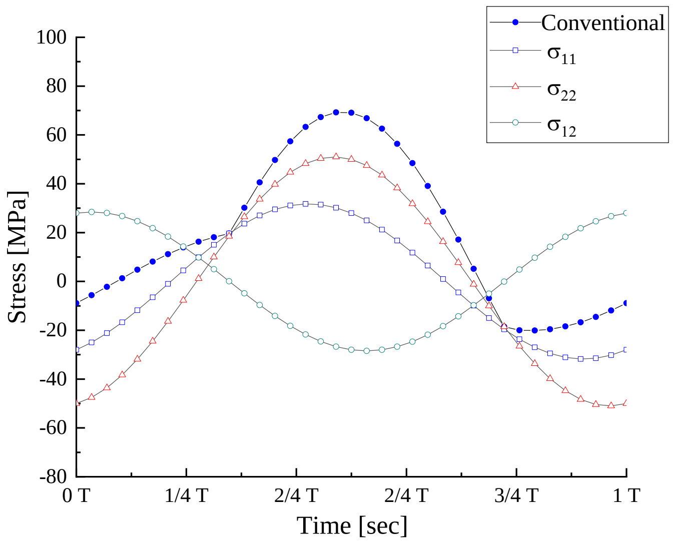

Fig. 3-5. The principal stress result obtained from conventional method.

In order to utilize the conventional method, the wave period(T) was divided into 36 equal increments from 0 to T. The stress components and the corresponding principal stress for each time step were calculated, and the results are shown in the Fig. 3-5.

The coefficients for Eq. (3-14) are obtained as follows.

$D = -39$, $E = 12.5$, $F = 905$, $G = 31.25$, $H = 335$,

$$\cos\phi_1 = \frac{D}{\sqrt{D^2 + E^2}} = -0.9523, \quad \sin\phi_1 = \frac{E}{\sqrt{D^2 + E^2}} = -0.3052$$

$$\cos\phi_2 = \frac{F - G}{\sqrt{(F-G)^2 + (H)^2}} = 0.9337, \quad \sin\phi_2 = \frac{H}{\sqrt{(F-G)^2 + (H)^2}} = -0.3580.$$

We use the previously computed coefficients to determine the values for equations (3-14) and (3-15). The initial value of, which corresponds to the first term on the right-hand side, is set to its maximum value($t = 0.4506T$), and the Newton-Raphson method is employed to obtain the overall maximum value of the entire equation. The iteration is performed 2 times. The existing method calculates RAO through 36 calculations, whereas the proposed method calculates RAO through two calculations.

$P_{1\_max} = 69.4301, \; t = 0.4840T$.

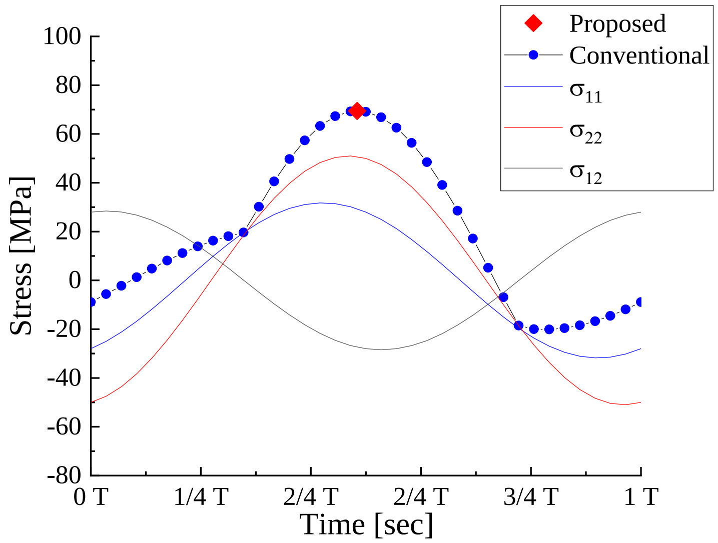

Fig. 3-6. Principal stress result obtained from conventional method and proposed method.

The results obtained by each method are shown in Fig. 3-6. We have observed that the maximum principal stress value and its corresponding time within a single cycle ($0 \le t \le T$). While the conventional method utilized the result calculated at a time step near the maximum value as the maximum value, the proposed method allows for obtaining a more accurate maximum value with fewer calculations.

3.3.3. A floating barge problem

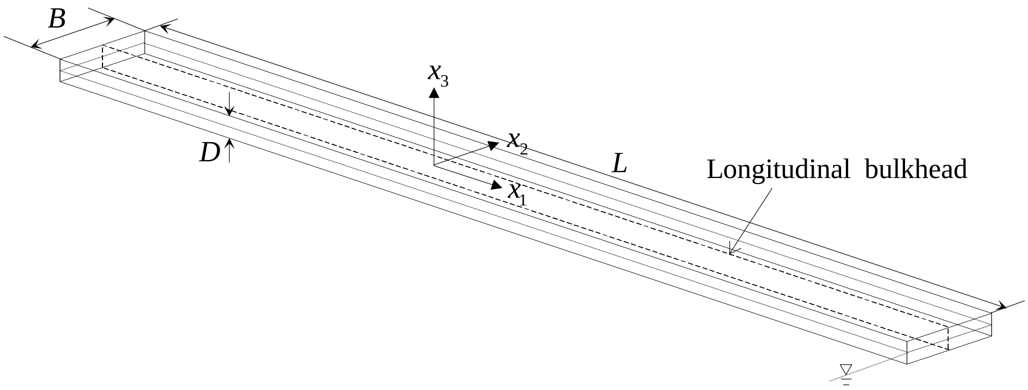

(a)

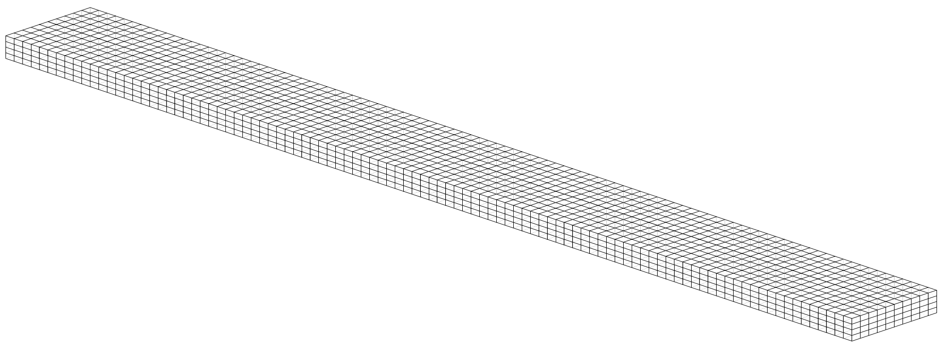

(b)

Fig. 3-7. Floating barge problem: (a) problem description and (b) finite and boundary element meshes used.

Let us consider the floating barge problem shown in Fig.3-7[7]. The barge's dimensions are the same with the one used in the reference [59]; that is, the length $L = 100\,\mathrm{m}$, the breadth B is 10 m, and the depth D is 2 m. A longitudinal bulkhead is additionally installed along the centerline in the barge model. Table. 3-1 shows the thickness and density of the floating barge.

Table 3-1. Thickness and density distributions of the floating barge.

	Top deck	Bottom deck	Side hull	Bulk head
Thickness t_s [m]	0.005	0.02	0.02	0.005
Density ρ_s [kg/m^3]	1.0×10^3	3.3389×10^4	3.3389×10^4	3.3389×10^4

For the barge model, 100, 10, and 4 shell finite elements are used in the length, breadth, and depth directions, respectively, and 100, 10, and 2 boundary elements are used for the fluid interface, respectively. We use the elastic modulus $E = 100$ GPa, Poisson's ratio $\upsilon = 0.3$, wave period $T = 4-16s$, and incident wave angle $\theta = 0°$. Then, hydroelastic analyses are carried out. von-Mises stress and principal stress RAO are obtained using the calculated component stresses from hydroelastic analysis.

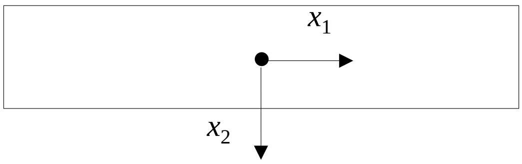

(a)

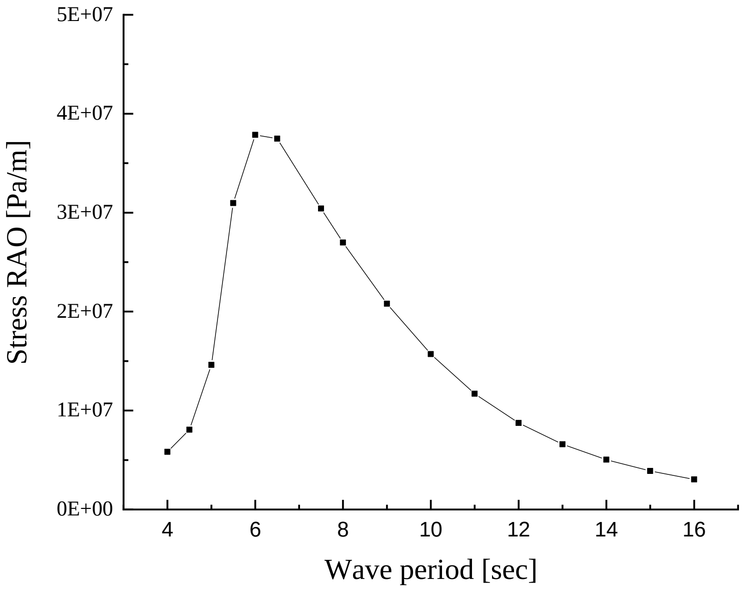

(b)

Fig. 3-8. Von-Mises stress RAO of the floating barge: (a) measuring point and (b) stress RAO.

Table 3-2. von-Mises stress RAO Computational time of the floating barge

	Previous	Proposed
Computational time [sec]	19.36	1.47 (7.6%)

Fig.3-8 shows the von-Mises stress RAO using the proposed method. The RAO is measured the center of the bottom of the barge. Table 3-2 shows the results compared with the existing method, and it is confirmed that the calculation time is reduced to 7.6% compared to the existing method.

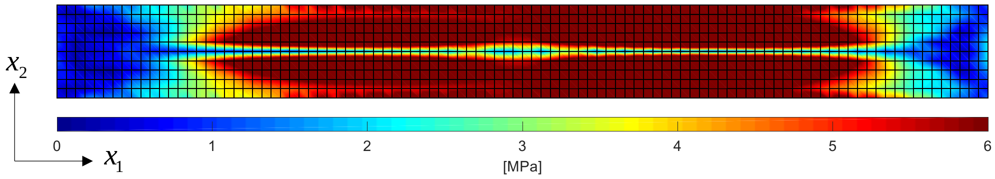

Fig. 3-9. von-Mises stress RAO distribution of the floating barge.

Fig. 3-9 show the von-Mises stress RAO when the wave period is 4 seconds. In this figure, the von-Mises stress RAO for each point of the corresponding wave can be checked.

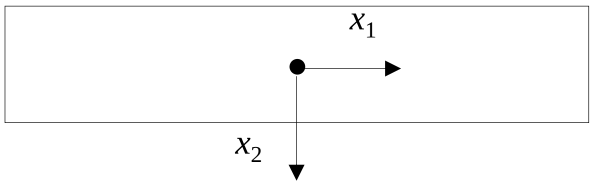

(a)

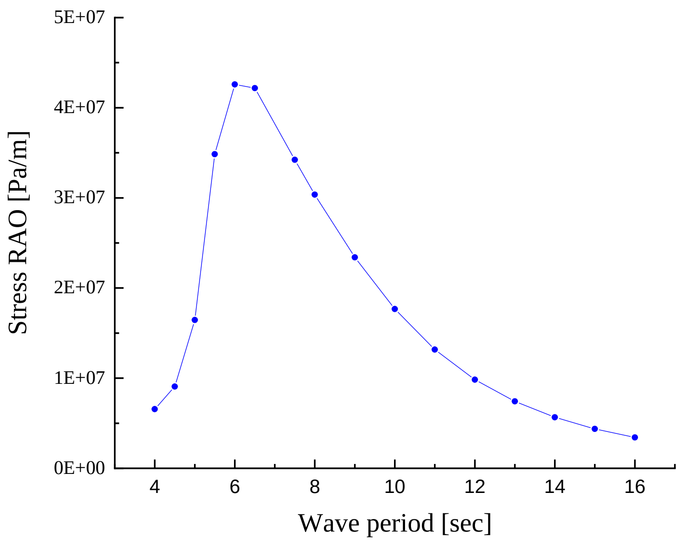

(b)

Fig. 3-10. Principal stress RAO of the floating barge: (a) measuring point and (b) stress RAO.

Table 3-3. Principal stress RAO Computational time of the floating barge

	Previous	Proposed
Computational time [sec]	19.78	5.42 (27.4%)

Fig.3-10 shows the principal stress RAO using the proposed method. The RAO is measured the center of the bottom of the barge. Table 3-3 shows the results compared with the existing method, and it is confirmed that the calculation time is reduced to 27.4% compared to the existing method.

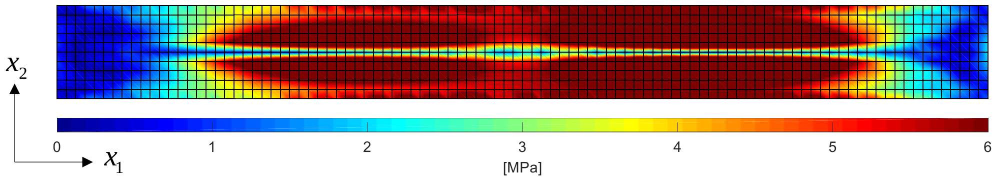

Fig. 3-11. Maximum principal stress distribution of the floating barge.

Fig. 3-11 shows the principal stress RAO when the wave period is 4 seconds.

3.3.4. Whole ship problem

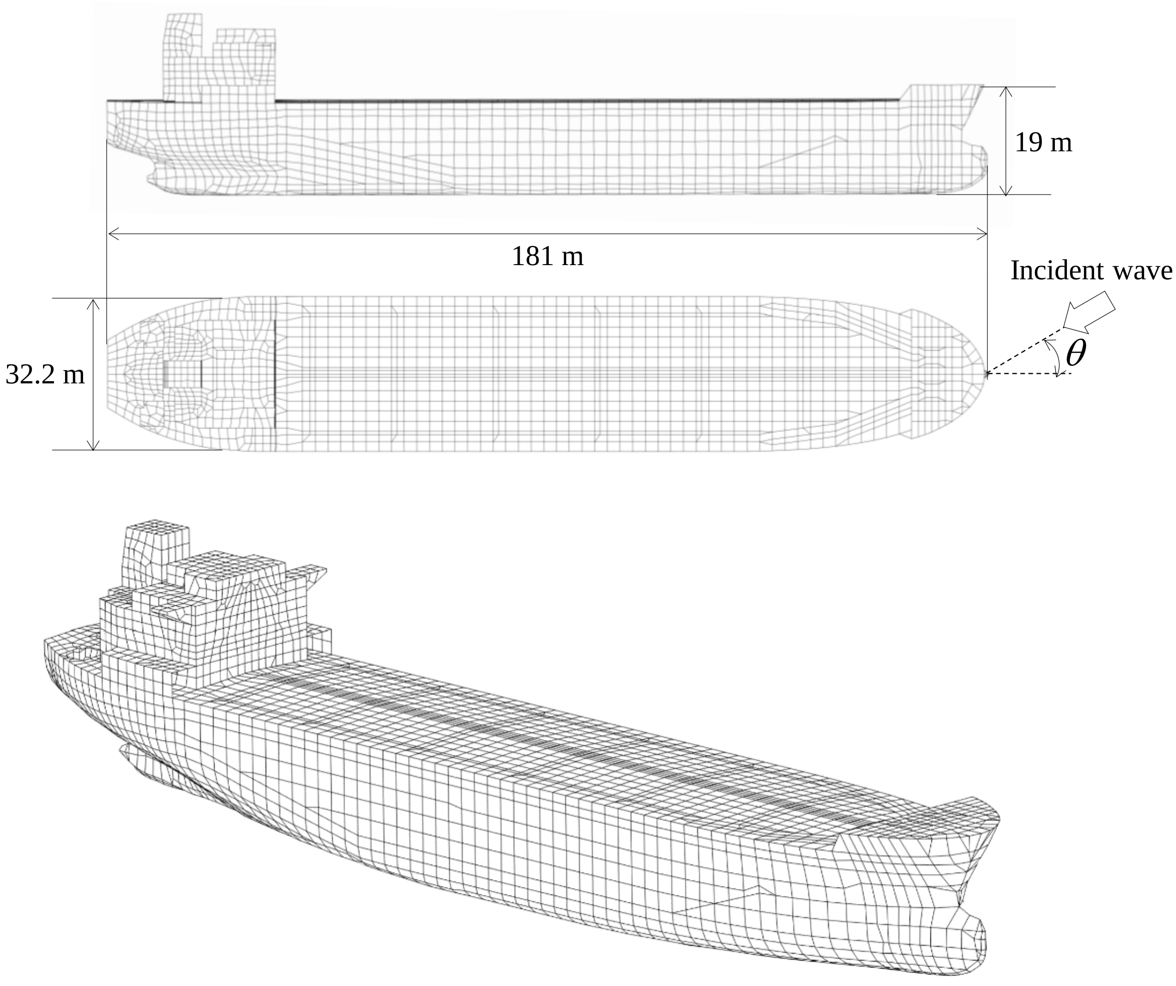

Fig. 3-12. Whole ship FE model

We consider a ship with 12 tanks, shown in Fig. 3-12. Length, breadth, and height (bottom to deck) are 181 m, 32.2 m, and 19 m, respectively. The density of the structure is 7,870 kg/m^3, Young's modulus E = 210 GPa, and Poisson's ratio ν = 0.3. Incident wave angle is 45 degrees and its period ranges from 8.0 to 26.0 s, with a constant increment (ΔT = 1 s).

The whole ship structure is modeled using 17,029 shell finite elements as shown in Fig.3-12. The internal fluid is modeled by simply increasing the density of the surrounding tank structure. The whole ship model has finite element meshes for inner structures and outer hull, and the meshes are intricately connected.

Hydrostatic and hydroelastic analysis are then carried out. Then, hydroelastic analyses are carried out.

von-Mises stress and principal stress RAO are obtained using the calculated component stresses from hydroelastic analysis.

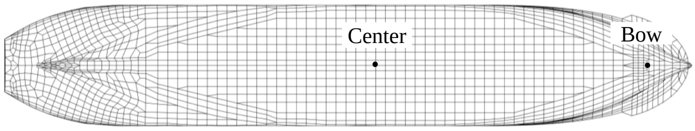

(a)

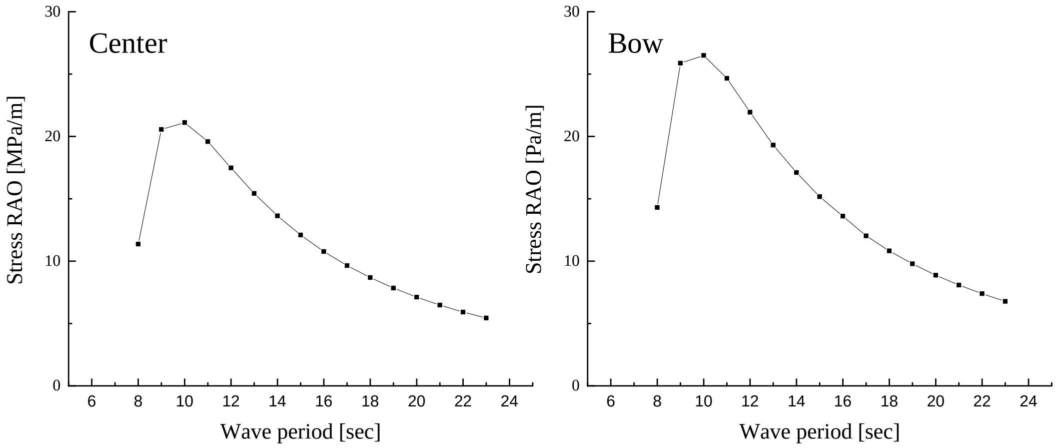

(b)

Fig. 3-13. Von-Mises stress RAO of the whole ship model: (a) measuring point and (b) stress RAO.

Table 3-4. von-Mises stress RAO Computational time of the whole ship

	Previous	Proposed
Computational time [sec]	59.76	4.937 (8.2%)

Fig. 3-13 presents the calculated von-Mises stress RAO at bow and center of the bottom. In addition, Table 3-4 shows the calculation time of von-Mises stress. Compared to the existing method, it is confirmed that the calculation time is reduced by 8.2%.

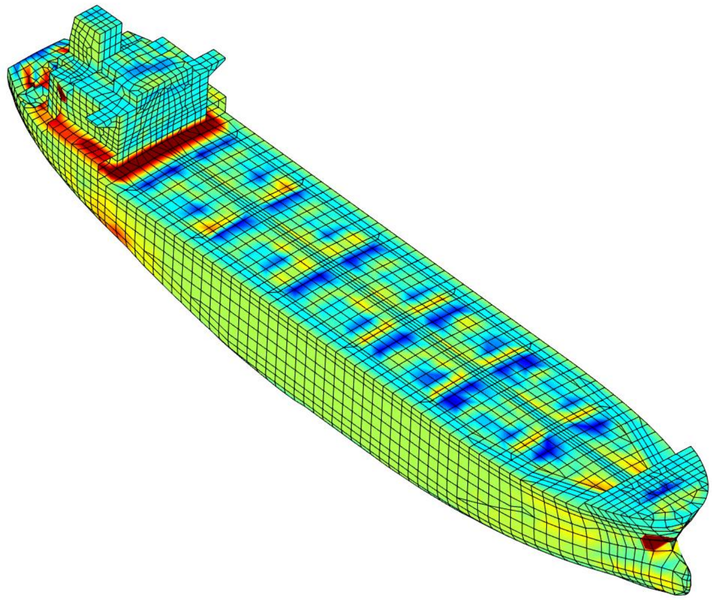

Fig. 3-14. von-Mises stress RAO distribution of the whole ship model.

Fig. 3-14 shows the von-Mises stress RAO when the wave period is 11 seconds. In this figure, the von-Mises stress RAO for each point of the corresponding wave can be checked.

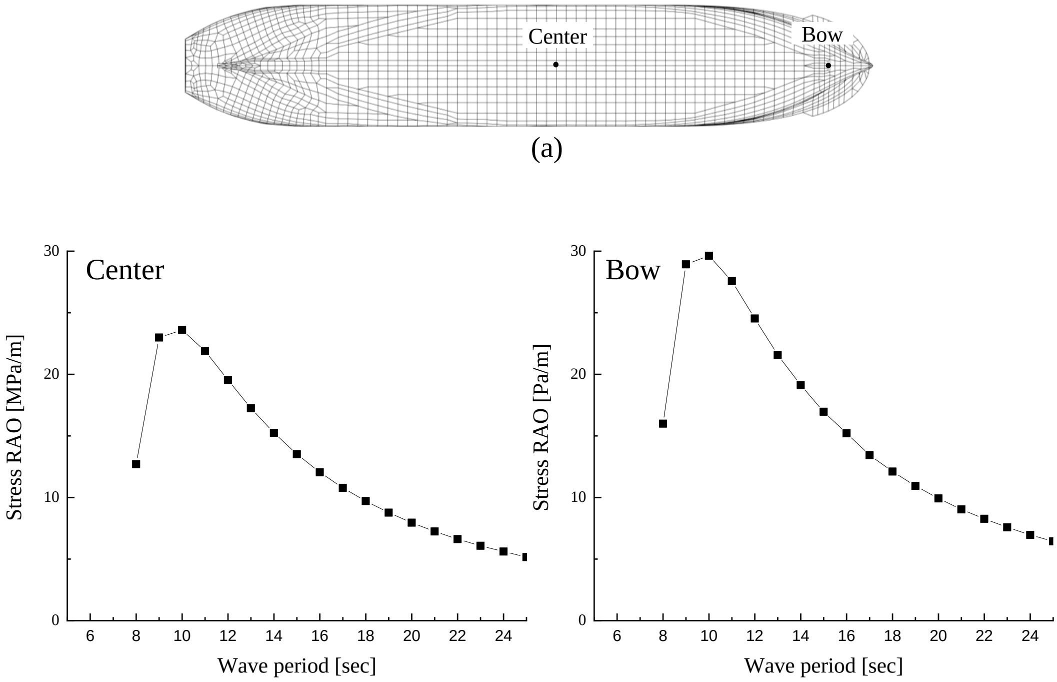

(a)

(b)

Fig. 3-15. Principal stress RAO of the whole ship model: (a) measuring point and (b) stress RAO.

Table 3-5. Principal stress RAO Computational time of the whole ship

	Previous	Proposed
Computational time [sec]	62.76	17.605 (28.0%)

We also confirm the results for principal stress. The calculated principal stress RAO at bow and center of the bottom are presented in Fig. 3-15. In addition, Table 3-5 shows the calculation time of principal stress. Compared to the existing method, it is confirmed that the calculation time is reduced by 28.0%.

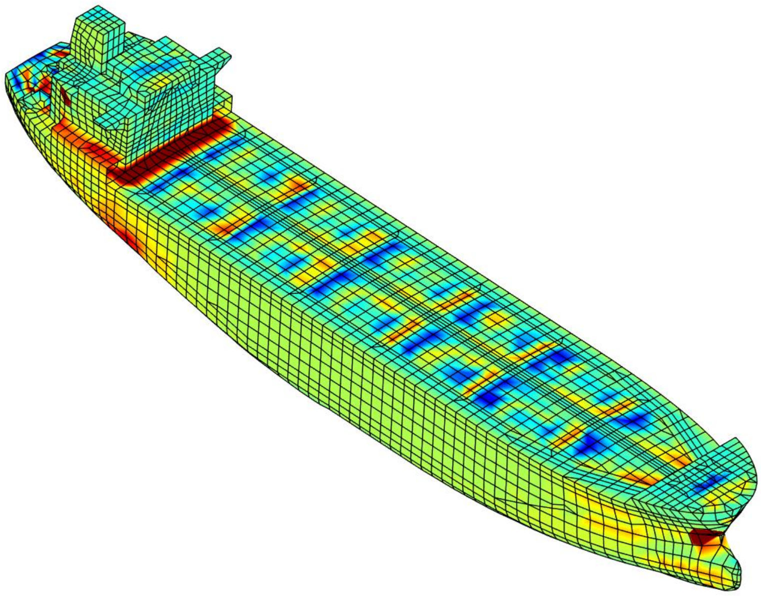

Fig. 3-16. Principal stress RAO distribution for the whole ship model.

Fig. 3-16 shows the principal stress RAO when the wave period is 11 seconds. In this figure, the principal stress RAO for each point of the corresponding wave can be checked.

3.4. Concluding remarks

We proposed a direct calculation method for the stress response amplitude operator (RAO) in the frequency domain for hydroelastic analysis. After calculating the component stresses using hydroelastic analysis and evaluating the strength using combined stresses such as von-Mises stress and principal stresses, the combined stresses are no longer in a harmonic form. Therefore, instead of using the conventional method of dividing a single cycle into equal intervals and calculating the maximum value within that cycle, we propose a direct method to find the maximum value. This approach allows for significant improvement in computational speed. We believe that our proposed method can contribute to the enhancement of computational efficiency in various applications such as ship and offshore structure design.

Chapter 4. Conclusions

The objective of this dissertation was to present an effective numerical method to integrate hydro-static and dynamic analysis of flexible floating structures. In general, hydrodynamic analysis is conducted in hydrostatic equilibrium, it is necessary to solve the non-matching mesh problem to propose an integrated equation. To deal with the non-matching mesh problem, we adopt an efficient numerical integration method, in which remeshing is not necessarily. Through this, hydrostatic analysis and hydrodynamic analysis were completely integrated.

In Chapter 2, we proposed a method for the hydro-elastic analysis considering various loading conditions, in which the direct-coupling method was employed to couple structural motions and water waves. When the cargo loading conditions of the floating structures change, the wet surface changes according to changing the hydrostatic equilibrium state. The remeshing is inevitable process to perform hydrodynamic analysis for each loading condition. The special numerical integration method was adopted to resolve the non-matching mesh problem without remeshing process.

In Chapter 3, we proposed a method for the direct calculation method of stress RAO in frequency domain. We proposed a direct calculation method for the stress response amplitude operator (RAO) in the frequency domain for hydroelastic analysis. After calculating the component stresses using hydroelastic analysis and evaluating the strength using combined stresses such as von-Mises stress and principal stresses, the combined stresses are no longer in a harmonic function. Therefore, instead of using the conventional method of dividing a single cycle into equal intervals and calculating the maximum value within that cycle, we propose a direct method to find the maximum value. This approach allows for significant improvement in computational speed. We believe that our proposed method can contribute to the enhancement of computational efficiency in various applications such as ship and offshore structure design, real-time monitoring.

The proposed numerical method can be easily used for the hydroelastic analysis of floating structures with various loading conditions. Moreover, it can be extended to the transient analysis of flexible floating structures in flooded conditions by considering the internal free surface effect. Furthermore, it will be valuable to extend the present research to nonlinear hydroelastic response, in which we could deal with the various loads causing nonlinear behavior of the floating structures.

Bibliography

[1] Bishop, R. E. D., Bishop, R. E., Price, W. G., 1979. Hydroelasticity of ships. Cambridge University Press, UK.

[2] Faltinsen, O. M., 2015. Hydrodynamics of marine and offshore structures. Journal of Hydrodynamics, Ser. B, 26(6), 835-847. https://doi.org/10.1016/S1001-6058(14)60092-5.

[3] John, F., 1949. On the motion of floating bodies I. Comm. Pure Appl. Math. 2, 13–57. https://doi.org/10.1002/cpa.3160020102.

[4] John, F., 1950. On the motion of floating bodies II, simple harmonic motions. Comm. Pure Appl. Math. 3, 45–101. https://doi.org/10.1002/cpa.3160030106.

[5] Mei, C. C., Stiassnie, M. A., Yue, D. K. P., 2005. Theory and Applications of Ocean Surface Waves, Part I: Linear Aspects. World Scientific, Singapore. https://doi.org/10.1142/9789813147195_0001.

[6] Newman, J. N., 2018. Marine Hydrodynamics. The MIT Press, Massachusetts. http://library.oapen.org/handle/20.500.12657/26039.

[7] Kim, B. W., Hong, S. Y., Kyoung, J. H., Cho, S. K., 2007. Evaluation of bending moments and shear forces at unit connections of very large floating structures using hydroelastic and rigid body analyses. Ocean engineering, 34(11-12), 1668-1679. https://doi.org/10.1016/j.oceaneng.2006.10.018.

[8] Khabakhpasheva, T., Korobkin, A., 2002. Hydroelastic behaviour of compound floating plate in waves. Journal of Engineering Mathematics 2002; 44:21–40. https://doi.org/10.1023/A:1020592414338.

[9] Wang, C. D., Meylan, M. H., 2004. A higher-order-coupled boundary element and finite element method for the wave forcing of a floating elastic plate. Journal of Fluids and Structures, 19(4), 557-572. https://doi.org/10.1016/j.jfluidstructs.2004.02.006.

[10] Taylor, R. E., 2007. Hydroelastic analysis of plates and some approximations. Journal of engineering mathematics, 58(1), 267-278. https://doi.org/10.1007/s10665-006-9121-7.

[11] Kim, K. T., Lee, P. S., Park, K. C., 2013. A direct coupling method for 3D hydroelastic analysis of floating structures. International journal for numerical methods in engineering, 96(13), 842-866. https://doi.org/10.1002/nme.4564.

[12] Kim, J. G., Cho, S. P., Kim, K. T., Lee, P. S., 2014. Hydroelastic design contour for the preliminary design of very large floating structures. Ocean engineering, 78, 112-123. https://doi.org/10.1016/j.oceaneng.2013.11.006.

[13] Yoon, J. S., Cho, S. P., Jiwinangun, R. G., Lee, P. S., 2014. Hydroelastic analysis of floating plates with multiple hinge connections in regular waves. Marine structures, 36, 65-87. https://doi.org/10.1016/j.marstruc.2014.02.002.

[14] Yoon, J. S., Lee, P. S., 2017. Towards hydro-elastoplastic analysis of floating plate structures. Journal of Fluids and Structures, 71, 164-182. https://doi.org/10.1016/j.jfluidstructs.2017.03.008.

[15] Lee, K. H., Lee, P. S., 2016. Nonlinear hydrostatic analysis of flexible floating structures. Applied Ocean Research, 59, 165-182. https://doi.org/10.1016/j.apor.2016.05.016.

[16] Li, S., Fu, S., Zhang, S., Moan, T., 2022. Second-order hydroelastic analysis of a flexible floating structure under spatially inhomogeneous waves. Marine Structures, 86, 103306. https://doi.org/10.1016/j.marstruc.2022.103306

[17] Bakti, F. P., Jin, C., Kim, M. H., 2021. Practical approach of linear hydro-elasticity effect on vessel with forward speed in the frequency domain. Journal of Fluids and Structures, 101, 103204. https://doi.org/10.1016/j.jfluidstructs.2020.103204.

[18] Lee, K. H., Cho, S., Kim, K. T., Kim, J. G., Lee, P. S., 2015. Hydroelastic analysis of floating structures with liquid tanks and comparison with experimental tests. Applied Ocean Research, 52, 167-187. https://doi.org/10.1016/j.apor.2015.06.002.

[19] Huang, L. L., Riggs, H. R., 2000. The hydrostatic stiffness of flexible floating structures for linear hydroelasticity. Marine Structures, 13(2), 91-106. https://doi.org/10.1016/S0951-8339(00)00007-1.

[20] Riggs, H. R., 2009. Comparison of formulations for the hydrostatic stiffness of flexible structures. Journal of offshore mechanics and Arctic engineering, 131(2). https://doi.org/10.1115/1.3058702.

[21] Senjanović, I., Tomić, M., Tomašević, S., 2008. An explicit formulation for restoring stiffness and its performance in ship hydroelasticity. Ocean Engineering, 35(13), 1322-1338. https://doi.org/10.1016/j.oceaneng.2008.06.004.

[22] Rodrigues, J. M., Guedes Soares, C., 2014. Exact pressure integrations on submerged bodies in waves using a quadtree adaptive mesh algorithm. International Journal for Numerical Methods in Fluids, 76(10), 632-652. https://doi.org/10.1002/fld.3948.

[23] Dommermuth, D. G., Sussman, M., Beck, R. F., O'Shea, T. T., Wyatt, D. C., Olson, K., MacNeice, P., 2014. The numerical simulation of ship waves using Cartesian grid methods with adaptive mesh refinement. arXiv preprint arXiv:1410.1942. https://doi.org/10.48550/arXiv.1410.1942.

[24] Rodrigues, J. M., Guedes Soares, C., 2019. Ship Vertical Loads From Using an Adaptive Mesh Pressure Integration Technique for Froude–Krylov Forces Calculation. Journal of Offshore Mechanics and Arctic Engineering, 141(1) : 011101. https://doi.org/10.1115/1.4040722.

[25] Ko, K. H., Park, T., Kim, K. H., Kim, Y., Yoon, D. H., 2011. Development of panel generation system for seakeeping analysis. Computer-Aided Design, 43(8), 848-862. https://doi.org/10.1016/j.cad.2011.04.013.

[26] Bathe, K. J., 2014. Finite Element Procedures 2nd ed. Klaus-Jürgen Bathe, Watertown, MA.

[27] Dean, R. G., & Dalrymple, R. A., 1991. Water wave mechanics for engineers and scientists (Vol. 2). world scientific publishing company. https://doi.org/10.1142/1232.

[28] Wehausen, J. V., Laitone, E. V., 1960. Surface waves. In Fluid Dynamics/Strömungsmechanik (pp. 446-778). Springer, Berlin, Heidelberg.

[29] Napa Ltd, 2016. NAPA for Design 2016.3 Manuals

[30] Rhinoceros, 2012. Orca 3D User manual.

[31] ANSYS®, 2020. Academic Research Mechanical, Release 2020 R1.

[32] Bureau Veritas, 2016. HYDROSTAR FOR EXPERTS USER MANUAL.

[33] WAMIT, Inc, 1999. WAMIT User manual. Versions 6.4.

[34] Dvorkin, E. N., Bathe, K. J., 1984. A continuum mechanics based four-node shell element for general non-linear analysis. Engineering computations. https://doi.org/10.1108/eb023562.

[35] Lee, Y., Lee, P. S., Bathe, K. J., 2014. The MITC3+ shell element and its performance. Computers & Structures, 138, 12-23. https://doi.org/10.1016/j.compstruc.2014.02.005.

[36] Jun, H., Yoon, K., Lee, P. S., Bathe, K. J., 2018. The MITC3+ shell element enriched in membrane displacements by interpolation covers. Computer Methods in Applied Mechanics and Engineering, 337, 458-480. https://doi.org/10.1016/j.cma.2018.04.007.

[37] Ko, Y., Lee, Y., Lee, P. S., Bathe, K. J., 2017. Performance of the MITC3+ and MITC4+ shell elements in widely-used benchmark problems. Computers & Structures, 193, 187-206. https://doi.org/10.1016/j.compstruc.2017.08.003.

[38] Lee, C., Lee, P. S., 2019. The strain-smoothed MITC3+ shell finite element. Computers & Structures, 223, 106096. https://doi.org/10.1016/j.compstruc.2019.07.005.

[39] Lee, C., Lee, P. S., 2018. A new strain smoothing method for triangular and tetrahedral finite elements. Computer Methods in Applied Mechanics and Engineering, 341, 939-955. https://doi.org/10.1016/j.cma.2018.07.022.

[40] Altair Engineering, Inc., 2021. HyperMesh 2021.1 User Guide.

[41] Edition, F., Journée, J. M. J., & Massie, W. W., 2001. Offshore hydromechanics. Delft University of Technology.

[42] DNV, 2021. Sesam User Manual Xtract

[43] Jeong, J. M., Jeong, B. H., Oh, M. H., 2023. Strength and Fatigue Analysis of Ship and Offshore Structures using Direct Load Calculation. Computational Structural Engineering Institute of Korea annual conference.

[44] Choung, J. M., Joung, J. H., Choo, M. H., & Yoon, K. Y,. 2007. Development of Fully stochstic Fatigue Anlayisis Program for Offshore Floaters. Journal of the Society of Naval Architects of Korea.

[45] DNV., 2014. RP-C203: Fatigue design of offshore steel structures. DNV GL AS.

[46] ABS., 2020. Guide for Fatigue Assessment of Offshore Structures. Standardization. American Bureau of Shipping

[47] DNV., 2011. CN.31.7, Strength Analysis of Hull Structures in Container Ships. DNV GL AS

[48] ABS., 2014. Guidance notes on : SAFEHULL FINITE ELEMENT ANALYSIS OF HULL STRUCTURES. American Bureau of Shipping.

[49] Tian, C, Wu, Y. S., 2006. Second-order hydroelastic analysis of a SWATH ship moving in large-amplitude waves. J Hydrodyn. 18(6):631-639. doi:10.1016/S1001-6058(07)60001-8.

[50] Javanmardi, N, Ghadimi, P., 2018. Hydroelastic analysis of a semi-submerged propeller using simultaneous solution of Reynolds-averaged Navier–Stokes equations and linear elasticity equations. Proc Inst Mech Eng Part M J Eng Marit Environ. 232(2):199-211. doi:10.1177/1475090217691864.

[51] Allan TD., 1992. The marine environment. Int J Remote Sens. 13(6-7):1261-1276. doi:10.1080/01431169208904190

[52] Shehzad, K., Huilong, R., Guoqing, F., Khurram, A. 2013. Towards the procedure automation of full stochastic spectral based fatigue analysis. Res J Appl Sci Eng Technol. 5(17):4388-4394. doi:10.19026/rjaset.5.4433.

[53] TJALLING, J., Y. 1995. Historical development of the prescription. Interne. 37(4):531-551.

[54] Verbeke, J., Cools, R. 1995. The newton-raphson method. Int J Math Educ Sci Technol. 26(2):177-193. doi:10.1080/0020739950260202.

[55] Shin, H., Lee, H. Y., Lim, C. G., Shin, H. S., Park, I. G. 2000. Motion Analysis of a Very Large Floating Structure in Irregular Waves. Proceedings of the Korea Committee for Ocean Resources and Engineering Conference.

[56] Tang, H., Ren, H., Li, H., Zhong, Q. 2016. Experimental Investigation of Wave-Induced Hydroelastic Vibrations of Trimaran in Oblique Irregular Waves. Shock Vib. Doi:10.1155/2016/8794560

[57] Li, L., Fu, S., Xu, Y. 2013. Nonlinear hydroelastic analysis of an aquaculture fish cage in irregular waves. Mar Struct. doi:10.1016/j.marstruc.2013.08.002.

[58] Liu, Y., Mizutani, N., Cho, Y., H., Nakamura, T. 2022. Nonlinear hydrodynamic analysis and optimization of oscillating wave surge converters under irregular waves. Ocean Eng. Doi:10.1016/j.oceaneng.2022.110888.

[59] Riggs HR, Niimi KM, Huang LL. Two benchmark problems for three-dimensional, linear hydroelasticity. Journal of Offshore Mechanics and Arctic Engineering 2007; 129(3):149–157.

Acknowledgement

먼저 저의 박사학위 과정에 있어서 귀중한 지도와 지원을 해 주신 이필승 교수님께 깊은 감사의 말씀을 전하고자 합니다. 교수님께서는 저를 제자로 받아 주시고, 학문적인 도전과 성장을 격려해 주셨습니다. 교수님의 열정과 영감은 항상 박사과정을 힘들지 않게 만들어 주었으며, 항상 저에게 도전하고 발전할 수 있는 기회를 주셨습니다. 교수님의 인도와 가르침으로 인해 저는 더 나은 연구자로 성장할 수 있었습니다.

바쁘신 와중에도 학위 심사위원으로 흔쾌히 응해 주신 김진환 교수님, 김대겸 교수님, 김병완 박사님, 김태영 박사님께도 깊은 감사의 인사를 드리고 싶습니다. 귀중한 조언과 피드백에 깊이 감사드립니다. 항상 가까이서 응원해 주시고 염려해 주신 나양섭 교수님께도 깊은 감사의 말씀을 전하고 싶습니다. 그리고 카이스트와 처음 인연을 맺게 해 주시고 관심과 격려로 자신감을 키워 주신 허훈 교수님께 감사의 말씀을 드립니다.

또한, 훈태, 승보, 소진, 승환, 승규, 재현, 윤성 CMSS 가족에게도 감사의 말씀을 전하고 싶습니다. 함께 토론하고 협력할 수 있었던 것은 큰 보람이었습니다. 다양한 시각과 아이디어를 얻을 수 있었으며, 항상 저를 믿고 지지해 주는 좋은 친구가 되어주어 깊이 감사드립니다.

마지막으로, 어머니와 누나, 매형 그리고 우진이와 은진이에게도 깊은 감사의 말씀을 전하고 싶습니다. 항상 저를 걱정과 믿음으로 저에게 든든한 힘이 되었습니다. 가족의 사랑과 지원이 저에게는 큰 원동력이 되었습니다.

많은 좋은 분들이 계셨기에 좋은 결실을 맺을 수 있었습니다. 다시한번 감사의 말씀을 드립니다.